

World Journal of *Radiology*

World J Radiol 2024 July 28; 16(7): 241-293



EDITORIAL

- 241 Advantages of the intradermal lymphoscintigraphy
Tartaglione G

ORIGINAL ARTICLE**Retrospective Study**

- 247 Ultrasomics in liver cancer: Developing a radiomics model for differentiating intrahepatic cholangiocarcinoma from hepatocellular carcinoma using contrast-enhanced ultrasound
Su LY, Xu M, Chen YL, Lin MX, Xie XY
- 256 Correlation between dose-volume parameters and rectal bleeding after 12 fractions of carbon ion radiotherapy for prostate cancer
Ono T, Sato H, Miyasaka Y, Hagiwara Y, Yano N, Akamatsu H, Harada M, Ichikawa M

Observational Study

- 265 Incidence of exclusive extrapelvic skeletal metastasis in prostate carcinoma on bone scintigraphy
Singh P, Agrawal K, Rahman A, Singhal T, Parida GK, Gnanasegaran G

SYSTEMATIC REVIEWS

- 274 Evaluating the role of 7-Tesla magnetic resonance imaging in neurosurgery: Trends in literature since clinical approval
Perera Molligoda Arachchige AS, Meuli S, Centini FR, Stomeo N, Catapano F, Politi LS

ABOUT COVER

Editorial Board Member of *World Journal of Radiology*, Ali Abbasian Ardakani, PhD, Assistant Professor, Department of Radiology Technology, School of Allied Medical Sciences, Shahid Beheshti University of Medical Sciences, Tehran 1971653313, Iran. ardakani@sbmu.ac.ir

AIMS AND SCOPE

The primary aim of *World Journal of Radiology* (*WJR*, *World J Radiol*) is to provide scholars and readers from various fields of radiology with a platform to publish high-quality basic and clinical research articles and communicate their research findings online.

WJR mainly publishes articles reporting research results and findings obtained in the field of radiology and covering a wide range of topics including state of the art information on cardiopulmonary imaging, gastrointestinal imaging, genitourinary imaging, musculoskeletal imaging, neuroradiology/head and neck imaging, nuclear medicine and molecular imaging, pediatric imaging, vascular and interventional radiology, and women's imaging.

INDEXING/ABSTRACTING

The *WJR* is now abstracted and indexed in PubMed, PubMed Central, Emerging Sources Citation Index (Web of Science), Reference Citation Analysis, China Science and Technology Journal Database, and Superstar Journals Database. The 2024 Edition of Journal Citation Reports® cites the 2023 journal impact factor (JIF) for *WJR* as 1.4; JIF without journal self cites: 1.4; 5-year JIF: 1.8; JIF Rank: 132/204 in radiology, nuclear medicine and medical imaging; JIF Quartile: Q3; and 5-year JIF Quartile: Q3.

RESPONSIBLE EDITORS FOR THIS ISSUE

Production Editor: *Xin-Xin Che*, Production Department Director: *Xu Guo*; Cover Editor: *Jia-Ping Yan*.

NAME OF JOURNAL

World Journal of Radiology

ISSN

ISSN 1949-8470 (online)

LAUNCH DATE

January 31, 2009

FREQUENCY

Monthly

EDITORS-IN-CHIEF

Thomas J Vogl

EDITORIAL BOARD MEMBERS

<https://www.wjgnet.com/1949-8470/editorialboard.htm>

PUBLICATION DATE

July 28, 2024

COPYRIGHT

© 2024 Baishideng Publishing Group Inc

INSTRUCTIONS TO AUTHORS

<https://www.wjgnet.com/bpg/gerinfo/204>

GUIDELINES FOR ETHICS DOCUMENTS

<https://www.wjgnet.com/bpg/GerInfo/287>

GUIDELINES FOR NON-NATIVE SPEAKERS OF ENGLISH

<https://www.wjgnet.com/bpg/gerinfo/240>

PUBLICATION ETHICS

<https://www.wjgnet.com/bpg/GerInfo/288>

PUBLICATION MISCONDUCT

<https://www.wjgnet.com/bpg/gerinfo/208>

ARTICLE PROCESSING CHARGE

<https://www.wjgnet.com/bpg/gerinfo/242>

STEPS FOR SUBMITTING MANUSCRIPTS

<https://www.wjgnet.com/bpg/GerInfo/239>

ONLINE SUBMISSION

<https://www.f6publishing.com>

Advantages of the intradermal lymphoscintigraphy

Girolamo Tartaglione

Specialty type: Radiology, nuclear medicine and medical imaging

Provenance and peer review: Invited article; Externally peer reviewed.

Peer-review model: Single blind

Peer-review report's classification

Scientific Quality: Grade B

Novelty: Grade B

Creativity or Innovation: Grade B

Scientific Significance: Grade B

P-Reviewer: Xu JD

Received: April 21, 2024

Revised: May 30, 2024

Accepted: July 1, 2024

Published online: July 28, 2024

Processing time: 93 Days and 15.6 Hours



Girolamo Tartaglione, Department of Nuclear Medicine, Cristo Re Hospital, Rome 00167, Italy

Corresponding author: Girolamo Tartaglione, MD, Chief Physician, Department of Nuclear Medicine, Cristo Re Hospital, 25 via delle Calasanziane, Rome 00167, Italy.
nmcrh@hotmail.com

Abstract

Lymphoscintigraphy is a nuclear medicine procedure that uses a small quantity of radioactive particles for visualizing the lymphatic system. Traditionally, the radiotracer was injected subcutaneously, but the quality of lymphatic path imaging was scarce due to high background. Intradermal radiotracer injection is considered the modern-day intralymphatic injection. We propose rest/stress intradermal lymphoscintigraphy for the diagnosis, staging and surgical planning of lymphedema. Major and minor findings were described in primary and secondary lymphedema. Based on the in-depth information of the lymphatic pathways, physiotherapists and microsurgeons can obtain important functional information in patients' selection to treat with physical treatments and/or undergo microsurgery.

Key Words: Intradermal injection; Lymphoscintigraphy; Exercise; Rest; Stress; Lymphedema; Radionuclide imaging; Lymphatic system

©The Author(s) 2024. Published by Baishideng Publishing Group Inc. All rights reserved.

Core Tip: Intradermal lymphoscintigraphy is a helpful functional nuclear imaging test that evaluates the lymphatic flow of the superficial and deeper lymphatic pathways at rest as well as following short and prolonged muscular activity, thus visualizing draining lymph nodes in a single 1-hour examination. This diagnostic method may help physiotherapists to evaluate the effects of muscular exercise and physical therapy on lymph drainage and surgeons to plan microsurgical treatments in advanced clinical stages of lymphedema.

Citation: Tartaglione G. Advantages of the intradermal lymphoscintigraphy. *World J Radiol* 2024; 16(7): 241-246

URL: <https://www.wjgnet.com/1949-8470/full/v16/i7/241.htm>

DOI: <https://dx.doi.org/10.4329/wjr.v16.i7.241>

INTRODUCTION

Lymphoscintigraphy is a nuclear medicine procedure based on the injection of a little amount of radiotracer in an area of the body to visualize lymph drainage and regional lymph nodes. In the past, the radiotracers available had an acidic pH and physicians prefer subcutaneous, subfascial or submucosal injections to avoid the burning sensation at the injection site due to the presence of pH receptors in the dermis. Subcutaneous injections resulted in a slow injection site clearance, an intense liver and bladder uptake, a higher background, and a scarce quality of imaging of lymphatic pathways due to the passage of tracer in bloodstream.

When injected intradermally, the radiotracer is quickly absorbed by lymphatic capillary networks which are in the reticular and papillary dermis, offering a large surface for uptake and a better visualization of the superficial and deep lymphatic system in an amount of shorter time. Both the epidermis and subcutaneous tissue lack lymphatic capillaries. Nowadays, intradermal tracer injection is considered the modern-day intralymphatic injection for lymphatic mapping.

The ideal imaging agent should have an adequate particle size, a fast clearance, a rapid lymph node accumulation, a favourable safety profile, and a neutral injected solution pH. Currently, ^{99m}Tc-HSA nanocolloids in Europe and ^{99m}Tc-tilmanocept in ultrasound show these favorable characteristics and can thus be injected intradermally without causing any pain at the injection site. In the present paper, we describe the technical aspects and advantages of rest/stress intradermal lymphoscintigraphy in lymphedema assessment. After removing elastic sleeves or stockings, we injected intradermally two doses of 50 MBq in 0.3 mL of ^{99m}Tc-nanocolloid fractioned in strategic points based on anatomical distribution of main lymphatic collectors of the affected limb. The intermetatarsal space and the external and internal peri malleolar areas were used for the lower limb, while the first and fourth intermetacarpal space for upper limb. A resting scan is acquired at once following tracer injection. Afterward, the patient performed a two-minute muscular exercise (light weightlifting for upper limb, stepping for lower limbs) followed by a stress scan. Subsequently, the patient performed a limited by symptoms muscular exercise (squeezing for upper limb, walking for lower limbs) and a delayed scan can be acquired one hour after tracer injection. According to the severity, the test may visualize several patterns: The minor findings in lymphatic insufficiency are: (1) Delayed lymphatic drainage from injection site. When using an intradermal injection, the normal tracer appearance time in regional lymph nodes is < 10 minutes. Tracer stagnation area. At delayed scan, the radiotracer may remain along the course of the lymphatic pathway also following a prolonged muscular exercise; (2) Little tracer stagnation areas at the elbow or along lymphatic vessels in proximity of the valves might appear in clinical stage 0-1 as a subclinical sign of developing secondary lymphedema; (3) Deviation of the main lymphatic pathway. The lymph may deviate toward collectors around small saphenous or cephalic vein, instead of great saphenous or basilic vein; (4) Collateral lymphatic vessel development (< 3). The most frequent compensatory mechanism in the first stages of lymphedema; (5) Crossover drainage. In secondary lymphedema, after unilateral inguinal lymph node dissection or in breast cancer patients after axillary lymph node clearance, the lymph may cross the midline onto the contralateral side; (6) Deep vessels. Progressive functional damage to the main superficial lymphatic vessels due to genetic causes or lymph node dissection is common in lymphoedema patients. The deep lymphatic vessels can support lymphatic drainage and can be visualized in a delayed scan after prolonged exercise. The deep lymphatics can be recognized by the uptake of tracers in the popliteal or epitrochlear nodes; and (7) Tortuous course of lymph vessel. Tortuous vessels are more often seen in early-stage lipedema and filariasis.

The major findings in lymphatic insufficiency are: (1) Lymphangiectasia is a pathologic dilation of lymph vessels with tracer stagnation that may appear in both primary and secondary lymphedema; (2) Extravasation of tracer (or lymphatic leaking) is more commonly observed following an interruption of the lymphatic system due to increased resistance to lymphatic flow and partial leakage of lymph. This pattern may be an early sign of secondary lymphedema if it is located near the elbow, groin or middle third of the legs; (3) Dermal backflow is a consequence of restricted or largely obstructed lymphatic flow. It can be seen more often in delayed scans after prolonged muscular activity. The mechanism of dermal backflow is that muscular exercise increases intraluminal pressure within the lymphatic vessel, pushing lymph ahead. However, in patients with lymphedema, the increased resistance to lymph flow may determine an incompetence of anti-reflux valves, and the lymph exits from lymphatic collectors returning into the cutaneous surface of the limb. Dermal backflow may be proximal or distal. In advanced clinical stages after an extensive surgical lymphadenectomy and/or radiation treatment, the entire limb may be involved. In areas affected by dermal backflow, lymphatic pathways visualization may be difficult or hardly recognizable; (4) Absent number of vessels. In patients with primary lymphedema, imaging of the main superficial pathways may be difficult due to damage or compromised functionality; (5) Absent number of nodes. Fewer or no lymph nodes following surgical dissection and/or radiation therapy can cause an accumulation of excess lymph fluid in the tissues with damaged drainage; and (6) No flow. No lymphatic flow may develop in patients with acute lymphangitis or in severe clinical stages of lymphedema. To better define the extension of the damage, we recommend reinjecting small doses of radiotracer in various parts of the limb.

These findings can appear or change after a prolonged muscular exercise (delayed scan). In any case, radiotracer extravasation from lymphatic collectors is the most significant sign of lymphedema (Figure 1). Lymphoscintigraphy can be useful for detecting lymphatic leakage as a frequent complication in vascular surgery or after kidney transplantation. It is due to the trauma of lymphatic system. Indocyanine green lymphangiography with embolization can both be used in diagnosis and therapy to close the leakage.

LYMPHOSCINTIGRAPHY IN LYMPHEDEMA MANAGEMENT

Lymphedema is a chronic condition caused by a damage of lymphatic system characterized by progressive swelling of

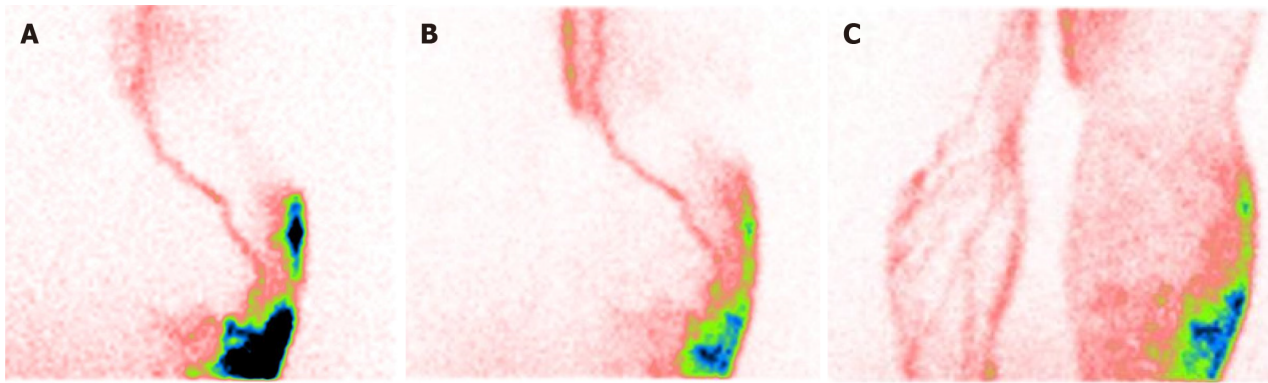


Figure 1 Intradermal lymphoscintigraphy in lower limbs secondary lymphedema. A: Resting scan; B: Stress scan; C: Delayed scan.

the limbs or other area of the body due to impaired lymphatic drainage. Lymphedema is most often a complication of cancer surgical or radiation treatment or parasitic infections, but it can also be a consequence of genetic disorders. Surgical removal or injury to lymph nodes and lymph vessels and radiation treatment for cancer radiation may result in secondary lymphedema. Lymphedema usually develops within 1-3 years after surgery, or 30 days after radiotherapy. It is important to note that lymphedema can progress through these stages over time, so early detection and treatment are key to managing the condition and preventing complications. Physical treatments for lymphedema may include physical therapy, compression garments, multilayer compression bandaging, compression devices, and exercise.

The muscle movement from exercise and a progressive resistance training improve the flow of lymph, which may help treat lymphedema. The American College of Sports Medicine recommends that a supervised exercise program is safe for patients with or at risk for lymphedema after cancer treatments. Muscular exercise as first-line treatment is a part of a healthy lifestyle and is essential for effective secondary lymphedema management. Before starting any exercise program, individuals should be cleared for the program of activity. Rest/stress intradermal lymphoscintigraphy may be performed in patients at risk to develop a secondary lymphedema to evaluate the direct effects of muscular exercise on lymph drainage. The scan may show subclinical findings of lymphedema as little tracer stagnation areas near valves of main lymphatic collector, at elbow or at middle third of legs. The evidence of draining lymph nodes of axilla or groins is an essential element to consider before starting muscular exercise program safely.

Today, lymphedema treatment is a combination of conservative and operative methods. Complex physical therapy is the first-line treatment and can be divided into two phases: A first, intensive phase composed of manual lymphatic drainage, skin care, muscular activity and/or compression, followed by a second phase to stabilize and conserve the results obtained through daily elastic compression garments. Surgical treatment options, in conjunction with conservative treatments, may provide clinical improvement and limb volume reduction[1]. Surgical therapies can be divided into reconstructive lymphatico-venous anastomosis (LVA) and vascular lymph node transfer, and ablatives (liposuction and dermolipectomy). LVA creates a bypass through which excess interstitial fluid excess may be drained directly into the venous system. Vascular lymph node transfer comprises the transplant of vascularized autologous lymph nodes from an unaffected region anatomized to recipient vessels in the lymphedematous area. Although the precise mechanism is still unknown, it is hypothesized that the transferred lymph nodes establish an effective shunting system *via* lymph angiogenesis to drain interstitial fluid into the venous system[2].

Diagnosis is based on anamnesis, clinical findings, and imaging. Imaging of the lymphatic system plays a fundamental role in diagnosing of lymphedema. Various imaging modalities may image the lymphatic system such as lymphography, lymphoscintigraphy, magnetic resonance imaging, computed tomography (CT), and ultra-high frequency ultrasound (UHFUS). A strict cooperation between surgeon, physiotherapist, radiologist, and nuclear physician is strongly recommended for a better use of technologies available[3].

Usually, there is no specific preparation for a patient receiving lymphoscintigraphy. However, in advanced clinical stage we prefer imaging patients only after an intensive decongestive treatment. Radiotracer injection sites may vary due to discrepancies among protocols[4-8]. In our experience, we performed intradermal radiotracer injections in specific points previously agreed with the microsurgeon, at the distal part of the affected limb. We recommend injecting in areas of skin where the dermis is well represented, avoiding scars or areas with dermatitis. Rest/stress intradermal lymphoscintigraphy is a method for diagnosing lymphedema, which involves injecting a radioactive tracer into the dermis and taking images of the superficial and deep lymphatic system and draining lymph nodes at rest and after exercise. The exercise stimulates the lymphatic flow and reveals any abnormalities in the lymphatic pathways. For the lower limbs, the injection point used are the first intermetatarsal space and the external and internal peri malleolar areas while for the upper limbs, the first and fourth intermetacarpal space. A reinjection at distal radial and ulnar epiphyses can be suggested in patients with swollen back of hand. A needle is inserted at 10-15-degree angle, 1-2 mm beneath the skin surface to perform an intradermal injection of 0.3 mL of ^{99m}Tc -nanocolloid. A resting scan is performed following tracer injection. The patient is then asked to perform a short exercise for 2 minutes followed by a second scan (stress). Subsequently the patient performs a prolonged muscular exercise for 30 to 40 minutes, limited by symptoms. A third and final delayed scan is performed one hour after tracer injection. In our experience, intradermal injections around the malleolar areas or heel most commonly provide a path of lymph drainage to the popliteal lymph nodes (deep lymphatic collectors)[9]. Stress activity can also be performed following radiotracer injection as it has been shown to improve lymph

drainage and increase radiotracer uptake into the lymph nodes. Lower limb stress includes walking or cycling, while upper limb stress can vary between hand gripping and lifting light weights. This method is a functional-imaging test which evaluates lymphatic flow of the superficial and deep lymphatic pathways at rest as well as following a short and prolonged muscular activity, thus visualizing draining lymph nodes in a single 1-hour examination.

With a detailed knowledge of the lymphatic pathway, the visual assessment of lymphoscintigraphy provides information regarding patent lymphatic drainage patterns, lymph nodes, collateral circulation, as well as the direction of lymph flow and potential disruptions in the affected limb[10]. In secondary lymphedema, the uptake of draining lymph nodes in atypical sites are indicative of rearrangement of the lymphatic flow. The transport index (TI) is a semi-quantitative evaluation of lymphatic flow that considers five factors noted when performing lymphoscintigraphy: Transport kinetics, distribution pattern of the radiotracer, time to visualization of lymph nodes, quality of visualization of lymph nodes, and visualization of lymphatic vessels[11]. A score ranging from 0 to 9 indicates a normal score while a score greater than 10 signals a pathological finding. In 2022, we described how pathological elements seen at rest/stress intradermal lymphoscintigraphy can be subdivided into major and minor findings[12]. In patients with secondary lymphoedema, a significantly higher percentage of serious findings such as lymph congestion, tracer extravasation and dermal reflux were seen. While a significantly higher percentage of minor findings, such as deep lymphatic vessels and radiotracer uptake at the epitrochlear and popliteal lymph nodes were observed in patients with primary lymphedema. Extensive dermal backflow and the absence of a draining lymph node are signs of severe clinical stages of lymphoedema. In our experience, we found a significantly higher incidence of dermal backflow in secondary lymphoedema as a result of medical procedures such as radiotherapy and surgical treatments for cancer. A scarce or absent visualization of lymphatic vessels in all phases of study, or a wide extent of dermal-backflow, and no evidence of lymph nodes (also after superficial and deeper re-injection in other sites) are related to more severe clinical stages of lymphedema.

The information obtained from lymphoscintigraphy renders it a reference exam in the decision-making process of selecting lymphedema patient who are microsurgical candidates and the development of personalized surgical treatment plans. Vaqueiro *et al*[13] report the use of lymphoscintigraphy for diagnosis and patient selection to undergo microvascular procedures, such as LVA, in patients with patent lymphatic channels at imaging. Campisi *et al*[14] describe the use of lymphatic microsurgery in patients with early-stage lymphedema with a lymphoscintigraphy that shows a low inguinal or axillary lymph nodal uptake and a minimal or absent passage of the tracer beyond this proximal lymph nodal area. Maegawa *et al*[15] indicate a relationship between lymphoscintigraphic findings and indications for lymphatic microsurgery in patients with secondary lower limb lymphedema. According to their observations, lymphoscintigraphic images can be divided into five types and suggest type 3 (no inguinal lymph nodes detected, dermal backflow in the thigh and/or leg, lymph stasis is observed) is the most suitable for LVA. A similar relationship was described by Mikami *et al*[16] between lymphoscintigraphic findings and indications for lymphatic microsurgery in patients with secondary upper limb lymphedema. Their results revealed lymphoscintigraphic images can be divided into five major types and three subtypes and suggest LVA should be considered as a treatment option for lymphedema types II-V. Boccardo *et al* [17] report a clinical and instrumental selection of 74 women with a history of axillary lymph node dissection for breast cancer with the use of lymphoscintigraphy. Patients with a body mass index less than 30 kg/m² and a TI score greater than 10 on lymphoscintigraphy were indications for Lymphatic Microsurgical Preventing Healing technique. Gentileschi *et al*[18] underline the feasibility of single photon emission CT/CT combined with ultrasound fusion imaging for the preoperative identification of groin efferent lymph node in patients scheduled for peripheric lymphaticovenular anastomosis. In severe clinical stages of lymphedema[19], Visconti *et al*[20] suggest an integration of nuclear imaging with UHFUS, that may help detecting the lymphatic vessels and evaluating their degeneration status, including wall and lumen characteristics.

Lymphoscintigraphy plays a leading role in the early diagnosis, may help evaluate the effects of muscular exercise and physical therapy on lymphedema, and plan microsurgical treatments such as lymphatic-venous anastomosis or vascularized lymph node transfer. Thanks to a suitable energy of radioactive signal the lymphoscintigraphy is the best modality for lymphatic imaging in obese and lipedema patients or for identification of sentinel node in unexpected site. However, it has a few limitations. First, there is no universally standardized imaging protocol, and each lymphedema center performs a different and personalized imaging modality. The imaging protocol can vary according to the extension of lymphedema, the radiotracer, radioactivity dose and injected volume, number of injections, injection site and plane, and if performed at rest or in conjunction with a stress activity. Secondly, lymphoscintigraphy is characterized by a limited spatial resolution making it more difficult to find lymphatic pathways in the three-dimensional space. In the lymphoscintigraphic images of lymphedema patients, pathological findings such as collateral lymphatic pathways and dermal backflow can impede the visualization of patent lymphatic vessels. In our experience, dorsal lymphatic pathways of the arm can overlap the lymphatic vessels that follow the cephalic vein in upper limb lymphedema. Likewise, anterior collateral lymphatic pathways can overlap the lymphatic vessels that follow the small saphenous vein in lower limb lymphedema. Nevertheless, the limited three-dimensional anatomic definition with lymphoscintigraphy can be overcome by taking anterior and posterior scans of the affected limb. By seeing the lymphatic pathways from multiple points of view, the two-dimensional lymphoscintigraphy images provide information of a three-dimensional space. Moreover, lymphoscintigraphy does not provide direct information about the quality of the lymphatic vessels. However, a qualitative analysis of lymphoscintigraphic findings may correlate to lymphatic vessel quality as seen intraoperatively. In our experience, patent lymphatic channels are more commonly found in patients with a lymphoscintigraphy that displays a linear pattern, ectasia, or radiotracer stasis. On the other hand, lymphatic channels tend to be sclerotic if dermal backflow and radiotracer extravasation are seen with lymphoscintigraphy. Nevertheless, in a surgical perspective an integration with UHFUS imaging may be suggested.

CONCLUSION

Lymphoscintigraphy plays a leading role in the early diagnosis, may help evaluate the effects of muscular exercise and physical therapy on lymphedema, and plan microsurgical treatments such as lymphatic-venous anastomosis or vascularized lymph node transfer. Thanks to a suitable energy of radioactive signal the lymphoscintigraphy is the best modality for lymphatic imaging in obese and lipedema patients or for identification of sentinel node in unexpected site. However, it has a few limitations. First, there is no universally standardized imaging protocol, and each lymphedema center performs a different and personalized imaging modality. The imaging protocol can vary according to the extension of lymphedema, the radiotracer, radioactivity dose and injected volume, number of injections, injection site and plane, and if performed at rest or in conjunction with a stress activity. Secondly, lymphoscintigraphy is characterized by a limited spatial resolution making it more difficult to find lymphatic pathways in the three-dimensional space. In the lymphoscintigraphic images of lymphedema patients, pathological findings such as collateral lymphatic pathways and dermal backflow can impede the visualization of patent lymphatic vessels. In our experience, dorsal lymphatic pathways of the arm can overlap the lymphatic vessels that follow the cephalic vein in upper limb lymphedema. Likewise, anterior collateral lymphatic pathways can overlap the lymphatic vessels that follow the small saphenous vein in lower limb lymphedema. Nevertheless, the limited three-dimensional anatomic definition with lymphoscintigraphy can be overcome by taking anterior and posterior scans of the affected limb. By seeing the lymphatic pathways from multiple points of view, the two-dimensional lymphoscintigraphy images provide information of a three-dimensional space. Moreover, lymphoscintigraphy does not provide direct information about the quality of the lymphatic vessels. However, a qualitative analysis of lymphoscintigraphic findings may correlate to lymphatic vessel quality as seen intraoperatively. In our experience, patent lymphatic channels are more commonly found in patients with a lymphoscintigraphy that displays a linear pattern, ectasia, or radiotracer stasis. On the other hand, lymphatic channels tend to be sclerotic if dermal backflow and radiotracer extravasation are seen with lymphoscintigraphy. Nevertheless, in a surgical perspective an integration with UHFUS imaging may be suggested.

FOOTNOTES

Author contributions: Tartaglione G conceived and authored the paper.

Conflict-of-interest statement: The author reports no relevant conflicts of interest for this article.

Open-Access: This article is an open-access article that was selected by an in-house editor and fully peer-reviewed by external reviewers. It is distributed in accordance with the Creative Commons Attribution NonCommercial (CC BY-NC 4.0) license, which permits others to distribute, remix, adapt, build upon this work non-commercially, and license their derivative works on different terms, provided the original work is properly cited and the use is non-commercial. See: <https://creativecommons.org/licenses/by-nc/4.0/>

Country of origin: Italy

ORCID number: Girolamo Tartaglione [0000-0002-1764-5230](https://orcid.org/0000-0002-1764-5230).

S-Editor: Wang JJ

L-Editor: A

P-Editor: Che XX

REFERENCES

- 1 **Executive Committee of the International Society of Lymphology.** The diagnosis and treatment of peripheral lymphedema: 2020 Consensus Document of the International Society of Lymphology. *Lymphology* 2020; **53**: 3-19 [PMID: [32521126](https://pubmed.ncbi.nlm.nih.gov/32521126/)]
- 2 **Liu HL,** Pang SY, Lee CC, Wong MM, Chung HP, Chan YW. Orthotopic transfer of vascularized groin lymph node flap in the treatment of breast cancer-related lymphedema: Clinical results, lymphoscintigraphy findings, and proposed mechanism. *J Plast Reconstr Aesthet Surg* 2018; **71**: 1033-1040 [PMID: [29550286](https://pubmed.ncbi.nlm.nih.gov/29550286/) DOI: [10.1016/j.bjps.2018.02.015](https://doi.org/10.1016/j.bjps.2018.02.015)]
- 3 **Tartaglione G,** Pagan M, Ieria FP, Visconti G, Tartaglione T. Imaging the Lymphatic System. *Radiology-Nuclear Medicine Diagnostic Imaging* 2023 [DOI: [10.1002/9781119603627.ch27](https://doi.org/10.1002/9781119603627.ch27)]
- 4 **Yoon JA,** Shin MJ, Shin YB, Kim K, Park H, Kang T, Kong IJ, Kim H, Park MS, Kim JH. Correlation of ICG lymphography and lymphoscintigraphy severity stage in secondary upper limb lymphedema. *J Plast Reconstr Aesthet Surg* 2020; **73**: 1982-1988 [PMID: [32952056](https://pubmed.ncbi.nlm.nih.gov/32952056/) DOI: [10.1016/j.bjps.2020.08.055](https://doi.org/10.1016/j.bjps.2020.08.055)]
- 5 **Akita S,** Mitsukawa N, Kazama T, Kuriyama M, Kubota Y, Omori N, Koizumi T, Kosaka K, Uno T, Satoh K. Comparison of lymphoscintigraphy and indocyanine green lymphography for the diagnosis of extremity lymphoedema. *J Plast Reconstr Aesthet Surg* 2013; **66**: 792-798 [PMID: [23523168](https://pubmed.ncbi.nlm.nih.gov/23523168/) DOI: [10.1016/j.bjps.2013.02.023](https://doi.org/10.1016/j.bjps.2013.02.023)]
- 6 **Imai H,** Yoshida S, Mese T, Roh S, Fujita A, Sasaki A, Nagamatsu S, Koshima I. Correlation between Lymphatic Surgery Outcome and Lymphatic Image-Staging or Clinical Severity in Patients with Lymphedema. *J Clin Med* 2022; **11** [PMID: [36078909](https://pubmed.ncbi.nlm.nih.gov/36078909/) DOI: [10.3390/jcm11174979](https://doi.org/10.3390/jcm11174979)]
- 7 **Sherman AI,** Ter-Pogossian M. Lymph-node concentration of radioactive colloidal gold following interstitial injection. *Cancer* 1953; **6**: 1238-1240 [PMID: [13106841](https://pubmed.ncbi.nlm.nih.gov/13106841/) DOI: [10.1002/1097-0142\(195311\)6:6<1238::aid-cnrcr2820060618>3.0.co;2-6](https://doi.org/10.1002/1097-0142(195311)6:6<1238::aid-cnrcr2820060618>3.0.co;2-6)]

- 8 **Szuba A**, Shin WS, Strauss HW, Rockson S. The third circulation: radionuclide lymphoscintigraphy in the evaluation of lymphedema. *J Nucl Med* 2003; **44**: 43-57 [PMID: [12515876](#)]
- 9 **Shinaoka A**, Koshimune S, Yamada K, Kumagishi K, Suami H, Kimata Y, Ohtsuka A. Correlations between Tracer Injection Sites and Lymphatic Pathways in the Leg: A Near-Infrared Fluorescence Lymphography Study. *Plast Reconstr Surg* 2019; **144**: 634-642 [PMID: [31461017](#) DOI: [10.1097/PRS.0000000000005982](#)]
- 10 **Villa G**, Campisi CC, Ryan M, Boccardo F, Di Summa P, Frascio M, Sambuceti G, Campisi C. Procedural Recommendations for Lymphoscintigraphy in the Diagnosis of Peripheral Lymphedema: the Genoa Protocol. *Nucl Med Mol Imaging* 2019; **53**: 47-56 [PMID: [30828401](#) DOI: [10.1007/s13139-018-0565-2](#)]
- 11 **Gale RP**, Graze PR, Wells J, Ho W, Hershko C, Lowenberg B, Feig S, Cline MJ. Autologous bone marrow transplantation in patients with cancer. *Exp Hematol* 1979; **7** Suppl 5: 351-359 [PMID: [400697](#) DOI: [10.1007/BF00251310](#)]
- 12 **Tartaglione G**, Ieria FP, Visconti G, Bartoletti R, Tarantino G, Aloisi D, Gentileschi S, Salgarello M. Rest/Stress Intradermal Lymphoscintigraphy for the Functional Imaging of the Lymphatic System. *Clin Nucl Med* 2022; **47**: 1011-1018 [PMID: [36183418](#) DOI: [10.1097/RLU.0000000000004422](#)]
- 13 **Vaqueiro M**, Gloviczki P, Fisher J, Hollier LH, Schirger A, Wahner HW. Lymphoscintigraphy in lymphedema: an aid to microsurgery. *J Nucl Med* 1986; **27**: 1125-1130 [PMID: [3723188](#)]
- 14 **Campisi C**, Eretta C, Pertile D, Da Rin E, Campisi C, Macciò A, Campisi M, Accogli S, Bellini C, Bonioli E, Boccardo F. Microsurgery for treatment of peripheral lymphedema: long-term outcome and future perspectives. *Microsurgery* 2007; **27**: 333-338 [PMID: [17477420](#) DOI: [10.1002/micr.20346](#)]
- 15 **Maegawa J**, Mikami T, Yamamoto Y, Satake T, Kobayashi S. Types of lymphoscintigraphy and indications for lymphaticovenous anastomosis. *Microsurgery* 2010; **30**: 437-442 [PMID: [20878726](#) DOI: [10.1002/micr.20772](#)]
- 16 **Mikami T**, Hosono M, Yabuki Y, Yamamoto Y, Yasumura K, Sawada H, Shizukuishi K, Maegawa J. Classification of lymphoscintigraphy and relevance to surgical indication for lymphaticovenous anastomosis in upper limb lymphedema. *Lymphology* 2011; **44**: 155-167 [PMID: [22458117](#)]
- 17 **Boccardo F**, Fulcheri E, Villa G, Molinari L, Campisi C, Dessalvi S, Murdaca G, Campisi C, Santi PL, Parodi A, Puppo F, Campisi C. Lymphatic microsurgery to treat lymphedema: techniques and indications for better results. *Ann Plast Surg* 2013; **71**: 191-195 [PMID: [23542829](#) DOI: [10.1097/SAP.0b013e31824f20d4](#)]
- 18 **Gentileschi S**, Albanese R, Pino V, Stefanizzi G, Fragomeni S, Zagaria L, Ieria FP, Salgarello M, Scambia G, Garganese G. SPECT/CT and fusion ultrasound to target the efferent groin lymph node for lymphatic surgery. *Microsurgery* 2019; **39**: 605-612 [PMID: [31400162](#) DOI: [10.1002/micr.30501](#)]
- 19 **Falcão RP**, Ismael SJ. Leu 7+, Leu 11a- acute T-lymphoblastic leukemia having low K cell activity and no NK cell activity. *Am J Hematol* 1987; **24**: 101-105 [PMID: [3492137](#) DOI: [10.1002/ajh.2830240113](#)]
- 20 **Visconti G**, Bianchi A, Hayashi A, Cina A, Maccauro G, Almadori G, Salgarello M. Thin and superthin perforator flap elevation based on preoperative planning with ultrahigh-frequency ultrasound. *Arch Plast Surg* 2020; **47**: 365-370 [PMID: [32718115](#) DOI: [10.5999/aps.2019.01179](#)]

Retrospective Study

Ultrasonics in liver cancer: Developing a radiomics model for differentiating intrahepatic cholangiocarcinoma from hepatocellular carcinoma using contrast-enhanced ultrasound

Li-Ya Su, Ming Xu, Yan-Lin Chen, Man-Xia Lin, Xiao-Yan Xie

Specialty type: Radiology, nuclear medicine and medical Imaging**Provenance and peer review:**

Unsolicited article; Externally peer reviewed.

Peer-review model: Single blind**Peer-review report's classification****Scientific Quality:** Grade A, Grade D**Novelty:** Grade A, Grade C**Creativity or Innovation:** Grade A, Grade C**Scientific Significance:** Grade A, Grade C**P-Reviewer:** Rizzo A, Italy**Received:** January 16, 2024**Revised:** May 10, 2024**Accepted:** May 29, 2024**Published online:** July 28, 2024**Processing time:** 189 Days and 17.4 Hours**Li-Ya Su, Ming Xu, Yan-Lin Chen, Man-Xia Lin, Xiao-Yan Xie**, Department of Medical Ultrasound, The First Affiliated Hospital, Institute of Diagnostic and Interventional Ultrasound, Sun Yat-Sen University, Guangzhou 510000, Guangdong Province, China**Co-first authors:** Li-Ya Su and Ming Xu**Co-corresponding authors:** Man-Xia Lin and Xiao-Yan Xie**Corresponding author:** Xiao-Yan Xie, MD, PhD, Director, Department of Medical Ultrasound, The First Affiliated Hospital, Institute of Diagnostic and Interventional Ultrasound, Sun Yat-Sen University, No. 58 Zhongshan Road 2, Guangzhou 510000, Guangdong Province, China. xxyl992@21cn.com

Abstract

BACKGROUND

Hepatocellular carcinoma (HCC) and intrahepatic cholangiocarcinoma (ICC) represent the predominant histological types of primary liver cancer, comprising over 99% of cases. Given their differing biological behaviors, prognoses, and treatment strategies, accurately differentiating between HCC and ICC is crucial for effective clinical management. Radiomics, an emerging image processing technology, can automatically extract various quantitative image features that may elude the human eye. Reports on the application of ultrasound (US)-based radiomics methods in distinguishing HCC from ICC are limited.

AIM

To develop and validate an ultrasonics model to accurately differentiate between HCC and ICC.

METHODS

In our retrospective study, we included a total of 280 patients who were diagnosed with ICC ($n = 140$) and HCC ($n = 140$) between 1999 and 2019. These patients were divided into training ($n = 224$) and testing ($n = 56$) groups for analysis. US images and relevant clinical characteristics were collected. We utilized the XGBoost method to extract and select radiomics features and further employed a random forest algorithm to establish ultrasonics models. We compared the diagnostic performances of these ultrasonics models with that of

radiologists.

RESULTS

Four distinct ultrasonics models were constructed, with the number of selected features varying between models: 13 features for the US model; 15 for the contrast-enhanced ultrasound (CEUS) model; 13 for the combined US + CEUS model; and 21 for the US + CEUS + clinical data model. The US + CEUS + clinical data model yielded the highest area under the receiver operating characteristic curve (AUC) among all models, achieving an AUC of 0.973 in the validation cohort and 0.971 in the test cohort. This performance exceeded even the most experienced radiologist (AUC = 0.964). The AUC for the US + CEUS model (training cohort AUC = 0.964, test cohort AUC = 0.955) was significantly higher than that of the US model alone (training cohort AUC = 0.822, test cohort AUC = 0.816). This finding underscored the significant benefit of incorporating CEUS information in accurately distinguishing ICC from HCC.

CONCLUSION

We developed a radiomics diagnostic model based on CEUS images capable of quickly distinguishing HCC from ICC, which outperformed experienced radiologists.

Key Words: Cholangiocarcinoma; Hepatocellular carcinoma; Contrast-enhanced ultrasound; Radiomics; Primary liver tumor

©The Author(s) 2024. Published by Baishideng Publishing Group Inc. All rights reserved.

Core Tip: In this study, we successfully established a novel radiomics model that leveraged contrast-enhanced ultrasound (US) for accurate discrimination between intrahepatic cholangiocarcinoma and hepatocellular carcinoma. The refined radiomics model incorporated 21 essential features, surpassing the diagnostic accuracy of seasoned radiologists. This model excelled in diagnostic performance and ease of use, requiring only three specific time-point images and by a transparent image-acquisition protocol. Its implementation enhanced diagnostic objectivity and diminished the operator-dependence inherent in US examinations. This ultrasonics-based model can provide additional diagnostic insights to radiologists of varying levels of experience, thereby elevating overall diagnostic accuracy.

Citation: Su LY, Xu M, Chen YL, Lin MX, Xie XY. Ultrasonics in liver cancer: Developing a radiomics model for differentiating intrahepatic cholangiocarcinoma from hepatocellular carcinoma using contrast-enhanced ultrasound. *World J Radiol* 2024; 16(7): 247-255

URL: <https://www.wjgnet.com/1949-8470/full/v16/i7/247.htm>

DOI: <https://dx.doi.org/10.4329/wjr.v16.i7.247>

INTRODUCTION

Primary liver cancer ranks as the sixth most common cancer globally and the third-leading cause of cancer-related mortality, with the fifth highest incidence and fourth highest mortality rates[1]. Hepatocellular carcinoma (HCC) and intrahepatic cholangiocarcinoma (ICC) represent the predominant histological types, comprising over 99% of cases[2]. Effective treatments such as resection, liver transplantation, and ablation are available for early-stage HCC or ICC. However, for lesions diagnosed at an advanced, incurable stage, systematic treatment varies significantly between these tumor types[3,4], necessitating distinct therapeutic approaches. Given their differing biological behaviors, prognoses, and treatment strategies, accurately differentiating between HCC and ICC is crucial for effective clinical management.

Over the past decade, contrast-enhanced ultrasound (CEUS) has been extensively studied across various domains, achieving notable success in characterizing focal liver lesions. Numerous studies have attempted to distinguish between ICC and HCC using CEUS, yielding promising findings. For instance, Liu *et al*[5] reported an area under the receiver operating characteristic (ROC) curve (AUC) of 0.808 in differentiating ICC from HCC, highlighting the high efficiency of peripheral rim-like enhancement and rapid contrast washout in these distinctions.

Despite advancements in modern imaging techniques, standard imaging modalities and qualitative image analysis often fall short of conclusively differentiating between ICC and HCC, especially in early-stage tumors[6]. Radiomics, an emerging image processing technology, can automatically extract various quantitative image features that may elude the human eye[7]. For example, Lewis *et al*[8] utilizing magnetic resonance imaging (MRI)-based radiomics, achieved an AUC of 0.900 in the differential diagnosis of ICC from HCC by incorporating radiomics with patient sex and Liver Imaging Reporting and Data Systems criteria.

Reports on the application of ultrasound (US)-based radiomics methods in distinguishing HCC from ICC are limited. Our research aimed to develop and validate an ultrasonics model to accurately differentiate between HCC and ICC.

MATERIALS AND METHODS

Patient characteristics

All patients diagnosed with liver cancer at our institution from 1999 to 2019 underwent CEUS. Prior to analysis, all patient data were fully anonymized. The inclusion criteria were: (1) Availability of preoperative CEUS images; and (2) Surgical excision or biopsy with pathological examination. Exclusion criteria included: (1) Lack of histopathological evaluation by surgery or biopsy; (2) Incomplete clinical data (CL); and (3) Substandard CEUS image quality. Consequently, 280 patients with pathological diagnoses of ICC ($n = 140$) and HCC ($n = 140$) were retrospectively included in the study from January 1999 to December 2019.

We divided the cohort into two groups: 224 patients for the training set; and 56 patients for the testing set. The workflow is depicted in [Figure 1](#). Clinical characteristics of the patients, including sex, age, hepatitis B virus (HBV) infection, alpha-fetoprotein (AFP), and carbohydrate antigen 19-9 (CA19-9), were collected from admission records, as shown in [Table 1](#).

US images acquisition protocol

All enrolled patients underwent preoperative CEUS *via* convex array scanners (Canon/Supersonic Explorer/Esaote/Mindray) with a frequency range of 1.0 to 6.0 MHz. For patients with multiple liver lesions, the largest lesion was targeted. The ultrasound contrast agent, Sonovue, was administered through the antecubital vein as a bolus (within 1-2 s), followed by a 5 mL flush of 0.9% normal saline using a 20-gauge cannula. CEUS clips were recorded for 90 s following the injection of Sonovue. Additional CEUS images were captured at 120 s and subsequently every 60 s until the contrast washed out.

The ultrasound images ([Figure 2](#)) obtained included: (1) US. Baseline US image of the target lesion with optimal image depth and gain (standard plane); (2) Arterial enhancement (AE). CEUS image in the arterial phase showing peak enhancement of the target lesion in the standard plane; and (3) Portal enhancement (PE). CEUS image of the target lesion at 120 s in the standard plane.

Establishing radiomics model in the training cohort

The whole tumor segmentation was manually delineated in Labelme by an abdominal radiologist with 6 years of experience in liver CEUS and validated by a senior abdominal radiologist with 10 years of experience. Regions of interests (ROIs) were manually segmented along the tumor contour on all US images. The Image preprocessing and feature extraction were performed by Pyradiomics package.

Eight hundred and twenty-eight features were extracted from each region of interest, as listed in [Table 2](#). The significance of each feature was calculated using XGBoost, and the top 20 significant features were selected for further analysis. The relationships among these features were assessed using the Spearman correlation coefficient. The less significant feature was discarded for radiomics features with a SCC greater than 0.8. The remaining features were chosen for subsequent analysis. A random forest algorithm was utilized to establish the radiomics model.

We developed four models and compared their performance to determine the most efficient one. These models include the US model (using US images), the CEUS model (using AE and PE images), the US + CEUS model (combining US, AE, and PE images), and the US + CEUS + CL model (integrating US, AE, and PE images with clinical characteristics).

Model analysis and evaluation

The ROC curves were plotted, and metrics such as the AUC, accuracy, sensitivity, specificity, and precision were calculated to evaluate the predictive efficacy of each model in both training and test cohorts. Three radiologists with varying levels of experience (3, 8, and 11 years in liver CEUS) reviewed the images of all cases and made diagnoses. The diagnostic performances of the radiomic models and the radiologists were compared using the DeLong test. A decision curve was plotted to assess the clinical utility of the model by quantifying the net benefits at different risk thresholds.

Statistical analysis

Statistical analysis was conducted with SPSS 22.0 (IBM Corp., Armonk, NY, United States). Continuous variables were expressed as the means \pm standard deviation. Categorical variables were reported as numbers and percentages and were compared by the χ^2 test. Clinical features were analyzed for statistical differences in the training and test cohorts by Student's *t*-test, Mann-Whitney *U* test, Wilcoxon test, χ^2 test, or Fisher's exact test, as appropriate.

The reported statistical significance levels were all two-sided, and *P* values of less than 0.05 were considered statistically significant. Calibration diagnostic accuracy was expressed as the AUC, and the resulting specificity, sensitivity, positive predictive value, and negative predictive value were calculated. The DeLong test was used to compare AUC values.

RESULTS

Patient characteristics

The final study cohort consisted of 280 patients (HCC = 140; ICC = 140) randomly divided into a training cohort ($n = 224$; HCC = 112; ICC = 112) and a validation cohort ($n = 56$; HCC = 28; ICC = 28). The primary characteristics of all patients and lesions are shown in [Table 1](#). There was no significant difference in age, sex, HBV infection, and tumor size ($P > 0.05$).

Table 1 Basic characteristics of patients and lesions

Characteristics	HCC, <i>n</i> = 140	ICC, <i>n</i> = 140	<i>P</i> value
Age in yr	53.39 + 11.85	57.46 + 11.39	0.58
	26-79	33-86	
Sex			0.311
Male	126	120	
Female	14	20	
HBV (+)	126	106	0.562
Lesion size in cm	66.37 + 27.38	69.04 + 32.68	0.271
AFP in µg/L			0.001
> 20	91	18	
< 20	49	122	
CA19-9 in U/mL			0.001
> 34	15	83	
< 34	125	57	

AFP: Alpha-fetoprotein; CA19-9: Carbohydrate antigen 19-9; HBV: Hepatitis B virus; HCC: Hepatocellular carcinoma; ICC: Intrahepatic cholangiocarcinoma.

Table 2 Radiomic features in the radiomic analysis

Types	Features
Shape (<i>n</i> = 9)	Elongation, MajorAxisLength, MaximumDiameter, MeshSurface, MinorAxisLength, Perimeter, PerimeterSurfaceRatio, PixelSurface, Sphericity
First order (<i>n</i> = 18)	10Percentile, 90Percentile, Energy, Entropy, InterquartileRange, Kurtosis, Maximum, MeanAbsoluteDeviation, Mean, Median, Minimum, Range, RobustMeanAbsoluteDeviation, RootMeanSquared, Skewness, TotalEnergy, Uniformity, Variance
GLCM (<i>n</i> = 22)	Autocorrelation, JointAverage, ClusterProminence, ClusterShade, ClusterTendency, Contrast, Correlation, DifferenceAverage, DifferenceEntropy, DifferenceVariance, JointEnergy, JointEntropy, Imc1, Imc2, Idm, Idmn, Id, Idn, InverseVariance, MaximumProbability, SumEntropy, SumSquares
GLRLM (<i>n</i> = 16)	GrayLevelNonUniformity, GrayLevelNonUniformityNormalized, GrayLevelVariance, HighGrayLevelRunEmphasis, LongRunEmphasis, LongRunHighGrayLevelEmphasis, LongRunLowGrayLevelEmphasis, LowGrayLevelRunEmphasis, RunEntropy, RunLengthNonUniformity, RunLengthNonUniformityNormalized, RunPercentage, RunVariance, ShortRunEmphasis, ShortRunHighGrayLevelEmphasis, ShortRunLowGrayLevelEmphasis
GLSZM (<i>n</i> = 16)	GrayLevelNonUniformity, GrayLevelNonUniformityNormalized, GrayLevelVariance, HighGrayLevelZoneEmphasis, LargeAreaEmphasis, LargeAreaHighGrayLevelEmphasis, LargeAreaLowGrayLevelEmphasis, LowGrayLevelZoneEmphasis, SizeZoneNonUniformity, SizeZoneNonUniformityNormalized, SmallAreaEmphasis, SmallAreaHighGrayLevelEmphasis, SmallAreaLowGrayLevelEmphasis, ZoneEntropy, ZonePercentage, ZoneVariance
GLDM (<i>n</i> = 14)	DependenceEntropy, DependenceNonUniformity, DependenceNonUniformityNormalized, DependenceVariance, GrayLevelNonUniformity, GrayLevelVariance, HighGrayLevelEmphasis, LargeDependenceEmphasis, LargeDependenceHighGrayLevelEmphasis, LargeDependenceLowGrayLevelEmphasis, LowGrayLevelEmphasis, SmallDependenceEmphasis, SmallDependenceHighGrayLevelEmphasis, SmallDependenceLowGrayLevelEmphasis
NGTDM (<i>n</i> = 5)	Busyness, Coarseness, Complexity, Contrast, Strength

Imagetype: Original, Log-sigma-2-0-mm-3D, Log-sigma-3-0-mm-3D, Log-sigma-4-0-mm-3D, Wavelet-H, wavelet-L, lbp-2D, square, squareroot, logarithm, exponential. GLCM: Gray Level Concurrence Matrix; GLDM: Gray Level Dependence Matrix; GLRLM: Gray Level Run-Length Matrix; GLSZM: Gray Level Size-one Matrix; NGTDM: Neighborhood Gray-Tone Difference Matrix.

However, the levels of AFP and CA19-9 demonstrated significant differences between HCC and ICC (*P* < 0.05). Five clinical characteristics, age, sex, HBV infection, AFP, and CA19-9, were subsequently included in the radiomics model.

Radiomics analysis

Independent significant features were identified for each model using XGBoost and Spearman correlation coefficient. The number of features selected was 13 for the US model, 15 for the CEUS model, 13 for the US + CEUS model, and 21 for the

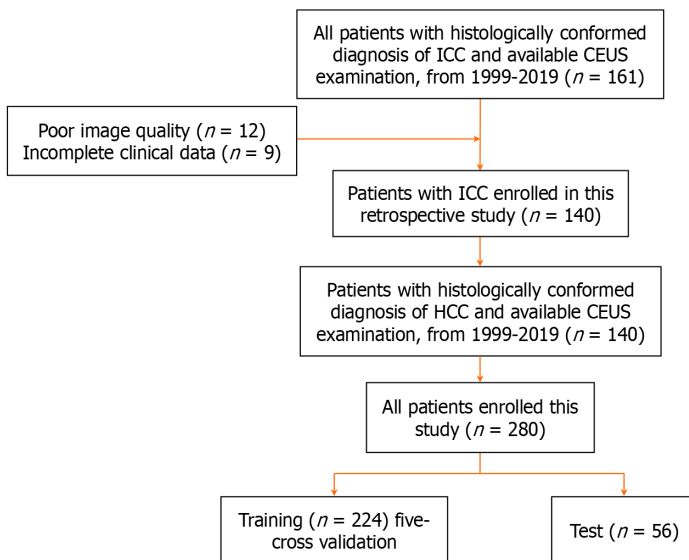


Figure 1 Workflow of necessary steps in current study. CEUS: Contrast-enhanced ultrasound; HCC: Hepatocellular carcinoma; ICC: Intrahepatic cholangiocarcinoma.

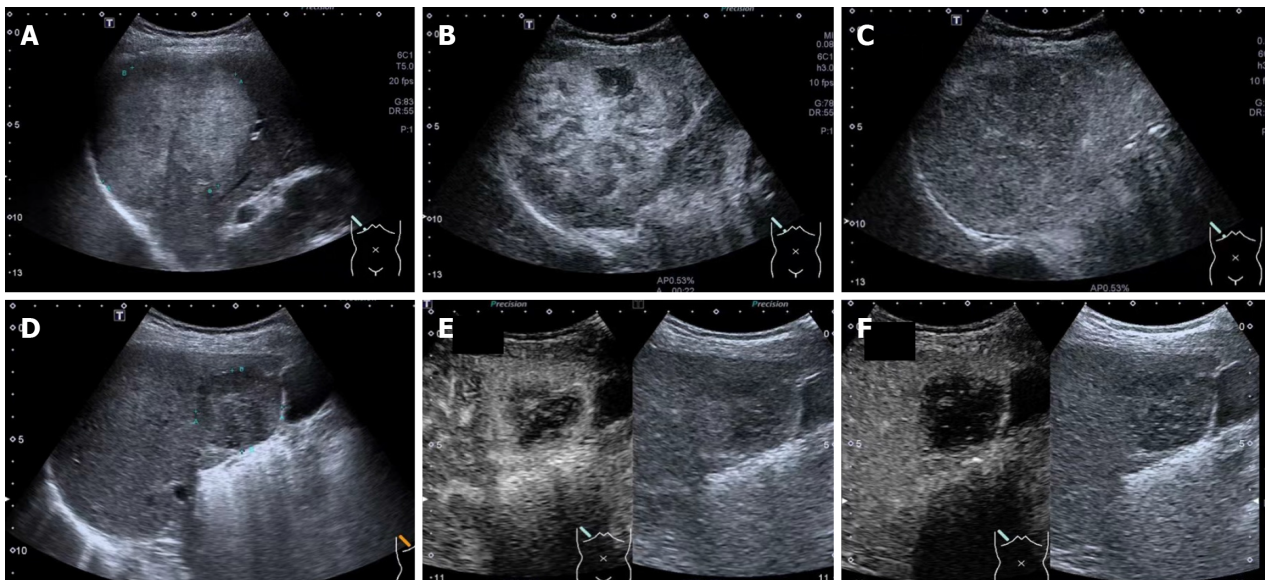


Figure 2 Image acquisition illustration. A and D: Baseline ultrasound (US) images of two target lesions; B and E: Contrast-enhanced ultrasound (CEUS) images of the target lesions at peak enhancement of arterial phase; C and F: CEUS images of the target lesions at 120 s after injection of contrast agent.

US + CEUS + CL. Four radiomic models were constructed using the random forest algorithm.

Model establishment and validation

ROC analysis results are depicted in [Figure 3](#), and a summary of the model outcomes is provided in [Table 3](#). Our study's radiomics model based on a single US image achieved an AUC of 0.822 in the validation cohort and 0.816 in the test cohort.

The CEUS model demonstrated a significant increase in AUC compared to the US model in both cohorts. In the validation cohort, the AUC for the CEUS model was 0.956, and in the test cohort the AUC was 0.919. The AUC for the US + CEUS model was higher (training cohort = 0.964, test cohort = 0.955) than that for the US model alone, indicating a significant benefit from adding CEUS information in distinguishing ICC from HCC. The AUC for the US + CEUS + CL was the highest among all models, with 0.973 in the validation cohort and 0.971 in the test cohort.

AUCs for three radiologists with different experience levels (3, 8, and 11 years in liver CEUS) were 0.786, 0.964, and 0.839, respectively. These results show that the AUC of the US + CEUS + CL was slightly higher than that of the most experienced radiologist.

The decision curve analysis is shown in [Figure 3](#). CEUS provided a significantly increased benefit compared to US alone. Moreover, the models that included more information, such as US, CEUS, and clinical characteristics,

Table 3 Area under the receiver operating characteristic curve, sensitivity, specificity, accuracy, positive predict value, and negative predict value of radiomics models in different cohorts

Parameter	Training				Validation				Test			
	US	AE + PE	US + AE + PE	US + AE + PE + CL	US	AE + PE	US + AE + PE	US + AE + PE + CL	US	AE + PE	US + AE + PE	US + AE + PE + CL
AUC (95%CI)	0.885 (0.825, 0.889)	0.955 (0.919, 0.962)	0.966 (0.934, 0.972)	0.975 (0.941, 0.975)	0.822 (0.738, 0.863)	0.956 (0.856, 0.962)	0.964 (0.907, 0.977)	0.973 (0.933, 0.983)	0.816 (0.690, 0.825)	0.919 (0.876, 0.959)	0.955 (0.907, 0.967)	0.971 (0.916, 0.980)
Sensitivity	0.766	0.933	0.900	0.911	0.727	0.909	0.818	0.863	0.607	0.714	0.928	0.892
Specificity	0.853	0.842	0.876	0.921	0.681	0.818	0.909	0.954	0.857	0.857	0.857	0.928
Accuracy	0.810	0.888	0.888	0.916	0.704	0.863	0.863	0.909	0.732	0.785	0.892	0.910
PPV	0.841	0.857	0.880	0.921	0.695	0.833	0.900	0.950	0.809	0.833	0.866	0.925
NPV	0.783	0.925	0.896	0.911	0.714	0.900	0.833	0.875	0.685	0.750	0.923	0.896

AE: Arterial enhancement; AUC: Area under the receiver operating characteristic curve; CI: Confidence interval; CL: Clinical data; NPV: Negative predict value; PE: Portal enhancement; PPV: Positive predict value; US: Ultrasound.

demonstrated greater benefits.

DISCUSSION

In this study, we constructed a new radiomics model to differentiate between ICC and HCC using CEUS, achieving good diagnostic performance. The final radiomics model incorporated 21 features and demonstrated higher efficacy than experienced radiologists.

ICC is the second most common primary hepatic malignancy, following HCC. The incidence of these two malignant hepatic tumors, in parallel with their mortality, has markedly increased worldwide in recent years[9,10]. Given their distinct pathogenesis, pathological features, prognostic outcomes, and responses to adjuvant therapies, accurate discrimination between HCC and ICC is paramount for effective clinical management[11].

While pathology remains the gold standard diagnostic test for liver cancer, often requiring paracentesis or surgery, its invasive nature and associated risks, such as bleeding and tumor cell seeding, render it a less favorable option. Hence, image diagnosis occupies a pivotal role in this realm, with US serving as the primary modality for liver disease surveillance.

In recent years, CEUS has played a significant role in characterizing focal liver lesions, including the differentiation of ICC from HCC. Compared to computed tomography (CT) and MRI, CEUS is a real-time dynamic imaging modality that provides enhanced information on the blood supply of lesions, which is crucial for liver tumor discrimination. CEUS is completely radiation-free for patients. Several studies have reported that CEUS has an excellent diagnostic performance in distinguishing between ICC and HCC. However, the scanning technique and visual interpretation of US images are both operator dependent, and diagnostic accuracy varies significantly across different radiologists and CEUS centers. Therefore, developing a more reliable, efficient, and user-friendly method for differentiation is imperative.

ACKNOWLEDGEMENTS

The authors thank Yan Li for supporting this study.

FOOTNOTES

Author contributions: Su LY, Xie XY, and Lin MX designed the research study; Su LY, Lin MX, Xu M, and Chen YL performed the research; Su LY and Chen YL analyzed the data and wrote the manuscript; Chen YL contributed to the model construction. All authors have read and approved the final manuscript.

Supported by National Natural Science Foundation of China, No. 92059201.

Institutional review board statement: This study was reviewed and approved by the Ethics Committee of the First Affiliated Hospital of Sun Yat-Sen University.

Informed consent statement: Informed consent was waived for this research because of the retrospective design of the study.

Conflict-of-interest statement: We have no financial relationships to disclose.

Data sharing statement: No additional data are available.

Open-Access: This article is an open-access article that was selected by an in-house editor and fully peer-reviewed by external reviewers. It is distributed in accordance with the Creative Commons Attribution NonCommercial (CC BY-NC 4.0) license, which permits others to distribute, remix, adapt, build upon this work non-commercially, and license their derivative works on different terms, provided the original work is properly cited and the use is non-commercial. See: <https://creativecommons.org/licenses/by-nc/4.0/>

Country of origin: China

ORCID number: Li-Ya Su 0000-0002-7771-893X; Man-Xia Lin 0000-0002-2969-0020; Xiao-Yan Xie 0000-0002-9761-9525.

S-Editor: Fan JR

L-Editor: Filipodia

P-Editor: Zhang L

REFERENCES

- 1 **Sung H**, Ferlay J, Siegel RL, Laversanne M, Soerjomataram I, Jemal A, Bray F. Global Cancer Statistics 2020: GLOBOCAN Estimates of Incidence and Mortality Worldwide for 36 Cancers in 185 Countries. *CA Cancer J Clin* 2021; **71**: 209-249 [PMID: 33538338 DOI: 10.3322/caac.21660]
- 2 **Sia D**, Villanueva A, Friedman SL, Llovet JM. Liver Cancer Cell of Origin, Molecular Class, and Effects on Patient Prognosis. *Gastroenterology* 2017; **152**: 745-761 [PMID: 28043904 DOI: 10.1053/j.gastro.2016.11.048]
- 3 **Gordan JD**, Kennedy EB, Abou-Alfa GK, Beg MS, Brower ST, Gade TP, Goff L, Gupta S, Guy J, Harris WP, Iyer R, Jaiyesimi I, Jhawer M, Karippot A, Kaseb AO, Kelley RK, Knox JJ, Kortmansky J, Leaf A, Remak WM, Shroff RT, Sohal DPS, Taddei TH, Venepalli NK, Wilson A, Zhu AX, Rose MG. Systemic Therapy for Advanced Hepatocellular Carcinoma: ASCO Guideline. *J Clin Oncol* 2020; **38**: 4317-4345 [PMID: 33197225 DOI: 10.1200/JCO.20.02672]
- 4 **European Association for the Study of the Liver**. EASL-ILCA Clinical Practice Guidelines on the management of intrahepatic cholangiocarcinoma. *J Hepatol* 2023; **79**: 181-208 [PMID: 37084797 DOI: 10.1016/j.jhep.2023.03.010]
- 5 **Liu GJ**, Wang W, Lu MD, Xie XY, Xu HX, Xu ZF, Chen LD, Wang Z, Liang JY, Huang Y, Li W, Liu JY. Contrast-Enhanced Ultrasound for the Characterization of Hepatocellular Carcinoma and Intrahepatic Cholangiocarcinoma. *Liver Cancer* 2015; **4**: 241-252 [PMID: 26779444 DOI: 10.1159/000367738]
- 6 **European Association for the Study of the Liver**. EASL Clinical Practice Guidelines: Management of hepatocellular carcinoma. *J Hepatol* 2018; **69**: 182-236 [PMID: 29628281 DOI: 10.1016/j.jhep.2018.03.019]
- 7 **Aerts HJ**. The Potential of Radiomic-Based Phenotyping in Precision Medicine: A Review. *JAMA Oncol* 2016; **2**: 1636-1642 [PMID: 27541161 DOI: 10.1001/jamaoncol.2016.2631]
- 8 **Lewis S**, Peti S, Hectors SJ, King M, Rosen A, Kamath A, Putra J, Thung S, Taouli B. Volumetric quantitative histogram analysis using diffusion-weighted magnetic resonance imaging to differentiate HCC from other primary liver cancers. *Abdom Radiol (NY)* 2019; **44**: 912-922 [PMID: 30712136 DOI: 10.1007/s00261-019-01906-7]
- 9 **Bertuccio P**, Malvezzi M, Carioli G, Hashim D, Boffetta P, El-Serag HB, La Vecchia C, Negri E. Global trends in mortality from intrahepatic and extrahepatic cholangiocarcinoma. *J Hepatol* 2019; **71**: 104-114 [PMID: 30910538 DOI: 10.1016/j.jhep.2019.03.013]
- 10 **Kim SJ**, Lee JM, Han JK, Kim KH, Lee JY, Choi BI. Peripheral mass-forming cholangiocarcinoma in cirrhotic liver. *AJR Am J Roentgenol* 2007; **189**: 1428-1434 [PMID: 18029881 DOI: 10.2214/AJR.07.2484]
- 11 **You MW**, Yun SJ. Differentiating between hepatocellular carcinoma and intrahepatic cholangiocarcinoma using contrast-enhanced MRI features: a systematic review and meta-analysis. *Clin Radiol* 2019; **74**: 406.e9-406.e18 [PMID: 30704667 DOI: 10.1016/j.crad.2018.12.016]
- 12 **Scapicchio C**, Gabelloni M, Barucci A, Cioni D, Saba L, Neri E. A deep look into radiomics. *Radiol Med* 2021; **126**: 1296-1311 [PMID: 34213702 DOI: 10.1007/s11547-021-01389-x]

- 13 **Li R**, Yuan MX, Ma KS, Li XW, Tang CL, Zhang XH, Guo DY, Yan XC. Detailed analysis of temporal features on contrast enhanced ultrasound may help differentiate intrahepatic cholangiocarcinoma from hepatocellular carcinoma in cirrhosis. *PLoS One* 2014; **9**: e98612 [PMID: 24874413 DOI: 10.1371/journal.pone.0098612]
- 14 **Galassi M**, Iavarone M, Rossi S, Bota S, Vavassori S, Rosa L, Leoni S, Venerandi L, Marinelli S, Sangiovanni A, Veronese L, Fraquelli M, Granito A, Golfieri R, Colombo M, Bolondi L, Piscaglia F. Patterns of appearance and risk of misdiagnosis of intrahepatic cholangiocarcinoma in cirrhosis at contrast enhanced ultrasound. *Liver Int* 2013; **33**: 771-779 [PMID: 23445369 DOI: 10.1111/liv.12124]
- 15 **Barreiros AP**, Piscaglia F, Dietrich CF. Contrast enhanced ultrasound for the diagnosis of hepatocellular carcinoma (HCC): comments on AASLD guidelines. *J Hepatol* 2012; **57**: 930-932 [PMID: 22739095 DOI: 10.1016/j.jhep.2012.04.018]
- 16 **Jang JY**, Kim MY, Jeong SW, Kim TY, Kim SU, Lee SH, Suk KT, Park SY, Woo HY, Kim SG, Heo J, Baik SK, Kim HS, Tak WY. Current consensus and guidelines of contrast enhanced ultrasound for the characterization of focal liver lesions. *Clin Mol Hepatol* 2013; **19**: 1-16 [PMID: 23593604 DOI: 10.3350/cmh.2013.19.1.1]

Retrospective Study

Correlation between dose-volume parameters and rectal bleeding after 12 fractions of carbon ion radiotherapy for prostate cancer

Takashi Ono, Hiraku Sato, Yuya Miyasaka, Yasuhito Hagiwara, Natsuko Yano, Hiroko Akamatsu, Mayumi Harada, Mayumi Ichikawa

Specialty type: Radiology, nuclear medicine and medical imaging

Provenance and peer review: Invited article; Externally peer reviewed.

Peer-review model: Single blind

Peer-review report's classification

Scientific Quality: Grade C

Novelty: Grade B

Creativity or Innovation: Grade B

Scientific Significance: Grade B

P-Reviewer: Huang X

Received: May 21, 2024

Revised: July 8, 2024

Accepted: July 10, 2024

Published online: July 28, 2024

Processing time: 63 Days and 21.5 Hours



Takashi Ono, Hiraku Sato, Yasuhito Hagiwara, Natsuko Yano, Hiroko Akamatsu, Mayumi Harada, Mayumi Ichikawa, Department of Radiation Oncology, Faculty of Medicine, Yamagata University, Yamagata 990-9585, Japan

Yuya Miyasaka, Department of Heavy Particle Medical Science, Yamagata University Graduate School of Medical Science, Yamagata 990-9585, Japan

Corresponding author: Takashi Ono, MD, PhD, Doctor, Department of Radiation Oncology, Faculty of Medicine, Yamagata University, 2-2-2 Iida-Nishi, Yamagata 990-9585, Japan. abc1123513@gmail.com

Abstract

BACKGROUND

Carbon ion radiotherapy (CIRT) is currently used to treat prostate cancer. Rectal bleeding is a major cause of toxicity even with CIRT. However, to date, a correlation between the dose and volume parameters of the 12 fractions of CIRT for prostate cancer and rectal bleeding has not been shown. Similarly, the clinical risk factors for rectal bleeding were absent after 12 fractions of CIRT.

AIM

To identify the risk factors for rectal bleeding in 12 fractions of CIRT for prostate cancer.

METHODS

Among 259 patients who received 51.6 Gy [relative biological effectiveness (RBE)], in 12 fractions of CIRT, 15 had grade 1 (5.8%) and nine had grade 2 rectal bleeding (3.5%). The dose-volume parameters included the volume (cc) of the rectum irradiated with at least x Gy (RBE) (Vx) and the minimum dose in the most irradiated x cc normal rectal volume (Dx).

RESULTS

The mean values of D6cc, D2cc, V10 Gy (RBE), V20 Gy (RBE), V30 Gy (RBE), and V40 Gy (RBE) were significantly higher in the patients with rectal bleeding than in those without. The cutoff values were D6cc = 34.34 Gy (RBE), D2cc = 46.46 Gy (RBE), V10 Gy (RBE) = 9.85 cc, V20 Gy (RBE) = 7.00 cc, V30 Gy (RBE) = 6.91 cc, and V40 Gy (RBE) = 4.26 cc. The D2cc, V10 Gy (RBE), and V20 Gy (RBE) cutoff values were significant predictors of grade 2 rectal bleeding.

CONCLUSION

The above dose-volume parameters may serve as guidelines for preventing rectal bleeding after 12 fractions of CIRT for prostate cancer.

Key Words: Carbon ion radiotherapy; Prostate cancer; Rectal bleeding; Dose volume parameters; Prevention

©The Author(s) 2024. Published by Baishideng Publishing Group Inc. All rights reserved.

Core Tip: This study identified the risk factors for rectal bleeding, including dose-volume parameters of 51.6 Gy [relative biological effectiveness (RBE)] in 12 fractions of carbon ion radiotherapy (CIRT) for prostate cancer. The cutoff values of D2cc = 46.46 Gy (RBE), V10 Gy (RBE) = 9.85 cc, and V20 Gy (RBE) = 7.00 cc were significant factors for the occurrence rate of grade 2 rectal bleeding. When planning CIRT for prostate cancer, the rate of rectal bleeding may decrease if these values are used.

Citation: Ono T, Sato H, Miyasaka Y, Hagiwara Y, Yano N, Akamatsu H, Harada M, Ichikawa M. Correlation between dose-volume parameters and rectal bleeding after 12 fractions of carbon ion radiotherapy for prostate cancer. *World J Radiol* 2024; 16(7): 256-264

URL: <https://www.wjgnet.com/1949-8470/full/v16/i7/256.htm>

DOI: <https://dx.doi.org/10.4329/wjr.v16.i7.256>

INTRODUCTION

Prostate cancer is the second most frequent cancer, with an estimated 1.4 million new cases, and is the most frequent cancer in 112 of 185 countries, including Japan. Although mortality rates have decreased in most high-income countries since the 1990s, they are expected to remain the fifth-leading cause of cancer-related deaths among men worldwide by 2020[1]. One well-established risk factor is older age[1,2]; therefore, the incidence of prostate cancer is expected to increase owing to Japan's aging society. Some patients with low-risk prostate cancer are allowed active surveillance to reduce overtreatment, and watchful waiting may be an option for frail patients. However, radical treatment should be considered for patients with medium- or high-risk prostate cancer and physicians should not refuse treatment based solely on age[2,3].

There are two radical treatments for prostate cancer: Radical prostatectomy and radiotherapy with or without androgen deprivation therapy (ADT)[2,3]. Retrospective studies have reported conflicting results regarding the superiority of radical prostatectomy or high-dose external X-ray radiotherapy, including biochemical failure[4-7]. Moreover, few randomized controlled trials have directly compared these two radical treatments[3]. Therefore, patients with good performance status can choose each treatment, considering their toxicities and advantages. However, many patients living in aging societies are unsuitable for surgery because of factors such as older age and comorbidities. Radiotherapy may be indicated in these cases. Moreover, radiotherapy avoids the substantial stress caused by urinary incontinence resulting from radical prostatectomy[3].

Rectal bleeding is one of the most troublesome toxicities in high-dose radiotherapy, and previous studies have shown a 1.8%-13% occurrence rate of grade 2 or higher rectal bleeding[8-11]. Previous studies have also shown a correlation between rectal dose-volume parameters and occurrence rate[10,12-17]. Therefore, intensity-modulated radiotherapy, which can reduce the exposure dose for at-risk organs, including the rectum, has been reported to reduce the risk of gastrointestinal toxicities, including rectal bleeding, compared with three-dimensional radiotherapy[11]. As an alternative, hydrogel spacers have been used in some trials to reduce rectal bleeding by escalating prescription doses[18, 19]. However, some reports have suggested clinical risk factors for grade 2 or higher rectal bleeding, such as diabetes mellitus (DM), anticoagulation therapy, ADT, and previous surgery[9,15,20-22].

Carbon ion radiotherapy (CIRT) is currently used to treat prostate cancer. In 2018, CIRT was approved by the national insurance as a curative treatment option for localized prostate cancer in Japan[23]. Multiple clinical trials have led to the development of novel therapies. The first clinical trial was a dose-escalation trial from 54 Gy [relative biological effectiveness (RBE)] in 20 fractions to 72 Gy (RBE) in 20 fractions conducted in December 1997 using the Heavy Ion Medical Accelerator in Chiba at the National Institute of Radiological Sciences[24]. Thereafter, treatment fractionations were gradually decreased from 20-16 to 12 fractions, and 51.6 Gy (RBE) in 12 fractions was used for curative CIRT for prostate cancer in Japan[25,26]. Favorable long-term results have been obtained using this schedule, including data for elderly patients[26,27].

Rectal bleeding is a major cause of toxicity even with CIRT. The incidence rates of grade 1 and 2 rectal bleeding are 1.8%-13% and 0%-2%, respectively[26-29]. There have been reports on the correlation between dose-volume parameters of 20 fractions of CIRT for prostate cancer and rectal bleeding[28]. Other reports have presented estimation data using normal tissue complication probability parameters[30,31]. However, to date, no correlation has been shown between the dose and volume parameters of the 12 fractions of CIRT for prostate cancer and rectal bleeding. Similarly, the clinical risk factors for rectal bleeding were absent after 12 fractions of CIRT. This study aimed to determine the correlation between the dose and volume parameters of 12 fractions of CIRT for prostate cancer and rectal bleeding.

MATERIALS AND METHODS

Ethics statement

This study was approved by the Institutional Ethics Committee of the Faculty of Medicine of Yamagata University (approval number: 2023-51). The study was conducted in accordance with the principles of the Declaration of Helsinki.

Patients

Patients who underwent CIRT for prostate cancer between February 2021 and December 2021 at Yamagata University Hospital were retrospectively identified and analyzed. The prostate cancer stage was determined according to the Union for International Cancer Control (8th edition) using rectal examination, magnetic resonance imaging, computed tomography (CT), and bone scintigraphy. The inclusion criteria were as follows: Received 51.6 Gy (RBE) in 12 fractions at the East Japan Heavy Ion Center; no rectal invasion; no lymph node metastasis; and no distant metastasis to other organs or sites of uncontrolled cancer.

CIRT

For planning, CT images of the patients were acquired using an Aquilion One (Canon Medical Systems, Otawara, Japan) with a slice thickness of 2 mm. All patients were immobilized in the supine position using a HipFix thermoplastic solid and HipFix Baseplate (CIVCO, IA, United States). In cases where there was large air/fecal content, we performed gas removal or enemas and adjusted the laxatives. For cases that were considered hopeless, retreatment planning CT was performed after adjusting the prescription. Therefore, no patients were excluded from this study because of excessive air/fecal content. The clinical target volume (CTV) included the prostate volume, with reference to magnetic resonance imaging. In addition to the prostate, a part of the seminal vesicle was added for T3a or lower, excluding low-risk cases (\leq T2a, Gleason score was 3 + 3, and initial prostate-specific antigen \leq 10 ng/mL), and the entire seminal vesicle was included in the CTV for T3b. The CIRT dose calculation algorithm uses a pencil beam. The planning target volume (PTV) was defined as the CTV plus 5-mm margins in the cranial, caudal, and posterior directions and 10-mm margins in the lateral and anterior directions. The CIRT plan was created using RayStation10A (RaySearch Laboratories, Stockholm, Sweden). A microdosimetric kinetic model was used to calculate the RBE dose[32,33]. The CIRT plan was created with the goal of > 51.55 Gy (RBE) for 95% of the PTV, accounting for the condition of each case and the rectal dose by each physician. CIRT was performed using a CI-1000 (Toshiba Energy Systems & Solutions Corporation, Kanagawa, Japan). The CIRT schedule was 51.6 Gy (RBE) in 12 fractions. Generally, CIRT is performed for 4 days in a week (generally Tuesday to Friday) and 6 days in 2 weeks if there are consecutive holidays, such as national holidays. The treatment plan was performed using 90- and 270-degree beams in six fractions each. Daily X-ray imaging and digitally reconstructed radiographs were used for positioning.

Evaluation and follow-up

Patients were followed-up every 2-6 months in the first year and every 6-12 months thereafter. Rectal bleeding was evaluated using the rectal hemorrhage item within the Common Terminology Criteria for Adverse Events version 5.0.

Statistical analysis

Statistical analyses were performed using the IBM SPSS Statistics software (version 24; SPSS Inc., Chicago, IL, United States). The Kaplan–Meier algorithm was used to estimate the cumulative incidence of rectal bleeding from the start of CIRT to the occurrence of rectal bleeding or last follow-up. The mean values of the dose-volume parameters were compared using the Mann-Whitney *U* test. Pretreatment clinical factors included DM, anticoagulation therapy, and ADT. Previous surgeries were not included in this study because not all patients had a sufficient surgical history. The entire rectal area was evaluated. The dose-volume parameters included the volume (cc) of the rectum irradiated with at least x Gy (RBE) (V_x) (V_{10-50} Gy [RBE]) and the minimum dose in the most irradiated x cc normal rectal volume (D_x) (D_{6cc} , D_{2cc} , and $D_{0.2cc}$). The relationship between the occurrence of rectal bleeding and pretreatment factors was compared using the χ^2 test. Receiver operating characteristic (ROC) curves and sensitivity and specificity calculations were performed to determine the cutoff value of the significant dose-volume parameter with the highest sum of sensitivity and specificity. The χ^2 test was used for evaluation. All *P*-values were two-sided, and *P*-values < 0.05 were considered statistically significant.

RESULTS

Patients

In total, 259 patients received 51.6 Gy (RBE) in 12 fractions of CIRT for prostate cancer, including two patients with bladder invasion (Table 1). All patients completed the planned treatment. The median follow-up time was 31 months (range, 14-40 months), and $> 94\%$ of living patients were followed up for at least 24 months. Five patients died of unrelated illnesses between 14 and 24 months after CIRT (two with heart disease, one with bacterial pneumonia, and two with pancreatic cancer).

Table 1 Patient characteristics, n (%)

Characteristics (n = 259)	
Age (years)	
Median (range)	71 (54-87)
Karnofsky performance status	
100	232 (89.5)
90	24 (9.3)
80	1 (0.4)
60	2 (0.8)
Follow-up time (months)	
Median (range)	31 (14-40)
Initial prostate-specific antigen (ng/mL)	
Median (range)	8.23 (0.62-1354)
T category	
1b	1 (0.4)
1c	39 (15.1)
2a	99 (38.2)
2b	34 (13.0)
2c	57 (22.0)
3a	19 (7.3)
3b	8 (3.1)
4	2 (0.8)
Gleason score	
6	39 (15.1)
7	119 (45.9)
8	65 (25.1)
9	35 (13.5)
10	1 (0.4)
Diabetes mellitus	
Yes	29 (11.2)
No	230 (88.8)
Anticoagulation therapy	
Yes	38 (14.7)
No	221 (85.3)
Androgen deprivation therapy	
Yes	234 (90.3)
No	25 (9.7)
Planning target volume (cc)	
Median (range)	80.71 (43.24-202.60)

Rectal bleeding

Fifteen patients had grade 1 rectal bleeding (5.8%), and nine patients had grade 2 rectal bleeding (3.5%). **Figure 1** shows the cumulative incidence. The median time between CIRT and rectal bleeding was 8 months (1-19 months). Approximately three-quarters of the patients developed rectal bleeding within 12 months, excluding six of the 24 patients. Only two patients had grade 1 rectal bleeding after 18 months. Eight of the nine patients experienced grade 2 rectal bleeding,

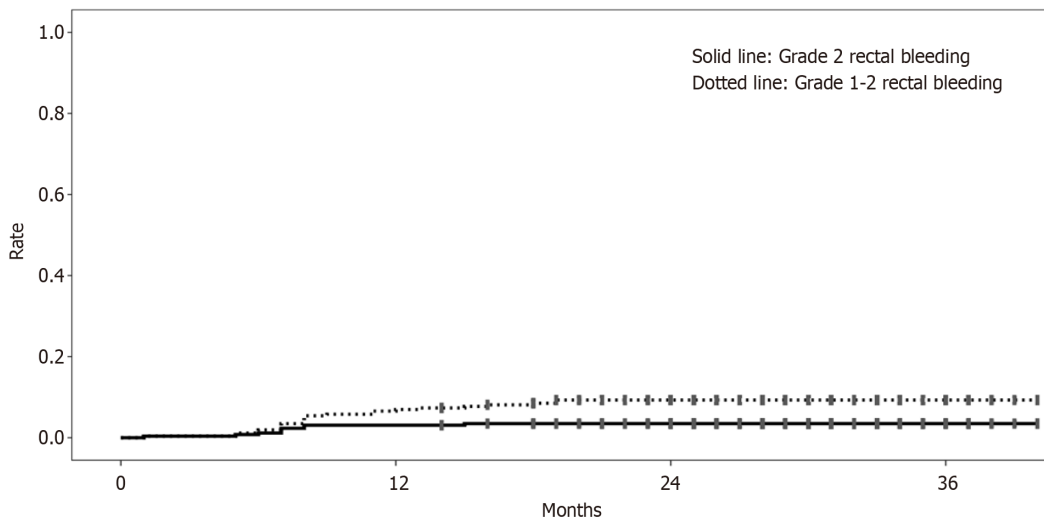


Figure 1 The cumulative incidence of rectal bleeding after carbon ion radiotherapy.

all eight of whom experienced bleeding within 8 months post-CIRT.

Correlation between pretreatment clinical factors and rectal bleeding

Grade 1 or 2 rectal bleeding occurred in four of 29 patients (14%) with DM, five of 38 patients (13%) using anticoagulation therapy, and four of 25 patients (16%) who received concomitant ADT. There were no significant differences in rectal bleeding in any of the pretreatment clinical factors.

Correlation between dose-volume parameter and rectal bleeding

Regarding dose-volume parameters, the mean values of D6cc, D2cc, V10 Gy (RBE), V20 Gy (RBE), V30 Gy (RBE), and V40 Gy (RBE) in patients with grade 1 or 2 rectal bleeding were significantly higher than in those without (Table 2). The data were used for the ROC curves. The cutoff values of parameters were D6cc = 34.34 Gy (RBE) (sensitivity 50.0%, specificity 85.5%), D2cc = 46.46 Gy (RBE) (sensitivity 54.2%, specificity 77.9%), V10 Gy (RBE) = 9.85 cc (sensitivity 79.2%, specificity 50.2%), V20 Gy (RBE) = 7.00 cc (sensitivity 83.3%, specificity 49.4%), V30 Gy (RBE) = 6.91 cc (sensitivity 50.0%, specificity 84.7%), and V40 Gy (RBE) = 4.26 cc (sensitivity 58.3%, specificity 80.9%), respectively, by using ROC curves. Analysis of the correlations between these cutoff values and the occurrence rates of grade 2 rectal bleeding showed that parameters below the cutoff values of D2cc, V10 Gy (RBE), and V20 Gy (RBE) were significant factors for lower occurrence rates (Table 3).

DISCUSSION

To the best of our knowledge, this is the first report showing a correlation between dose-volume parameters and rectal bleeding after 51.6 Gy (RBE) in 12 fractions of CIRT for prostate cancer.

The cutoff value of rectal bleeding after CIRT for prostate cancer should be defined using clinical data, completely separate from reports on X-ray therapy, although dose-volume parameters appear to be related to rectal bleeding in CIRT, as with X-ray therapy. This is because carbon ions do not have the characteristics of photons. Carbon ions have a higher RBE and a lower oxygen enhancement ratio[34]. Owing to this advancement, CIRT is expected to achieve eradication of radioresistant tumors and a smaller variation in radiation sensitivity with the position of the cells in the replication cycle, unlike X-ray therapy. Although this property may have positive therapeutic effects, it may also affect toxicity. Moreover, the physical dose (Gy) decreases as the RBE increases to achieve a uniform dose [Gy (RBE)] across the irradiated field in CIRT[35]. As mentioned above, CIRT often has different properties from those of X-ray therapy, which has been widely used until now, and it is unclear whether the common sense that physicians use for X-ray therapy still applies. In addition, the areas of the rectum irradiated with low and medium doses of X-ray radiotherapy are much wider than those irradiated with CIRT[36]. This is because CIRT is applied mainly in the left and right directions, including the plan of the present study[26,28,36]. These differences may result in different outcomes for each treatment method. Therefore, a concrete discussion is needed using actual clinical results, as in the present study.

Methods using absolute and relative values have been reported for evaluating rectal doses. Most studies have discussed the proportion of the rectum or rectal wall irradiated with doses of V40-70 Gy[10,12-16]. However, this evaluation method varies greatly depending on the rectal area and degree of rectal dilatation. In contrast, Kotabe *et al*[17] reported that the absolute rectal volume irradiated at 60 Gy was the only significant factor for rectal bleeding, although relative rectal volume was not. The present study also analyzed the absolute volume owing to rectal volume uncertainty, as reported by Kotabe *et al*[17]. Indeed, the present study found a significant difference between the absolute rectal volume and occurrence rate of rectal bleeding, and it seems appropriate to evaluate it using absolute values, even for

Table 2 The correlation between dose–volume parameter of rectum and rectal bleeding, mean \pm SD

	Grade 0	Grade 1/2	P value
D 6cc	25.40 \pm 7.56 Gy (RBE)	30.93 \pm 6.75 Gy (RBE)	0.001 ^a
D 2cc	44.54 \pm 2.88 Gy (RBE)	45.93 \pm 1.71 Gy (RBE)	0.005 ^a
D 0.2cc	49.73 \pm 0.98 Gy (RBE)	49.80 \pm 0.34 Gy (RBE)	0.592
V 10 Gy (RBE)	10.45 \pm 2.72 cc	11.89 \pm 2.79 cc	0.010 ^a
V 20 Gy (RBE)	7.46 \pm 2.05 cc	8.90 \pm 2.29 cc	0.002 ^a
V 30 Gy (RBE)	5.32 \pm 1.57 cc	6.56 \pm 1.78 cc	0.001 ^a
V 40 Gy (RBE)	3.34 \pm 1.05 cc	4.15 \pm 1.12 cc	0.001 ^a
V 50 Gy (RBE)	0.18 \pm 0.10 cc	0.17 \pm 0.12 cc	0.590

^aP < 0.05.

RBE: Relative biological effectiveness.

Table 3 The comparison of ratio of rectal bleeding before and after cutoff values of dose-volume parameters calculated by using receiver operating characteristic curves

	Comparison	Number of patients	Ratio of grade 2 rectal bleeding (%)	P value
D 6cc	\geq 34.34 Gy (RBE)	54	5.3	0.42
	< 34.34 Gy (RBE)	202	3.0	
D 2cc	\geq 46.46 Gy (RBE)	65	7.7	0.047 ^a
	< 46.46 Gy (RBE)	194	2.1	
V 10 Gy (RBE)	\geq 9.85 cc	136	5.9	0.038 ^a
	< 9.85 cc	123	0.8	
V 20 Gy (RBE)	\geq 7.00 cc	139	5.8	0.040 ^a
	< 7.00 cc	120	0.8	
V 30 Gy (RBE)	\geq 6.91 cc	48	6.0	0.374
	< 6.91 cc	211	6.3	
V 40 Gy (RBE)	\geq 4.26 cc	59	1.7	0.689
	< 4.26 cc	200	4.0	

^aP < 0.05.

RBE: Relative biological effectiveness.

CIRT. Moreover, there is a report on CIRT for cervical cancer rather than prostate cancer, which was evaluated based on the absolute values of V_x and D_{xcc}. In this study, these were identified as significant factors for rectal bleeding[37], which is consistent with the results of the present study.

There have been some reports of rectal bleeding with CIRT using clinical data from a certain number of patients. Using clinical data from 172 patients, Ishikawa *et al*[28] reported that the V50% of the prescribed dose (33 Gy [RBE]) was a significant factor for rectal bleeding. In contrast, factors other than a high rectal dose were identified as significant in the present study. The reason may be the difference in the evaluation methods, such as the absolute value in the present study, unlike the relative value in the previous study, and the difference in the dose per fraction. However, Okonogi *et al* [37] reported that D5cc and D2cc for the rectum were significantly higher in patients with \geq grade 1 rectal bleeding, although the V10-50 were not, using 139 patients' clinical data. In the present study, D6cc and D2cc were significant risk factors for rectal bleeding, as in their study. The different results of the V_x data may be due to differences in the irradiation method, as CIRT was applied only from the left and right directions in the present study; however, CIRT may also be applied in other directions for cervical cancer, as well as differences in total dose and dose per fraction. Beams from other sides likely worsen the absolute exposure to radiation of the rectal wall compared with a more dispersed beam, given an equal rectal volume, including its contents (gas and feces). Previous evaluations of X-ray therapy have shown that an area irradiated with a slightly higher dose affects rectal bleeding, unlike the present results, for example, V50-70[10,12-16]. In this study, the area of the rectum irradiated with low-dose radiation was identified as a significant

factor in the incidence of rectal bleeding. Moreover, no significant difference was observed in the pinpoint high-dose areas as D0.2cc in the present study. The tendency of the significant factor to be the area of the rectum irradiated with a low dose was more clearly observed in patients with grade 2 rectal bleeding. This may be because a small dose must be delivered to a certain area of the rectum for rectal bleeding, especially problematic bleeding.

DM, anticoagulation therapy, and ADT, the clinical factors examined in the present study, have been suggested as risk factors for rectal bleeding after X-ray therapy for prostate cancer[9,15,20,21,28]. Herold *et al*[20] reported that DM is a significant risk factor for grade 2 gastrointestinal toxicity. However, Feigenberg *et al*[21] reported that ADT was an independent predictor of \geq grade 2 gastrointestinal toxicity, adding to the total dose. Ishikawa *et al*[28] reported that anticoagulation therapy was a significant risk factor for grade 1-2 rectal bleeding after 20 fractions of CIRT. However, these factors were not significant predictors of rectal bleeding in the present study. This may be because only a small number of patients received DM or anticoagulation therapy, whereas most patients in the present study received ADT. Other reasons may include cases in which the attending physician adjusted the dose to the rectum, taking into account risk factors; however, this could not be evaluated in this retrospective study.

This study had two limitations. First, the follow-up period was relatively short. However, more than 94% of patients were followed for at least 2 years. Moreover, Ishikawa *et al*[28] reported that $> 80\%$ of rectal bleeding cases occurred within 2 years, and most patients with rectal bleeding in the present study experienced it within 1.5 years. Second, this study was based on retrospective data from a single institution. However, the number of patients in the present study was larger than those in previous clinical studies that examined dose-volume parameters[28,36]. Therefore, despite its limitations, the present study is meaningful.

CONCLUSION

In conclusion, D2cc = 46.46 Gy (RBE), V10 Gy (RBE) = 9.85 cc, and V20 Gy (RBE) = 7.00 cc may be indicators for preventing both all-grade and grade 2 rectal bleeding after 51.6 Gy (RBE) in 12 fractions of CIRT for prostate cancer.

ACKNOWLEDGEMENTS

The authors thanked to all staff of carbon-ion radiotherapy section.

FOOTNOTES

Author contributions: Ono T designed and performed the research and wrote present paper; Sato H designed and supervised the report; Miyasaka Y provided clinical advice; Hagiwara Y, Yano N, Akamatsu H, Harada M, and Ichikawa M contributed to data analysis.

Institutional review board statement: This study was reviewed and approved by the Ethics Committee of the Faculty of Medicine at Yamagata University (approval number: 2023-51).

Informed consent statement: Patients were not required to give informed consent to the study because the analysis used anonymous clinical data that were obtained after each patient agreed to treatment by written informed consent. When consenting to treatment, we also informed patients of the possibility of their use in research, and they agreed to this, so we do not believe it is necessary to obtain new consent for this study. For full disclosure, the details of the study are published on the home page of Faculty of Medicine at Yamagata University.

Conflict-of-interest statement: All authors report no relevant conflicts of interest for this article.

Data sharing statement: Data sharing is not applicable to this article.

Open-Access: This article is an open-access article that was selected by an in-house editor and fully peer-reviewed by external reviewers. It is distributed in accordance with the Creative Commons Attribution NonCommercial (CC BY-NC 4.0) license, which permits others to distribute, remix, adapt, build upon this work non-commercially, and license their derivative works on different terms, provided the original work is properly cited and the use is non-commercial. See: <https://creativecommons.org/licenses/by-nc/4.0/>

Country of origin: Japan

ORCID number: Takashi Ono 0000-0002-9711-1158; Hiraku Sato 0000-0002-0210-3439; Yasuhito Hagiwara 0000-0002-5612-5094; Natsuko Yano 0000-0002-2911-8489; Hiroko Akamatsu 0000-0001-8086-8974; Mayumi Ichikawa 0000-0001-8092-3371.

S-Editor: Qu XL

L-Editor: A

P-Editor: Che XX

REFERENCES

- 1 **Sung H**, Ferlay J, Siegel RL, Laversanne M, Soerjomataram I, Jemal A, Bray F. Global Cancer Statistics 2020: GLOBOCAN Estimates of Incidence and Mortality Worldwide for 36 Cancers in 185 Countries. *CA Cancer J Clin* 2021; **71**: 209-249 [PMID: 33538338 DOI: 10.3322/caac.21660]
- 2 **Mottet N**, van den Bergh RCN, Briers E, Van den Broeck T, Cumberbatch MG, De Santis M, Fanti S, Fossati N, Gandaglia G, Gillessen S, Grivas N, Grummet J, Henry AM, van der Kwast TH, Lam TB, Lardas M, Liew M, Mason MD, Moris L, Oprea-Lager DE, van der Poel HG, Rouvière O, Schoots IG, Tilki D, Wiegel T, Willemse PM, Cornford P. EAU-EANM-ESTRO-ESUR-SIOG Guidelines on Prostate Cancer-2020 Update. Part 1: Screening, Diagnosis, and Local Treatment with Curative Intent. *Eur Urol* 2021; **79**: 243-262 [PMID: 33172724 DOI: 10.1016/j.eururo.2020.09.042]
- 3 **Sandhu S**, Moore CM, Chiong E, Beltran H, Bristow RG, Williams SG. Prostate cancer. *Lancet* 2021; **398**: 1075-1090 [PMID: 34370973 DOI: 10.1016/S0140-6736(21)00950-8]
- 4 **Kupelian PA**, Potters L, Khuntia D, Ciezki JP, Reddy CA, Reuther AM, Carlson TP, Klein EA. Radical prostatectomy, external beam radiotherapy <72 Gy, external beam radiotherapy > or =72 Gy, permanent seed implantation, or combined seeds/external beam radiotherapy for stage T1-T2 prostate cancer. *Int J Radiat Oncol Biol Phys* 2004; **58**: 25-33 [PMID: 14697417 DOI: 10.1016/s0360-3016(03)00784-3]
- 5 **Reichard CA**, Hoffman KE, Tang C, Williams SB, Allen PK, Achim MF, Kuban DA, Chapin BF. Radical prostatectomy or radiotherapy for high- and very high-risk prostate cancer: a multidisciplinary prostate cancer clinic experience of patients eligible for either treatment. *BJU Int* 2019; **124**: 811-819 [PMID: 31009137 DOI: 10.1111/bju.14780]
- 6 **Shih HJ**, Chang SC, Hsu CH, Lin YC, Hung CH, Wu SY. Comparison of Clinical Outcomes of Radical Prostatectomy versus IMRT with Long-Term Hormone Therapy for Relatively Young Patients with High- to Very High-Risk Localized Prostate Cancer. *Cancers (Basel)* 2021; **13** [PMID: 34885096 DOI: 10.3390/cancers13235986]
- 7 **Wu SY**, Chang SC, Chen CI, Huang CC. Oncologic Outcomes of Radical Prostatectomy and High-Dose Intensity-Modulated Radiotherapy with Androgen-Deprivation Therapy for Relatively Young Patients with Unfavorable Intermediate-Risk Prostate Adenocarcinoma. *Cancers (Basel)* 2021; **13** [PMID: 33806181 DOI: 10.3390/cancers13071517]
- 8 **Zelevsky MJ**, Chan H, Hunt M, Yamada Y, Shippy AM, Amols H. Long-term outcome of high dose intensity modulated radiation therapy for patients with clinically localized prostate cancer. *J Urol* 2006; **176**: 1415-1419 [PMID: 16952647 DOI: 10.1016/j.juro.2006.06.002]
- 9 **Skwarchuk MW**, Jackson A, Zelevsky MJ, Venkatraman ES, Cowen DM, Levegrün S, Burman CM, Fuks Z, Leibel SA, Ling CC. Late rectal toxicity after conformal radiotherapy of prostate cancer (I): multivariate analysis and dose-response. *Int J Radiat Oncol Biol Phys* 2000; **47**: 103-113 [PMID: 10758311 DOI: 10.1016/s0360-3016(99)00560-x]
- 10 **Fiorino C**, Sanguineti G, Cozzarini C, Fellin G, Foppiano F, Menegotti L, Piazzolla A, Vavassori V, Valdagni R. Rectal dose-volume constraints in high-dose radiotherapy of localized prostate cancer. *Int J Radiat Oncol Biol Phys* 2003; **57**: 953-962 [PMID: 14575825 DOI: 10.1016/s0360-3016(03)00665-5]
- 11 **Zelevsky MJ**, Levin EJ, Hunt M, Yamada Y, Shippy AM, Jackson A, Amols HI. Incidence of late rectal and urinary toxicities after three-dimensional conformal radiotherapy and intensity-modulated radiotherapy for localized prostate cancer. *Int J Radiat Oncol Biol Phys* 2008; **70**: 1124-1129 [PMID: 18313526 DOI: 10.1016/j.ijrobp.2007.11.044]
- 12 **Jackson A**, Skwarchuk MW, Zelevsky MJ, Cowen DM, Venkatraman ES, Levegrun S, Burman CM, Kutcher GJ, Fuks Z, Liebel SA, Ling CC. Late rectal bleeding after conformal radiotherapy of prostate cancer. II. Volume effects and dose-volume histograms. *Int J Radiat Oncol Biol Phys* 2001; **49**: 685-698 [PMID: 11172950 DOI: 10.1016/s0360-3016(00)01414-0]
- 13 **Storey MR**, Pollack A, Zagars G, Smith L, Antolak J, Rosen I. Complications from radiotherapy dose escalation in prostate cancer: preliminary results of a randomized trial. *Int J Radiat Oncol Biol Phys* 2000; **48**: 635-642 [PMID: 11020558 DOI: 10.1016/s0360-3016(00)00700-8]
- 14 **Fiorino C**, Cozzarini C, Vavassori V, Sanguineti G, Bianchi C, Cattaneo GM, Foppiano F, Magli A, Piazzolla A. Relationships between DVHs and late rectal bleeding after radiotherapy for prostate cancer: analysis of a large group of patients pooled from three institutions. *Radiation Oncol* 2002; **64**: 1-12 [PMID: 12208568 DOI: 10.1016/s0167-8140(02)00147-0]
- 15 **Fiorino C**, Fellin G, Rancati T, Vavassori V, Bianchi C, Borca VC, Girelli G, Mapelli M, Menegotti L, Nava S, Valdagni R. Clinical and dosimetric predictors of late rectal syndrome after 3D-CRT for localized prostate cancer: preliminary results of a multicenter prospective study. *Int J Radiat Oncol Biol Phys* 2008; **70**: 1130-1137 [PMID: 17881142 DOI: 10.1016/j.ijrobp.2007.07.2354]
- 16 **Gulliford SL**, Foo K, Morgan RC, Aird EG, Bidmead AM, Critchley H, Evans PM, Gianolini S, Mayles WP, Moore AR, Sánchez-Nieto B, Partridge M, Sydes MR, Webb S, Dearnaley DP. Dose-volume constraints to reduce rectal side effects from prostate radiotherapy: evidence from MRC RT01 Trial ISRCTN 47772397. *Int J Radiat Oncol Biol Phys* 2010; **76**: 747-754 [PMID: 19540054 DOI: 10.1016/j.ijrobp.2009.02.025]
- 17 **Kotabe K**, Nakayama H, Takashi A, Takahashi A, Tajima T, Kume H. Association between rectal bleeding and the absolute dose volume of the rectum following image-guided radiotherapy for patients with prostate cancer. *Oncol Lett* 2018; **16**: 2741-2749 [PMID: 30013669 DOI: 10.3892/ol.2018.8888]
- 18 **Mariados N**, Sylvester J, Shah D, Karsh L, Hudes R, Beyer D, Kurtzman S, Bogart J, Hsi RA, Kos M, Ellis R, Logsdon M, Zimberg S, Forsythe K, Zhang H, Soffen E, Francke P, Mantz C, Rossi P, DeWeese T, Hamstra DA, Bosch W, Gay H, Michalski J. Hydrogel Spacer Prospective Multicenter Randomized Controlled Pivotal Trial: Dosimetric and Clinical Effects of Perirectal Spacer Application in Men Undergoing Prostate Image Guided Intensity Modulated Radiation Therapy. *Int J Radiat Oncol Biol Phys* 2015; **92**: 971-977 [PMID: 26054865 DOI: 10.1016/j.ijrobp.2015.04.030]
- 19 **Hamstra DA**, Mariados N, Sylvester J, Shah D, Karsh L, Hudes R, Beyer D, Kurtzman S, Bogart J, Hsi RA, Kos M, Ellis R, Logsdon M, Zimberg S, Forsythe K, Zhang H, Soffen E, Francke P, Mantz C, Rossi P, DeWeese T, Daignault-Newton S, Fischer-Valuck BW, Chundury A, Gay H, Bosch W, Michalski J. Continued Benefit to Rectal Separation for Prostate Radiation Therapy: Final Results of a Phase III Trial. *Int J Radiat Oncol Biol Phys* 2017; **97**: 976-985 [PMID: 28209443 DOI: 10.1016/j.ijrobp.2016.12.024]
- 20 **Herold DM**, Hanlon AL, Hanks GE. Diabetes mellitus: a predictor for late radiation morbidity. *Int J Radiat Oncol Biol Phys* 1999; **43**: 475-479 [PMID: 10078625 DOI: 10.1016/s0360-3016(98)00460-x]
- 21 **Feigenberg SJ**, Hanlon AL, Horwitz EM, Uzzo RG, Eisenberg D, Pollack A. Long-term androgen deprivation increases Grade 2 and higher late morbidity in prostate cancer patients treated with three-dimensional conformal radiation therapy. *Int J Radiat Oncol Biol Phys* 2005; **62**: 397-405 [PMID: 15890581 DOI: 10.1016/j.ijrobp.2004.10.021]
- 22 **Valdagni R**, Vavassori V, Rancati T, Fellin G, Baccolini M, Bianchi C, Cagna E, Gabriele P, Mauro F, Menegotti L, Monti AF, Stasi M,

- Fiorino C. Increasing the risk of late rectal bleeding after high-dose radiotherapy for prostate cancer: the case of previous abdominal surgery. Results from a prospective trial. *Radiother Oncol* 2012; **103**: 252-255 [PMID: 22521747 DOI: 10.1016/j.radonc.2012.03.012]
- 23 **Ishikawa H**, Hiroshima Y, Kanematsu N, Inaniwa T, Shirai T, Imai R, Suzuki H, Akakura K, Wakatsuki M, Ichikawa T, Tsuji H. Carbon-ion radiotherapy for urological cancers. *Int J Urol* 2022; **29**: 1109-1119 [PMID: 35692124 DOI: 10.1111/iju.14950]
- 24 **Akakura K**, Tsujii H, Morita S, Tsuji H, Yagishita T, Isaka S, Ito H, Akaza H, Hata M, Fujime M, Harada M, Shimazaki J; Working Group for Genitourinary Tumors, National Institute of Radiological Science. Phase I/II clinical trials of carbon ion therapy for prostate cancer. *Prostate* 2004; **58**: 252-258 [PMID: 14743464 DOI: 10.1002/pros.10328]
- 25 **Okada T**, Tsuji H, Kamada T, Akakura K, Suzuki H, Shimazaki J, Tsujii H; Working Group for Genitourinary Tumors. Carbon ion radiotherapy in advanced hypofractionated regimens for prostate cancer: from 20 to 16 fractions. *Int J Radiat Oncol Biol Phys* 2012; **84**: 968-972 [PMID: 22898380 DOI: 10.1016/j.ijrobp.2012.01.072]
- 26 **Sato H**, Kasuya G, Ishikawa H, Nomoto A, Ono T, Nakajima M, Isozaki Y, Yamamoto N, Iwai Y, Nemoto K, Ichikawa T, Tsuji H; Working Group for Genitourinary Tumors. Long-term clinical outcomes after 12-fractionated carbon-ion radiotherapy for localized prostate cancer. *Cancer Sci* 2021; **112**: 3598-3606 [PMID: 34107139 DOI: 10.1111/cas.15019]
- 27 **Hiroshima Y**, Ishikawa H, Iwai Y, Wakatsuki M, Utsumi T, Suzuki H, Akakura K, Harada M, Sakurai H, Ichikawa T, Tsuji H. Safety and Efficacy of Carbon-Ion Radiotherapy for Elderly Patients with High-Risk Prostate Cancer. *Cancers (Basel)* 2022; **14** [PMID: 36011007 DOI: 10.3390/cancers14164015]
- 28 **Ishikawa H**, Tsuji H, Kamada T, Hirasawa N, Yanagi T, Mizoe JE, Akakura K, Suzuki H, Shimazaki J, Tsujii H. Risk factors of late rectal bleeding after carbon ion therapy for prostate cancer. *Int J Radiat Oncol Biol Phys* 2006; **66**: 1084-1091 [PMID: 16979840 DOI: 10.1016/j.ijrobp.2006.06.056]
- 29 **Li P**, Hong Z, Li Y, Fu S, Zhang Q. Two-Year Toxicity and Efficacy of Carbon Ion Radiotherapy in the Treatment of Localized Prostate Cancer: A Single-Centered Study. *Front Oncol* 2021; **11**: 808216 [PMID: 35223457 DOI: 10.3389/fonc.2021.808216]
- 30 **Fukahori M**, Matsufoji N, Himukai T, Kanematsu N, Mizuno H, Fukumura A, Tsuji H, Kamada T. Estimation of late rectal normal tissue complication probability parameters in carbon ion therapy for prostate cancer. *Radiother Oncol* 2016; **118**: 136-140 [PMID: 26700600 DOI: 10.1016/j.radonc.2015.11.023]
- 31 **Choi K**, Molinelli S, Russo S, Mirandola A, Fiore MR, Vischioni B, Fossati P, Petrucci R, Turturici I, Dale JE, Valvo F, Ciocca M, Mairani A. Rectum Dose Constraints for Carbon Ion Therapy: Relative Biological Effectiveness Model Dependence in Relation to Clinical Outcomes. *Cancers (Basel)* 2019; **12** [PMID: 31877802 DOI: 10.3390/cancers12010046]
- 32 **Hawkins RB**. A Microdosimetric-Kinetic Model of Cell Killing by Irradiation from Permanently Incorporated Radionuclides. *Radiat Res* 2018; **189**: 104-116 [PMID: 29045193 DOI: 10.1667/RR14681.1]
- 33 **Kase Y**, Kanai T, Matsumoto Y, Furusawa Y, Okamoto H, Asaba T, Sakama M, Shinoda H. Microdosimetric measurements and estimation of human cell survival for heavy-ion beams. *Radiat Res* 2006; **166**: 629-638 [PMID: 17007551 DOI: 10.1667/RR0536.1]
- 34 **Kamada T**, Tsujii H, Blakely EA, Debus J, De Neve W, Durante M, Jäkel O, Mayer R, Orecchia R, Pötter R, Vatnitsky S, Chu WT. Carbon ion radiotherapy in Japan: an assessment of 20 years of clinical experience. *Lancet Oncol* 2015; **16**: e93-e100 [PMID: 25638685 DOI: 10.1016/S1470-2045(14)70412-7]
- 35 **Suit H**, DeLaney T, Goldberg S, Paganetti H, Clasié B, Gerweck L, Niemierko A, Hall E, Flanz J, Hallman J, Trifimov A. Proton vs carbon ion beams in the definitive radiation treatment of cancer patients. *Radiother Oncol* 2010; **95**: 3-22 [PMID: 20185186 DOI: 10.1016/j.radonc.2010.01.015]
- 36 **Fukata K**, Kawamura H, Kubo N, Kanai T, Torikoshi M, Nakano T, Tashiro M, Ohno T. Retrospective comparison of rectal toxicity between carbon-ion radiotherapy and intensity-modulated radiation therapy based on treatment plan, normal tissue complication probability model, and clinical outcomes in prostate cancer. *Phys Med* 2021; **90**: 6-12 [PMID: 34521017 DOI: 10.1016/j.ejmp.2021.08.013]
- 37 **Okonogi N**, Fukahori M, Wakatsuki M, Ohkubo Y, Kato S, Miyasaka Y, Tsuji H, Nakano T, Kamada T. Dose constraints in the rectum and bladder following carbon-ion radiotherapy for uterus carcinoma: a retrospective pooled analysis. *Radiat Oncol* 2018; **13**: 119 [PMID: 29941040 DOI: 10.1186/s13014-018-1061-7]

Observational Study

Incidence of exclusive extrapelvic skeletal metastasis in prostate carcinoma on bone scintigraphy

Parneet Singh, Kanhaiyalal Agrawal, Ashique Rahman, Tejasvini Singhal, Girish Kumar Parida, Gopinath Gnanasegaran

Specialty type: Radiology, nuclear medicine and medical imaging

Provenance and peer review:

Invited article; Externally peer reviewed.

Peer-review model: Single blind

Peer-review report's classification

Scientific Quality: Grade C

Novelty: Grade C

Creativity or Innovation: Grade C

Scientific Significance: Grade C

P-Reviewer: Song C

Received: May 8, 2024

Revised: June 8, 2024

Accepted: July 2, 2024

Published online: July 28, 2024

Processing time: 76 Days and 16.3 Hours



Parneet Singh, Kanhaiyalal Agrawal, Ashique Rahman, Tejasvini Singhal, Girish Kumar Parida, Department of Nuclear Medicine, All India Institute of Medical Sciences, Bhubaneswar 751019, Odisha, India

Gopinath Gnanasegaran, Department of Nuclear Medicine, Royal Free Hospital, London NW3 2QG, United Kingdom

Co-first authors: Parneet Singh and Kanhaiyalal Agrawal.

Corresponding author: Kanhaiyalal Agrawal, MBBS, MD, Additional Professor, Department of Nuclear Medicine, All India Institute of Medical Sciences, Sijua, Dumuduma, Bhubaneswar 751019, Odisha, India. nucmed_kanhaiyalal@aiimsbhubaneswar.edu.in

Abstract

BACKGROUND

Bone is one of the common sites of metastasis from prostate carcinoma. Bone scintigraphy (BS) is one of the most sensitive imaging modalities currently used for bone metastatic work-up. Skeletal metastasis in prostate carcinoma commonly involves pelvic bones but rarely involves extrapelvic-extraspinal sites.

AIM

To retrospectively analyze the BS data to determine the pattern of skeletal metastases in the prostate carcinoma.

METHODS

This retrospective observational study involves patients with biopsy-proven prostate carcinoma referred for BS for staging assessment. Patients with abnormal BS were evaluated for the pattern of skeletal involvement and data were presented in descriptive format in the form of percentages.

RESULTS

A total of 150 patients with biopsy-proven prostate cancer who were referred for staging were included in the study. Thirteen of 150 patients (8.67%) had no abnormal uptake on planar images, ruling out metastatic disease. Twenty-four patients (16%) had heterogeneous uptake in the spine with distribution characteristic of degenerative disease and no scan pattern of metastatic disease. Thirty patients (20%) had multifocal uptake involving both pelvic and extra pelvic bones

on planar images typical for skeletal metastasis and were considered metastatic. Eighty-three out of 150 patients (55.3%) had increased tracer uptake, which was indeterminate, thus, single photon emission computed tomography-computed tomography (SPECT-CT) was acquired, which showed 51 with metastatic disease, 31 benign lesions, and one indeterminate finding. Seven of 150 patients had exclusive pelvic bone uptake, which was found to be metastatic in 4/7 patients in SPECT-CT. Fifty six out of 150 patients showed exclusive extrapelvic tracer uptake, of which only 3 had vertebral metastatic disease. None of the patients with increased uptake exclusively in the extrapelvic-extraspinal location was metastatic.

CONCLUSION

The incidence of exclusive extrapelvic skeletal metastatic disease in prostate carcinoma is 2% (excluding one patient with indeterminate findings). Further, none of the patients in the current study had exclusive extrapelvic-extraspinal metastasis. Thus, exclusive extrapelvic-extraspinal focal abnormality on planar BS carries a very low probability of metastatic disease and hence, further imaging or SPECT-CT can be safely avoided in such cases.

Key Words: Pelvic; Prostate cancer; Bone scan; Single photon emission computed tomography-computed tomography; Skeletal metastasis

©The Author(s) 2024. Published by Baishideng Publishing Group Inc. All rights reserved.

Core Tip: The current study analyzed bone scintigraphy (BS) data from 150 patients with biopsy-proven prostate carcinoma to determine skeletal metastasis patterns. The most common site of skeletal metastasis was pelvis. The incidence of exclusive extrapelvic skeletal metastatic disease was 2%, excluding one indeterminate case. Additionally, no patients in the study had exclusive extrapelvic-extraspinal metastasis. Therefore, exclusive extrapelvic-extraspinal focal abnormalities on planar BS have a very low likelihood of being metastatic, making further imaging or single photon emission computed tomography-computed tomography often unnecessary.

Citation: Singh P, Agrawal K, Rahman A, Singhal T, Parida GK, Gnanasegaran G. Incidence of exclusive extrapelvic skeletal metastasis in prostate carcinoma on bone scintigraphy. *World J Radiol* 2024; 16(7): 265-273

URL: <https://www.wjgnet.com/1949-8470/full/v16/i7/265.htm>

DOI: <https://dx.doi.org/10.4329/wjr.v16.i7.265>

INTRODUCTION

Prostate carcinoma (PCa) is one of the most common cancers worldwide and stands as the second most commonly diagnosed cancer in men. It constitutes the 5th most common cause of cancer-related death[1]. The prevalence of PCa increases with age. About less than 5% of individuals under the age of 30 years harbor PCa, while this rises to greater than 59% in those with age above 80 years[2-4]. Skeleton is the most common site for metastatic disease involvement in PCa. Radionuclide bone scintigraphy (BS) is one of the most sensitive investigations for screening of skeletal metastases in PCa with the added advantage of low cost and the ability to screen the entire skeleton in a single study[5,6].

In PCa, pelvic bones, followed by the spine, represent the most common site of metastatic bone disease. This can be attributed to the low resistance venous connection between the periprostatic venous plexus and valveless vertebral venous plexus of Batson and the presence of a highly conducive microenvironment due to abundant red marrow, particularly in the pelvic bones providing the ideal “soil” for metastatic disease development[7-9]. Involvement of other bones without involvement of pelvic bones and spine is rarely encountered. We retrospectively analyzed the BS data to determine the pattern of bone metastases in PCa[5,10,11].

MATERIALS AND METHODS

The study involved a retrospective analysis of BS data of prostate cancer patients referred to the Department of Nuclear Medicine who underwent whole-body skeletal scintigraphy between August 2016 to June 2023. All patients with histopathologically proven PCa referred for whole-body BS for metastatic work-up were reviewed. Patients’ details, clinical history, result of other imaging modalities and follow-up of the patients were recorded. The study was performed in accordance with the Declaration of Helsinki and after receiving approval from the institutional ethical committee (No. T/IM-NF/Nucl.Med/23/187).

Inclusion criteria

(1) Histopathologically proven PCa; (2) Patient referred for initial staging work-up; and (3) No history of prior hormonal therapy, radiotherapy, chemotherapy, or any other form of systemic therapy.

Exclusion criteria

(1) Histopathological diagnosis not available; or (2) History of prior systemic therapy.

Image acquisition

BS imaging protocol: Whole body BS was performed after intravenous administration of 20-25 mCi (740-925 MBq) of Tc-99m methylene diphosphonate (MDP) following SNMMI Procedure Standard for BS 4.0. Images were acquired on a dual-head gamma camera (Discovery NM/CT 670, GE Healthcare) using a low energy high-resolution parallel hole collimator with an energy window width of 20% centered at 140 KeV. Whole body planar images were acquired 3 hours after tracer injection in anterior and posterior views with a matrix size of 1024 × 256[12].

Regional single-photon emission computed tomography (SPECT)-computed tomography (CT) was acquired in patients with indeterminate and suspicious lesions on planar images. The SPECT was acquired in a step-and-shoot manner with 60 stops, 25 seconds/stop, and angular movement of 3 degrees/head/stop using a matrix size of 128 × 128 and co-registered with CT (low-dose non-contrast 16 slice CT acquired keeping 120 KVp, 50 mAs tube energy setting). The images were analyzed using the Xeleris 4.0 workstation. SPECT-CT images were processed with 8 iterations and sub-sets and co-registration with CT was done on Volumetric MI software to form fused 3D images[12].

Image interpretation

The scans were interpreted individually by two experienced nuclear medicine physicians. The scans were categorized as positive, negative, or suspicious/indeterminate for skeletal metastases on planar studies. The tracer uptake on planar BS was reported positive for metastasis when there is a classical pattern for metastatic disease involvement, like multiple foci of uptake. The scan was reported as negative when it conforms to the physiological distribution of the tracer or to the typical pattern of benign disease viz degenerative changes, arthritis, *etc.* In suspicious/indeterminate uptake, SPECT/CT of the corresponding region was available in all cases. SPECT/CT was interpreted as positive, negative or indeterminate for metastasis. In case of discordancy of results, the help of a third nuclear medicine physician was sought, and the final result was made on the basis of consensus.

Statistical analysis

The data were analysed on a per-patient basis, and the incidence of multiple metastases, including pelvic and extrapelvic, exclusive extrapelvic, and exclusive extrapelvic/extraspinal metastasis, was recorded. The data are presented in descriptive format in the form of percentages.

RESULTS

A total of 150 patients with biopsy-proven prostate cancer for staging were included in the study. The median age of included patients was 68.7 years (range: 42-86 years). A total of 81/150 patients showed metastatic disease.

Thirteen of 150 patients (8.67%) had no abnormal uptake on planar images ruling out metastatic disease. Twenty-four patients (16%) had heterogenous uptake in the spine with distribution characteristic of degenerative disease and no scan pattern of metastatic disease. Thirty patients (20%) had multifocal uptake involving both pelvic and extra pelvic bones on planar images typical for skeletal metastasis and were considered metastatic (Table 1).

Eighty-three out of 150 patients (55.3%) had increased tracer uptake on whole-body planar images, which were indeterminate or suspicious for metastatic disease. Thus, SPECT-CT was acquired to characterize the uptake further (Table 2). Forty-four of 83 patients (53%) had more than five foci of abnormally increased osteoblastic activity involving all pelvic, spinal, and extraspinal sites, and SPECT-CT was performed to confirm the metastatic disease. All of these patients were found to be metastatic on SPECT-CT. Focal osteoblastic activity localizing exclusively to the pelvis was seen in 7 patients, with 4 patients proven to be metastatic, and 3 patients having benign uptake on SPECT-CT. Thus, pondering a very high relative risk of isolated pelvic focal osteoblastic activity being malignant. The remaining 32 out of 83 patients showed abnormal exclusive extra pelvic tracer uptake. These included 20 patients with vertebral (17 benign and 3 metastatic) as shown in Figure 1, and 12 patients with exclusive extrapelvic extraspinal uptake (11 benign and 1 indeterminate) as shown in Figures 2-4. None of the patients with osteoblastic abnormality exclusively in the extrapelvic-extraspinal regions on planar BS was metastatic. One patient had focal uptake in the skull and was deemed indeterminate on SPECT-CT.

Exclusive extrapelvic

Thus, in total, of all patients showing exclusive extrapelvic uptake (56 patients), only three were metastatic (all vertebral metastatic disease) (Table 3). Exclusive extrapelvic/extraspinal uptake was found in a total of 12 patients, of which locations of uptake were ribs (7/12), sternum and manubriosternal joint (2/12), and skull (3/12). None of these exclusive extra pelvic-extraspinal sites of abnormal tracer uptake was malignant on SPECT-CT. Thus, pondering a negligible risk of metastatic skeletal disease in absence of pelvic and spinal bones involvement. Table 4 elaborates the SPECT-CT findings in solitary extra pelvic uptake. Most common site for metastatic disease involvement were pelvic bones followed by vertebrae and ribs (Table 5).

Table 1 Planar bone scintigraphy findings

Pattern of uptake on bone scan	Number of patients among, n = 150
No abnormal increased osteoblastic activity	13
Increased uptake with pattern typical of degenerative changes/benign uptake	24
Multifocal increased uptake typical for metastatic disease	30
Indeterminate or suspicious for metastatic uptake where SPECT-CT was performed	83

SPECT-CT: Single photon emission computed tomography-computed tomography.

Table 2 Single photon emission computed tomography-computed tomography findings

Lesion	Number of patients among, n = 83
Benign	31
Metastatic	51
Indeterminate	1

Table 3 Location of uptake and characterization in patients with exclusive extrapelvic uptake

Site of uptake	Benign	Metastatic	Indeterminate
Vertebra	41	3	0
Ribs	7	0	0
Sternum and manubriosternal region	2	0	0
Skull	2	0	1

Table 4 Single photon emission computed tomography-computed tomography characterization of isolated extrapelvic uptake

Serial No.	Age in years	Site of uptake	SPECT-CT findings	Final diagnosis
1	67	Left 1 st rib	Arthritis	Benign
2	83	Right 5 th rib	Fibrous dysplasia	Benign
3	66	Right 6 th rib	Fracture line likely post traumatic	Benign
4	63	Right 11 th rib	Fracture line likely post traumatic	Benign
5	72	Right 6 th rib	Fracture line likely post traumatic	Benign
6	60	Sternum	Manubriosternal joint	Benign
7	76	Right parietal bone	Subtle sclerosis not typical for metastatic disease	Indeterminate

SPECT-CT: Single photon emission computed tomography-computed tomography.

DISCUSSION

In this study, we found pelvic bones and vertebrae to be the most common sites of metastatic disease in PCa. Further, this study demonstrates that the risk of a metastatic disease of an extra-pelvic/extraspinal uptake in PCa is negligible. Exclusive extrapelvic osteoblastic activity localizing to the spine has a less but significant risk of metastatic disease (15%).

PCa is relatively indolent and has slow growth. Thus, PCa has a favorable prognosis. The 5-year survival rates approach nearly 100% for localized as well as locoregional disease. However, this reduces to almost 34% once the patient has metastatic disease. Thus, marking the importance of early diagnosis of metastatic disease in PCa. With the implementation of early detection strategies like prostate-specific antigen screening programs, the majority of the cases are diagnosed in the early stages[2,6,13-15]. At diagnosis, about 78% of the patients have localized disease, while 16% of patients have locoregional lymph nodal involvement, and only 6% of cases have metastatic disease.

Table 5 Site of metastatic disease on bone scintigraphy

Site	Number of patients
Super-scan	10
Pelvic bones	68
Vertebrae	63
Ribs	55
Sternum	42
Femur	41
Scapula	41
Skull	32
Clavicle	29
Humerus	23
Others	7 (4 tibia, 2 forearm bones, 1 maxilla)

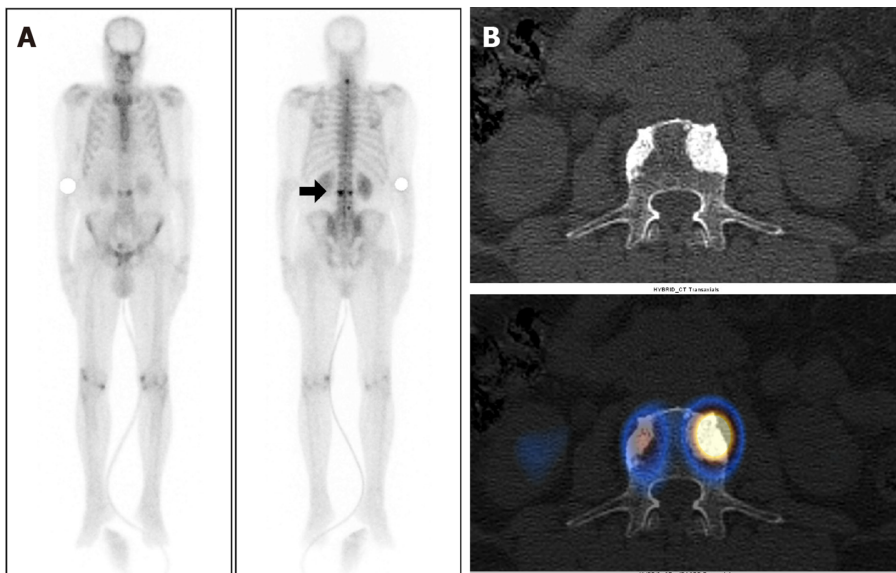


Figure 1 A 74-year-old male, with a newly diagnosed case of carcinoma of the prostate [Gleason's Score 7 (4 + 3)] with serum prostate-specific antigen level 491 ng/mL and underwent whole body bone scintigraphy. A: ^{99m}Tc methylene diphosphonate Whole body planar images show focal increased tracer uptake involving the cervical and lumbar vertebrae (arrow) raising the suspicion of metastatic disease; B: Axial computed tomography (CT) and fused single photon emission computed tomography (SPECT)-CT images show tracer localization to sclerotic lesion involving L3 vertebrae suggestive of metastatic disease. No metastatic disease was seen in pelvic bones on SPECT-CT.

Bone and bone marrow, providing the ideal site for metastatic disease development, constitute the most common site for metastatic disease involvement of PCa. Lymph nodes, lung and liver follow this. Approximately 60% of patients progress to metastatic disease throughout management, and approximately 80% of patients with fatal progressive PCa harbor bone metastasis [16,17]. Bone metastasis commonly localizes to pelvic bones. This is hypothesized to be secondary to the retrograde spread of the tumor *via* the venous communication between the low resistance periprostatic venous plexus and Batson's plexus. BS is the most commonly used imaging modality for the assessment of bone metastasis in PCa staging. BS can be performed using ^{99m}Tc MDP and ^{99m}Tc HDP (hydroxymethylene diphosphonate). These radiopharmaceuticals, when injected intravenously, get rapidly chemisorbed onto the hydroxyapatite crystals and more so at the sites of increased osteoblastic activity, thus highlighting the skeletal involvement with high sensitivity [8,18-20].

However, not all areas of increased osteoblastic activity are metastatic, and they may represent some benign pathology. Thus, emanating its limited specificity. The use of targeted SPECT/CT offers more specific diagnostic options in this subgroup of patients. It adds anatomical information of CT with functional information of SPECT and can help rule out benign causes of increased tracer uptake and confirm the metastatic disease. SPECT/CT, however, is associated with increased patient radiation burden by its CT component and adds to the total scan time. It adds approximately 0.5 to 2.6 mSv of radiation dose to the patient and approximately ≥ 12 mins to the acquisition time, depending on the area imaged. Thus, employing the need for caution while performing SPECT/CT [21-23]. Further, it is not always available in all

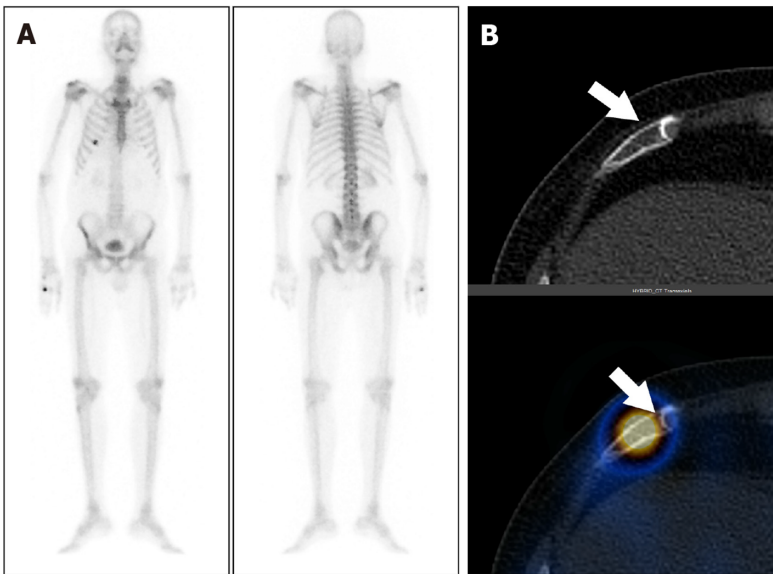


Figure 2 A 66-year-old male with carcinoma of the prostate and serum prostate-specific antigen of 23.3 ng/mL. A: Staging with whole body bone scintigraphy show focal areas of increased tracer uptake involving the right 6th rib; B: Axial computed tomography (CT) and fused single photon emission computed tomography-CT images show tracer localization to the right 6th rib anteriorly with a fracture line (arrow). The uptake was thus secondary to rib fracture post traumatic. There was no other abnormal uptake anywhere in the bones on whole body study.

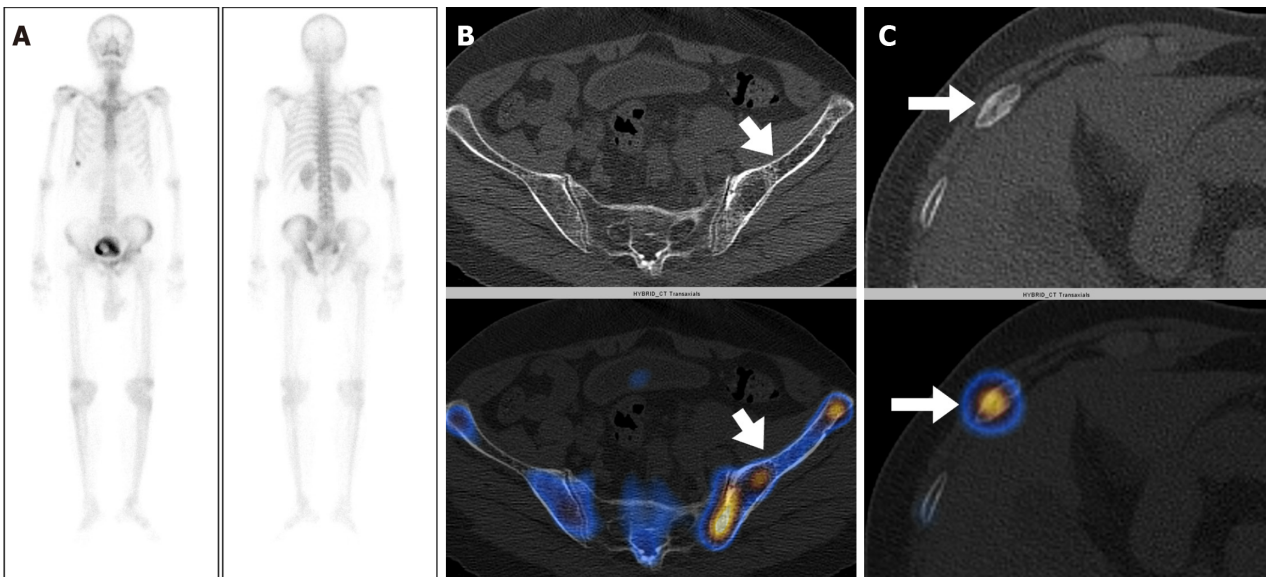


Figure 3 A 77-year-old male with carcinoma of the prostate and a Gleason's Score 8 (4 + 4) and serum prostate-specific antigen level of 100 ng/mL. A: Staging whole body bone scintigraphy show heterogeneously increased tracer uptake involving the left hemipelvis and focal areas of increased tracer uptake involving the right 8th rib raising the suspicion of metastatic disease; B and C: Axial computed tomography (CT) and fused single photon emission computed tomography-CT images localizes the tracer to the left iliac bone with cortical thickening and bony expansion consistent with Paget's disease (arrow in B) and to the right 8th rib anteriorly with a fracture line (arrow in C).

Nuclear Medicine departments.

Skeletal metastasis from PCa commonly localizes to pelvic bones followed by vertebrae. Isolated focal areas of uptake, apart from these regions, are rarely due to skeletal metastasis[13,14,17]. Wang *et al*[24] studied the distribution of skeletal metastasis in PCa and found vertebrae and pelvis to be the most frequent sites to harbor metastasis. Only 1% of patients had exclusive extrapelvic-extraspinal metastasis. The present study revealed metastatic disease involvement only in 3 patients (2%) with extra-pelvic skeletal disease in the absence of pelvic bone involvement. All three patients had involvement of vertebrae. None of the 150 patients had exclusive extrapelvic-extraspinal skeletal metastasis.

In an autopsy study by Mintz and Smith[25], including 100 patients of PCa, 21 patients had bone metastasis, and all the cases had involvement of the axial skeleton, with no incidence of isolated appendicular skeleton involvement. The pelvis was the most common site for metastatic disease and was involved in 13/21 cases. Similar results were observed by Roth *et al*[14] where axial skeleton involvement was found in all the patients ($n = 54$), while pelvic involvement was observed

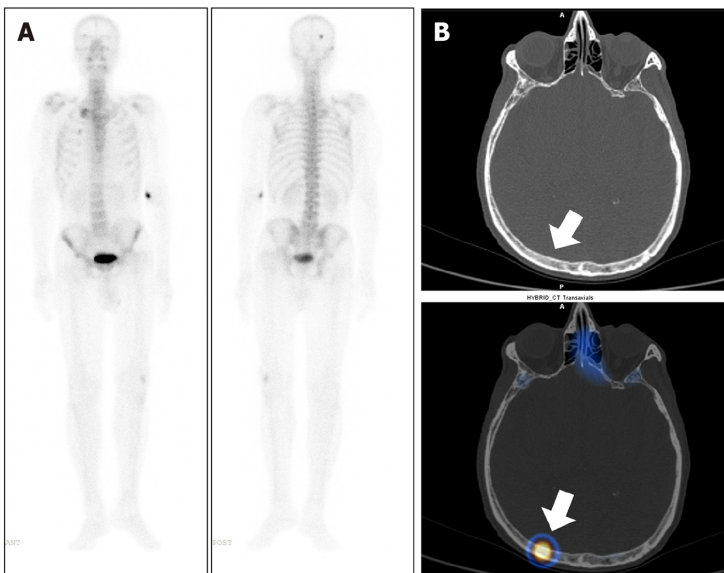


Figure 4 A 76-year-old male, with a newly diagnosed case of carcinoma of the prostate underwent whole body bone scintigraphy. A: ^{99m}Tc methylene diphosphonate Whole body planar images show solitary focal area of increased tracer uptake involving skull bone on the right side; B: Axial computed tomography (CT) and fused single photon emission computed tomography-CT images show tracer localization to the right parietal bone (arrow) with no significant CT abnormality to suggest of metastatic disease involvement. The lesion was thus considered indeterminate.

in 92.5% ($n = 50$) of patients. Also, in another autopsy study by Bubendorf *et al*[6], the axial skeleton was the predominant site of skeletal metastasis, with exclusively extrapelvic-extraspinal metastasis skeleton being rarely involved. Thus, fortifying the hypothesis of the current study.

The current study's limitations include a retrospective design, limited sample size, lack of survival data, and lack of histopathology confirmation of the BS findings.

CONCLUSION

The incidence of exclusive extrapelvic skeletal metastatic disease in PCa is 2% (excluding one patient with indeterminate findings). None of the patients in the current study had exclusive extrapelvic-extraspinal metastasis. Thus, exclusive extrapelvic-extraspinal focal abnormality on planar BS carries a very low probability of metastatic disease, and hence, further imaging or SPECT/CT can be safely avoided in such cases.

FOOTNOTES

Author contributions: Singh P and Agrawal K contributed to conception and design; Singh P and Singhal T contributed to drafting the manuscript; Agrawal K, Parida GK and Gnanasegaran G contributed to analysis and interpretation of data; Rahman A contributed to data collection, interpretation of data; All authors have confirmed the final approval.

Institutional review board statement: The study was approved by the institutional review board under IEC No. T/IM-NF/Nucl.Med/23/187.

Informed consent statement: Patients were not required to give informed consent to the study as the current study is a retrospective analysis of data and study was performed maintaining anonymity of the patients. The scintigraphy data were obtained after each patient agreed to the imaging by written consent.

Conflict-of-interest statement: All the authors report no relevant conflicts of interest for this article.

Data sharing statement: The data used to support the findings of this study are available from the corresponding author upon request at nucmed_kanhaiyalal@aiimshubaneswar.edu.in.

STROBE statement: The authors have read the STROBE Statement-checklist of items, and the manuscript was prepared and revised according to the STROBE Statement-checklist of items.

Open-Access: This article is an open-access article that was selected by an in-house editor and fully peer-reviewed by external reviewers. It is distributed in accordance with the Creative Commons Attribution NonCommercial (CC BY-NC 4.0) license, which permits others to distribute, remix, adapt, build upon this work non-commercially, and license their derivative works on different terms, provided the

original work is properly cited and the use is non-commercial. See: <https://creativecommons.org/licenses/by-nc/4.0/>

Country of origin: India

ORCID number: Kanhaiyalal Agrawal 0000-0003-4855-8938.

S-Editor: Li L

L-Editor: Filipodia

P-Editor: Zhang XD

REFERENCES

- 1 **Sung H**, Ferlay J, Siegel RL, Laversanne M, Soerjomataram I, Jemal A, Bray F. Global Cancer Statistics 2020: GLOBOCAN Estimates of Incidence and Mortality Worldwide for 36 Cancers in 185 Countries. *CA Cancer J Clin* 2021; **71**: 209-249 [PMID: 33538338 DOI: 10.3322/caac.21660]
- 2 **Soerjomataram I**, Bray F. Planning for tomorrow: global cancer incidence and the role of prevention 2020-2070. *Nat Rev Clin Oncol* 2021; **18**: 663-672 [PMID: 34079102 DOI: 10.1038/s41571-021-00514-z]
- 3 **Schaeffer EM**, Srinivas S, Adra N, An Y, Barocas D, Bitting R, Bryce A, Chapin B, Cheng HH, D'Amico AV, Desai N, Dorff T, Eastham JA, Farrington TA, Gao X, Gupta S, Guzzo T, Ippolito JE, Kuettel MR, Lang JM, Lotan T, McKay RR, Morgan T, Netto G, Pow-Sang JM, Reiter R, Roach M, Robin T, Rosenfeld S, Shabsigh A, Spratt D, Teplý BA, Tward J, Valicenti R, Wong JK, Shead DA, Snedeker J, Freedman-Cass DA. Prostate Cancer, Version 4.2023, NCCN Clinical Practice Guidelines in Oncology. *J Natl Compr Canc Netw* 2023; **21**: 1067-1096 [PMID: 37856213 DOI: 10.6004/jnccn.2023.0050]
- 4 **World Health Organization**. Global Health Estimates 2020: Prostate Source: Globocan 2020 Number of new cases in 2020, both sexes, all ages. 2020. [cited 27 June 2024]. Available from: <https://gco.iarc.fr/today>
- 5 **San Francisco IF**, Rojas PA, Bravo JC, Díaz J, Ebel L, Urrutia S, Prieto B, Cerda-Infante J. Can We Predict Prostate Cancer Metastasis Based on Biomarkers? *Int J Mol Sci* 2023; **24** [PMID: 37569883 DOI: 10.3390/ijms241512508]
- 6 **Bubendorf L**, Schöpfer A, Wagner U, Sauter G, Moch H, Willi N, Gasser TC, Mihatsch MJ. Metastatic patterns of prostate cancer: an autopsy study of 1,589 patients. *Hum Pathol* 2000; **31**: 578-583 [PMID: 10836297 DOI: 10.1053/hp.2000.6698]
- 7 **Clarke NW**, Hart CA, Brown MD. Molecular mechanisms of metastasis in prostate cancer. *Asian J Androl* 2009; **11**: 57-67 [PMID: 19050684 DOI: 10.1038/aja.2008.29]
- 8 **Akin O**, Hricak H. Imaging of prostate cancer. *Radiol Clin North Am* 2007; **45**: 207-222 [PMID: 17157630 DOI: 10.1016/j.rcl.2006.10.008]
- 9 **Brook R**, Tung K, Oeppen R. Batson's plexus and retrograde venous spread of malignancy – a pictorial review. *Cancer Imaging* 2014; **14**: P40 [DOI: 10.1186/1470-7330-14-s1-p40]
- 10 **Manna F**, Karkampouna S, Zoni E, De Menna M, Hensel J, Thalmann GN, Kruithof-de Julio M. Metastases in Prostate Cancer. *Cold Spring Harb Perspect Med* 2019; **9** [PMID: 29661810 DOI: 10.1101/cshperspect.a033688]
- 11 **Roudier MP**, Vesselle H, True LD, Higano CS, Ott SM, King SH, Vessella RL. Bone histology at autopsy and matched bone scintigraphy findings in patients with hormone refractory prostate cancer: the effect of bisphosphonate therapy on bone scintigraphy results. *Clin Exp Metastasis* 2003; **20**: 171-180 [PMID: 12705638 DOI: 10.1023/a:1022627421000]
- 12 **Beheshti M**, Langsteger W, Fogelman I. Prostate cancer: role of SPECT and PET in imaging bone metastases. *Semin Nucl Med* 2009; **39**: 396-407 [PMID: 19801219 DOI: 10.1053/j.semnuclmed.2009.05.003]
- 13 **McDavid K**, Lee J, Fulton JP, Tonita J, Thompson TD. Prostate cancer incidence and mortality rates and trends in the United States and Canada. *Public Health Rep* 2004; **119**: 174-186 [PMID: 15192905 DOI: 10.1177/003335490411900211]
- 14 **Roth AR**, Harmon SA, Perk TG, Eickhoff J, Choyke PL, Kurdziel KA, Dahut WL, Apolo AB, Morris MJ, Perlman SB, Liu G, Jeraj R. Impact of Anatomic Location of Bone Metastases on Prognosis in Metastatic Castration-Resistant Prostate Cancer. *Clin Genitourin Cancer* 2019; **17**: 306-314 [PMID: 31221545 DOI: 10.1016/j.clgc.2019.05.013]
- 15 **Hariharan K**, Padmanabha V. Demography and disease characteristics of prostate cancer in India. *Indian J Urol* 2016; **32**: 103-108 [PMID: 27127351 DOI: 10.4103/0970-1591.174774]
- 16 **Deek MP**, Taparra K, Dao D, Chan L, Phillips R, Gao RW, Kwon ED, Deville C, Song DY, Greco S, Carducci MA, Eisenberger M, DeWeese TL, Denmeade S, Pienta K, Paller CJ, Antonarakis ES, Olivier KR, Park SS, Stish BJ, Tran PT. Patterns of Recurrence and Modes of Progression After Metastasis-Directed Therapy in Oligometastatic Castration-Sensitive Prostate Cancer. *Int J Radiat Oncol Biol Phys* 2021; **109**: 387-395 [PMID: 32798608 DOI: 10.1016/j.ijrobp.2020.08.030]
- 17 **Quinn M**, Babb P. Patterns and trends in prostate cancer incidence, survival, prevalence and mortality. Part I: international comparisons. *BJU Int* 2002; **90**: 162-173 [PMID: 12081758 DOI: 10.1046/j.1464-410x.2002.2822.x]
- 18 **Hayward SJ**, McIvor J, Burdge AH, Jewkes RF, Williams G. Staging of prostatic carcinoma with radionuclide bone scintigraphy and lymphography. *Br J Radiol* 1987; **60**: 79-81 [PMID: 3814999 DOI: 10.1259/0007-1285-60-709-79]
- 19 **Berish RB**, Ali AN, Telmer PG, Ronald JA, Leong HS. Translational models of prostate cancer bone metastasis. *Nat Rev Urol* 2018; **15**: 403-421 [PMID: 29769644 DOI: 10.1038/s41585-018-0020-2]
- 20 **Wong SK**, Mohamad NV, Giaze TR, Chin KY, Mohamed N, Ima-Nirwana S. Prostate Cancer and Bone Metastases: The Underlying Mechanisms. *Int J Mol Sci* 2019; **20** [PMID: 31137764 DOI: 10.3390/ijms20102587]
- 21 **Tulik M**, Tulik P, Kowalska T. On the optimization of bone SPECT/CT in terms of image quality and radiation dose. *J Appl Clin Med Phys* 2020; **21**: 237-246 [PMID: 33111500 DOI: 10.1002/acm2.13069]
- 22 **Alrehily FA**, Alqahtani KS, Aljohani MH, Alharbi NS, Alharbi RM, Abdulaal OM, Alshamrani AF, Alsaedi AS, Al-Murshedi SH, Alhazmi FH. Establishing local diagnostic reference levels for computed tomography examinations using size-specific dose estimates. *Saudi Med J* 2023; **44**: 761-766 [PMID: 37582572 DOI: 10.15537/smj.2023.44.8.20230230]
- 23 **Gupta SK**, Trethewey S, Brooker B, Rutherford N, Diffey J, Viswanathan S, Attia J. Radionuclide bone scan SPECT-CT: lowering the dose of

- CT significantly reduces radiation dose without impacting CT image quality. *Am J Nucl Med Mol Imaging* 2017; **7**: 63-73 [PMID: 28533938]
- 24 **Wang C**, Shen Y, Zhu S. Distribution Features of Skeletal Metastases: A Comparative Study between Pulmonary and Prostate Cancers. *PLoS One* 2015; **10**: e0143437 [PMID: 26599401 DOI: 10.1371/journal.pone.0143437]
- 25 **Mintz ER**, Smith GG. Autopsy Findings in 100 Cases of Prostatic Cancer. *N Engl J Med* 1934; **211**: 479-487 [DOI: 10.1056/nejm193409132111101]

Evaluating the role of 7-Tesla magnetic resonance imaging in neurosurgery: Trends in literature since clinical approval

Arosh S Perera Molligoda Arachchige, Sarah Meuli, Francesca Romana Centini, Niccolò Stomeo, Federica Catapano, Letterio S Politi

Specialty type: Radiology, nuclear medicine and medical imaging

Provenance and peer review: Invited article; Externally peer reviewed.

Peer-review model: Single blind

Peer-review report's classification

Scientific Quality: Grade C

Novelty: Grade B

Creativity or Innovation: Grade B

Scientific Significance: Grade C

P-Reviewer: Yu RQ

Received: April 6, 2024

Revised: May 8, 2024

Accepted: June 17, 2024

Published online: July 28, 2024

Processing time: 108 Days and 13.2 Hours



Arosh S Perera Molligoda Arachchige, Sarah Meuli, Francesca Romana Centini, Faculty of Medicine, Humanitas University, Pieve Emanuele, Milan 20072, Italy

Niccolò Stomeo, Department of Anaesthesiology and Intensive Care, IRCCS Humanitas Research Hospital, Via Manzoni 56, Rozzano, Milan 20089, Italy

Niccolò Stomeo, Federica Catapano, Letterio S Politi, Department of Biomedical Sciences, Humanitas University, via Rita Levi Montalcini 4, 20090 Pieve Emanuele - Milan, Italy

Federica Catapano, IRCCS Humanitas Research Hospital, Via Manzoni 56, 20089 Rozzano - Milan, Italy

Letterio S Politi, Department of Neuroradiology, IRCCS Humanitas Research Hospital, Via Manzoni 56, Rozzano, Milan 20089, Italy

Corresponding author: Letterio S Politi, MD, Professor, Department of Biomedical Sciences, Humanitas University, Via Rita Levi Montalcini 4, Pieve Emanuele, Milan 20072, Italy. letterio.politi@hunimed.eu

Abstract

BACKGROUND

After approval for clinical use in 2017, early investigations of ultra-high-field abdominal magnetic resonance imaging (MRI) have demonstrated its feasibility as well as diagnostic capabilities in neuroimaging. However, there are no to few systematic reviews covering the entirety of its neurosurgical applications as well as the trends in the literature with regard to the aforementioned application.

AIM

To assess the impact of 7-Tesla MRI (7T MRI) on neurosurgery, focusing on its applications in diagnosis, treatment planning, and postoperative assessment, and to systematically analyze and identify patterns and trends in the existing literature related to the utilization of 7T MRI in neurosurgical contexts.

METHODS

A systematic search of PubMed was conducted for studies published between January 1, 2017, and December 31, 2023, using MeSH terms related to 7T MRI and neurosurgery. The inclusion criteria were: Studies involving patients of all ages, meta-analyses, systematic reviews, and original research. The exclusion criteria

were: Pre-prints, studies with insufficient data (*e.g.*, case reports and letters), non-English publications, and studies involving animal subjects. Data synthesis involved standardized extraction forms, and a narrative synthesis was performed.

RESULTS

We identified 219 records from PubMed within our defined period, with no duplicates or exclusions before screening. After screening, 125 articles were excluded for not meeting inclusion criteria, leaving 94 reports. Of these, 2 were irrelevant to neurosurgery and 7 were animal studies, resulting in 85 studies included in our systematic review. Data were categorized by neurosurgical procedures and diseases treated using 7T MRI. We also analyzed publications by country and the number of 7T MRI facilities per country was also presented. Experimental studies were classified into comparison and non-comparison studies based on whether 7T MRI was compared to lower field strengths.

CONCLUSION

7T MRI holds great potential in improving the characterization and understanding of various neurological and psychiatric conditions that may be neurosurgically treated. These include epilepsy, pituitary adenoma, Parkinson's disease, cerebrovascular diseases, trigeminal neuralgia, traumatic head injury, multiple sclerosis, glioma, and psychiatric disorders. Superiority of 7T MRI over lower field strengths was demonstrated in terms of image quality, lesion detection, and tissue characterization. Findings suggest the need for accelerated global distribution of 7T magnetic resonance systems and increased training for radiologists to ensure safe and effective integration into routine clinical practice.

Key Words: 7-Tesla; Magnetic resonance imaging; Neuroimaging; Neurosurgery; Pathologies; Procedures; Trends

©The Author(s) 2024. Published by Baishideng Publishing Group Inc. All rights reserved.

Core Tip: Frequent neurosurgical procedures using 7-Tesla magnetic resonance imaging (7T MRI) include endoscopic neurosurgery, resective epilepsy surgery, and deep brain stimulation, addressing conditions like cerebrovascular diseases, epilepsy, pituitary adenoma, and gliomas. Leading in publications are the United States, Netherlands, South Korea, and Japan. 7T MRI enhances the understanding of neurological and psychiatric disorders, showing superiority in image quality, lesion detection, and tissue characterization, underscoring the need for global deployment and improved radiologist training.

Citation: Perera Molligoda Arachchige AS, Meuli S, Centini FR, Stomeo N, Catapano F, Politi LS. Evaluating the role of 7-Tesla magnetic resonance imaging in neurosurgery: Trends in literature since clinical approval. *World J Radiol* 2024; 16(7): 274-293

URL: <https://www.wjgnet.com/1949-8470/full/v16/i7/274.htm>

DOI: <https://dx.doi.org/10.4329/wjr.v16.i7.274>

INTRODUCTION

In the realm of modern medicine, the field of neurosurgery stands as a testament to the remarkable progress achieved through advancements in technology and imaging. The delicate and intricate nature of the human brain necessitates tools and techniques that allow for precise diagnosis, treatment planning, and surgical intervention. Among the many innovations that have revolutionized the field, one technology has emerged as a promising game-changer: The 7-Tesla magnetic resonance imaging (7T MRI) scanner which received United States FDA approval for clinical use in 2017[1-3]. The introduction of 7T MRI represents a pivotal moment in the history of neurosurgery. This remarkable imaging technology harnesses the power of ultra-high magnetic fields to produce images with unprecedented detail and resolution, far surpassing the capabilities of conventional magnetic resonance imaging (MRI) scanners[4]. By capitalizing on the inherent magnetic properties of hydrogen nuclei within the human body, 7T MRI offers both neurosurgeons and neurologists an invaluable tool to investigate deeper into the intricate structures of the brain, enabling them to make more precise assessments of pathologies and formulate optimized treatment strategies[5,6]. Traditionally, neurosurgery has relied upon lower field strength MRI machines, typically operating at 1.5 or 3 T. While these systems have been instrumental in guiding surgical interventions and aiding in preoperative planning, they often fall short in providing the level of detail required for complex neurosurgical cases[2,3]. The limitations of lower field strength MRI, such as reduced spatial resolution and limited contrast, have posed challenges in accurately delineating critical structures, identifying subtle abnormalities, and characterizing lesions, ultimately affecting the quality and safety of neurosurgical procedures[5,6]. The emergence of 7T MRI, with its higher magnetic field strength, has raised the bar for neuroimaging capabilities. It promises to unveil new dimensions of information that were previously concealed, shedding light on intricate anatomical details and subtle pathologies that were once elusive[5,6]. This newfound precision has the potential to redefine the landscape of neurosurgery by offering enhanced preoperative assessment and surgical guidance, ultimately leading to improved patient outcomes and reduced surgical risks. This systematic review aims to systematically analyze and

identify patterns and trends within the existing literature on the utilization of 7T MRI in neurosurgical contexts, focusing on its applications in the diagnosis, treatment planning, and postoperative assessment of various neurosurgically treated pathologies.

MATERIALS AND METHODS

A systematic search of the PubMed database was conducted to identify relevant studies published between January 1, 2017 and December 31, 2021, using the following MeSH search terms: ((7T MRI) AND (neurosurgery)). Two independent reviewers performed the initial search and screening, with the inclusion criteria encompassing studies involving patients of all ages (both pediatric and adults) where 7-T MRI imaging was performed and/or compared with conventional MRI imaging in the context of neurosurgery. Eligible study types included meta-analyses, systematic reviews, and original research. The exclusion criteria involved studies with insufficient data such as case reports, publications not in English, and studies of animal subjects. Data synthesis involved standardized extraction forms. Our objective was to analyze trends in the literature as well as to provide a comprehensive and descriptive overview of research conducted within the specified time frame. Given the nature of our research question and the scope of our analysis, we chose not to perform a formal risk of bias assessment for individual studies using QUADAS or Rob2[7-9]. Our decision was based on the recognition that our aim was to capture and summarize the breadth of research in this field rather than to make judgments about the quality or internal validity of the included studies, nor the determination of diagnostic accuracy. Despite not having assessed study bias, we do acknowledge that it is a potential issue. Nonetheless, we have reported key characteristics and methodological details of the studies in our analysis, including any notable limitations or methodological considerations, to provide readers with a transparent understanding of the included literature. Note that no complex statistical methods were employed in this study as the research was descriptive in nature and focused on summarizing the usage patterns and clinical applications of 7T MRI in neurosurgery. **Table 1** summarizes the studies falling under each pathology discussed, their primary endpoints, and 7T MRI sequences used.

RESULTS

We initially identified a total of 219 records from the PubMed database within our defined period. We found no duplicate publications or any other reason to remove any manuscript before screening. All 219 articles were screened and out of them 125 were excluded as they did not meet our inclusion criteria. Finally, 94 reports were retrieved and 2 out of them were irrelevant to neurosurgery, and 7 were animal studies. This yielded a total of 85 studies that were included in our systematic review (**Figure 1**). We manually categorized the data in our database to obtain the number of publications available on PubMed for each of the neurosurgical procedures discussed in them as well as for each neurosurgically treated disease. According to our data, the most common neurosurgical procedures utilizing 7-T MRI were endoscopic neurosurgery, resective epilepsy surgery, and deep brain stimulation (DBS) surgery. **Figure 2** illustrates publications (p) per each procedure. The most treated pathologies were cerebrovascular diseases (10p), followed by epilepsy (8p), pituitary adenoma (7p), and gliomas (12p). However, it should be noted that under cerebrovascular diseases, a series of diseases were considered, such as amyloid angiopathy (1p), arteriovenous malformations (1p), stroke (2p), atherosclerosis (1p), intracranial aneurysms (4p), and intracerebral hemorrhage (ICH) (1p) (**Figure 3**). We also sorted the number of publications produced by each country. For this, only the institutional affiliation of the first author was considered. The countries with the highest absolute number of publications were the United States (27p) followed by the Netherlands (16p), South Korea (15p), Japan (13p), and Germany (7p) (**Figure 4**). In addition, we also present the number of 7T MRI facilities in each country (**Figure 5**). We also noticed that there has been a decline in the research output in the year 2018 and in 2022 (**Figure 6**). The experimental studies included were classified into comparison studies if 7T MRI was compared with lower field strengths, typically 1.5T and 3T, and into non-comparison studies (**Figure 7**).

DISCUSSION

Through the analysis of the included articles, several important observations and implications have emerged. The use of 7T MRI has demonstrated great potential in improving the characterization and understanding of various neurological and psychiatric conditions such as temporal lobe epilepsy (TLE), pituitary adenoma, unruptured intracranial aneurysms (UIAs), and movement disorders and has reported valuable insights into disease mechanisms, anatomical abnormalities, and functional alterations.

Epilepsy

7T MRI was proven to be a valuable non-invasive tool for evaluating subtle structural changes in the hippocampus of patients with TLE[10]. Specifically, the enhanced visualization of hippocampal internal architecture (HIA) can be achieved with 7T MRI. Notably, HIA asymmetry serves as a substantial predictor of the laterality of seizure onset in TLE patients, demonstrating comparable predictive efficacy to hippocampal volume asymmetry[11]. Similarly, significant advantages of using 7T MRI with post-processing techniques for identifying subtle focal cortical dysplasia lesions have been demonstrated (including increased detection rates) in patients with pharmaco-resistant epilepsy with non-lesional

Table 1 Summary of studies included in the review falling under each neurosurgically treated pathology

Pathology	Ref.	Aim of the study	Applied 7T MRI protocol
Epilepsy	Stefanits <i>et al</i> [10]	To correlate noninvasive, high-resolution, morphological 7T MRI of the hippocampus in temporal lobe epilepsy (TLE) patients with histopathological findings	T2-weighted (T2w) 2D fast spin echo (FSE) sequence, obtained in paracoronal, hippocampal plane perpendicular to the central sulcus (matrix, 688 × 688; field of view (FOV), 230 × 172.5; image resolution, 0.33 mm × 0.33 mm × 1.5 mm; slices, 25; parallel imaging, 2; repetition time (TR), 4500 milliseconds (ms); echo time (TE), 81 ms) with an acquisition time of 8 min 48 s
	Wang <i>et al</i> [12]	To assess the clinical value of <i>in vivo</i> structural 7T MRI and its post-processing in patients with pharmaco-resistant epilepsy who underwent presurgical evaluation and had a nonlesional 3T MRI scan	A standard epilepsy protocol was used with the following sequences on a 7T MRI scanner (Magnetom, Siemens, Erlangen, Germany) with a head-only circularly polarized transmit and 32-channel phased array receive coil (Nova Medical, Wilminuteston, MA): 3D T1-MP2RAGE: Sagittal acquisition, TR/TE = 6000/3 ms, TI1/TI2 = 700/2700 ms, flip angle (FA) 1/FA 2 = 4°/5°, 0.75 mm isotropic-voxel resolution, 208 slices, total acquisition time (TA) = 9 min 32 s; 2D T2-GRE (spoiled-gradient echo): Axial and oblique coronal acquisition, TR/TE = 2290/17.8 ms, FA = 23°, in-plane resolution = 0.38 mm × 0.38 mm, slice thickness = 1.5 mm, 60 slices, no gap, TA = 9 min 50 s; 2D FLAIR: Axial and oblique coronal acquisition, TR/TE = 9000/124 ms, TI = 2600 ms, in-plane resolution = 0.75 mm × 0.75 mm, slice thickness = 2 mm, 45 slices, 30% gap, TA = 3 min 2 s; 3D susceptibility weighted imaging (SWI) (included only for selected cases such as vascular malformation): TR/TE = 23/15 ms, FA = 20°, voxel size = 0.49 mm × 0.49 mm × 0.8 mm, 144 slices, TA = 8 min 16 s. Two dielectric calcium titanate pads with passive B1 shimming were used to improve the signal loss in the temporal lobes
	Rutland <i>et al</i> [15]	To perform hippocampal subfield-specific tractography and quantify connectivity of the subfields in MRI-negative patients. Abnormal connectivity of the hippocampal subfields may help inform seizure focus hypothesis and provide information to guide surgical intervention	Participants were scanned under an Institutional Review Board-approved protocol using a 7T whole body scanner. A SC72CD gradient coil was used (Gmax = 70 mT/m, max slew rate = 200 T/m/s), with a single channel transmit and 32 channel receive head coil. The MRI scan included a T1-weighted MP2RAGE sequence: TR = 6000 ms, TE = 3.62 ms, FA = 5°, FOV = 240 mm × 320 mm, slices = 240, 0.7 mm ³ isotropic resolution, scan time = 7 min 26 s. A coronal-oblique T2w turbo spin echo sequence was included: TR = 6900 ms, TE = 69 ms, FA = 150°, FOV = 202 mm × 202 mm, in-plane resolution 0.4 mm × 0.4 mm, slice thickness = 2 mm, slices = 40, time = 6 min 14 s. A high-angular-resolved diffusion-weighted imaging (HARDI) dMRI sequence was also performed with whole-brain coverage: <i>b</i> = 1200 s/mm ² , TR = 7200 ms, TE = 67.6 ms, 1.05 mm isotropic resolution, in-plane acceleration R = 3 (GRAPPA), reversed phase encoding in the AP and PA direction for paired acquisition in 68 directions, with a TA of 20 min
	Veersema <i>et al</i> [13]	To determine whether the use of 7T MRI in clinical practice leads to higher detection rates of focal cortical dysplasias in possible candidates for epilepsy surgery	7T MRI parameters are as follows: 3D T1w TFE: TE = 2.9 ms, TI = 1200 ms, TR = 9 ms, FA = 6°, resolution = 0.81 mm × 0.81 mm × 0.80 mm, matrix = 248 × 312 × 475, acquisition time = 9 min 34 s. 3D T2w turbo spin echo (TSE): TE = 302 ms, TR = 3200 ms, FA = 90°, resolution = 0.70 mm × 0.70 mm × 0.70 mm, matrix = 356 × 357 × 543, acquisition time = 10 min 24 s. 3D T2*w: TE = 27 ms, TR = 88 ms, FA = 24°, resolution = 0.50 mm × 0.50 mm × 0.50 mm, matrix = 480 × 381 × 600, acquisition time = 7 min 23 s; 3D MP-FLAIR: TE = 300 ms, TI = 2200 ms, TR = 8000 ms, FA = 90°, resolution = 0.80 mm × 0.82 mm × 1.00 mm, matrix = 312 × 304 × 380, acquisition time = 8 min 40 s. 3D WMS: TE = 2.0 ms, TI = 600 ms, TR = 6.73 ms, FA = 4.5°, resolution = 0.80 mm × 0.80 mm × 0.80 mm, matrix = 320 × 320 × 474, acquisition time = 8 min 42 s
	Zhang <i>et al</i> [11]	To compare the hippocampal internal architecture (HIA) between 3 and 7T MRI in patients with TLE	All patients underwent MRI scans with a 7 T scanner. Thirty-two channel head coils were used with both scanners. For the assessment of HIA, T2w images (T2WI) in the coronal plane located perpendicular to the long axis of the hippocampus were collected (7T T2WI-TSE): TR = 9640 ms, TE = 72 ms, resolution 0.3 mm × 0.3 mm × 2.0 mm, FA = 60°, TA = 11 min 26 s. 7T T1WI 3D-magnetization prepared rapid acquisition gradient echo (3D-MPRAGE): TR = 2200 ms, TE = 2.98 ms, resolution = 0.7 mm × 0.7 mm × 0.7 mm, FA = 8°, TA = 10 mi 16 s
	Sharma <i>et al</i> [14]	To quantitatively assess surgical outcomes in epilepsy patients who underwent scanning at 7T whose lesions were undetectable at conventional field strengths (1.5T/3T)	Unspecified
	van Lanen <i>et al</i> [16]	To assess whether 7T MRI increases the sensitivity to detect epileptogenic lesions	N/A (systematic review)
Pituitary adenoma	Yao <i>et al</i> [18]	To examine the utility of 7T MRI in predicting the tumor consistency of pituitary adenomas	High-resolution 7T TSE (0.4 mm × 0.4 mm × 2 mm), MP2-RAGE (0.75 mm isotropic), and TOF (0.26 mm × 0.26 mm × 0.4 mm) acquisitions on all patients
	Rutland <i>et al</i> [20]	To investigate microstructural damage caused by pituitary macroadenomas by performing probabilistic tractography of the optic tracts and	Participants were scanned under an Institutional Review Board-approved protocol using a 7T whole body scanner. A SC72CD gradient coil was used (Gmax = 70 mT/m, max slew rate = 200 T/m/s), with a single channel transmit and 32-channel receive head coil. Scanning included a T1-weighted

	radiations using 7T diffusion-weighted MRI (DWI). These imaging findings were correlated with neuro-ophthalmological results to assess the utility of ultra-high-field MRI for objective evaluation of damage to the anterior and posterior visual pathways	MP2RAGE sequence with the following parameters: TE (ms) = 5.1, TR (ms) = 6000, TI (ms) = 1050 (3000), FA = 5° (4°), FOV = 240 mm × 320 mm, slices = 240, resolution = 0.7 mm isotropic, scan time = 7 min 26 s. Quantitative T1-maps were derived from the MP2RAGE sequence. A coronal-oblique T2-TSE (TE = 69, TR = 6900, FA = 150°, FOV = 202 mm × 202 mm, in-plane resolution 0.4 mm × 0.4 mm, slice thickness = 2 mm, slices = 40, time = 6 min 14 s) and HARDI dMRI ($b = 1200 \text{ mm}^2/\text{sec}$, TE = 67.6, TR = 7200, resolution = 1.05 mm isotropic, in-plane acceleration R = 3 (GRAPPA), reversed phase encoding in AP and PA directions for paired acquisition in 68 directions, TA = 20) sequences were acquired
Rutland <i>et al</i> [21]	To leverage ultra-high-field 7T MRI to study the retinotopic organization of the primary visual cortex (V1) and correlate visual defects with cortical thinning in V1 to characterize consequences of pituitary adenomas on the posterior visual system	Participants were scanned using a 7T whole-body scanner (Magnetom, Siemens Healthineers). A SC72CD gradient coil was used (Gmax = 70 mT/m, maximum slew rate = 200 T/m/sec), with a single-channel transmit and 32-channel receive head coil (Nova Medical). Scanning included a T1-weighted MP2RAGE sequence with the following parameters: TE = 3.62 ms, TR 6000 ms, TI = 1050 ms (2 nd pulse 3000 ms), FA = 5° (2 nd pulse 4°), FOV = 224 mm × 168 mm, number of slices = 240, voxel size = 0.7 mm isotropic, and scan time = 8 min 8 s. Coronal oblique T2w turbo spin echo (TE = 59 ms, TR = 6000 ms, FA = 180°, FOV = 200 mm × 168 mm, in-plane voxel size = 0.4 mm × 0.4 mm, slice thickness = 2 mm, number of slices = 60, time = 6 min 50 s) and high-angular-resolved DWI ($b = 1200 \text{ mm}^2/\text{s}$, TE = 67.6 ms, TR = 7200 ms, voxel size = 1.05 mm isotropic, FA = 180°, number of slices = 66, in-plane acceleration R = 3, reversed-phase encoding in anteroposterior and posteroanterior directions for paired acquisition in 64 directions, TA = 18 min 38 s) sequences were prescribed. Dielectric pads and localized shimming methods were employed to reduce signal artifact at the skull base
Patel <i>et al</i> [22]	To describe the initial experience using ultra-high-field 7T MRI in patients with suspected Cushing’s disease and negative or equivocal imaging at conventional field strengths	Patients were scanned on a Siemens Terra 7T system using a Nova Medical 1Tx/32Rx head coil. Pre- and post- contrast (0.2 mL/kg gadoterate megluminutense) T1-weighted pituitary sequences included coronal and sagittal 2D TSE (TR = 960 ms, TE = 10 ms, voxel size = 0.2 mm × 0.2 mm × 2.0 mm), 3D SPACE (TR = 1200 ms, TE = 12 ms, variable FA, voxel size = 0.5 mm × 0.5 mm × 0.5 mm), and 3D MPRAGE (TR = 2300 ms, TE = 2.95 ms, FA = 7°, voxel size = 0.7 mm × 0.7 mm × 0.7 mm). Not all patients were scanned with all sequences due to changes in clinical protocol during the study period
Rutland <i>et al</i> [23]	To examine 7T DWI as a novel method of measuring the consistency of pituitary adenomas	Participants were scanned using a 7T whole-body scanner. A SC72CD gradient coil was used (Gmax = 70 mT/m, maximum slew rate = 200 T/m/s), with a single-channel transmit and 32-channel receive head coil. Scanning included a T1-weighted MP2RAGE sequence with the following parameters: TE = 3.62 ms, TR = 6000 ms, TI = 1050 ms (2 nd pulse 3000 ms), FA = 5° (2 nd pulse 4°), FOV = 224 mm × 168 mm, number of slices = 240, voxel size = 0.7 mm isotropic, and scan time = 8 min 8 s. Coronal oblique T2w turbo spin echo (TE = 59 ms, TR = 6000 ms, FA = 180°, FOV = 200 mm × 168 mm, in-plane voxel size = 0.4 mm × 0.4 mm, slice thickness = 2 mm, number of slices = 60, time = 6 min 50 s) and high-angular-resolved DWI ($b = 1200 \text{ mm}^2/\text{s}$, TE = 67.6 ms, TR = 7200 ms, voxel size = 1.05 mm isotropic, FA = 180°, number of slices = 66, in-plane acceleration R = 3, reversed-phase encoding in anteroposterior and posteroanterior directions for paired acquisition in 64 directions, TA = 18 min 38 s) sequences were prescribed. Dielectric pads and localized shimming methods were employed to reduce signal artifact at the skull base
Rutland <i>et al</i> [24]	To determine the efficacy of 7T MRI in identifying radiological markers for endocrine function	The Institutional Review Board-approved protocol employed a 7T whole-body MRI scanner (Magnetom, Siemens Healthcare, Erlangen, Germany) with a SC72CD gradient coil (Gmax = 70 mT/m, max slew rate = 200 T/m/s), and used a single channel transmit and 32-channel receive head coil (Nova Medical, Wilminutestgon, MA, United States). Sequences included a T1-weighted MP2RAGE[14] sequence: TE (ms) = 3.62, TR (ms) = 6000, TI (ms) = 1050/3000, FA = 5°/4°, FOV = 224 mm × 168 mm, slices = 240, resolution = 0.7 mm isotropic, scan time = 8 min 8 s. Quantitative T1-maps were derived from the MP2RAGE sequence. Coronal-oblique and axial T2-TSE (TE = 60 ms, TR = 6000 ms, FA = 180°, FOV = 200 mm × 168 mm, in-plane resolution 0.4 mm × 0.4 mm, slice thickness = 2 mm, slices = 60, time = 6 min 50 s) sequences were acquired. A T1-weighted MPRAGE sequence was also obtained (TE = 4.1 ms, TR = 3000 ms, TI = 1050 ms, FA = 7°, resolution = 0.7 mm isotropic, scan time = 7 min 40 s)
Rutland <i>et al</i> [17]	The study quantifies visualization of tumor features and adjacent skull base anatomy in a homogeneous cohort of pituitary adenoma patients comparing 7T MRI vs standard lower field MRI	Unspecified
Parkinson’s disease	Shamir <i>et al</i> [30] To validate the clinical application accuracy of the 7T-ML method by comparing it with identification of the subthalamic nucleus (STN) based on intraoperative microelectrode recordings	Unspecified
Lau <i>et al</i> [27]	To integrate ultra-high-field template	Patients were scanned on a 7T scanner (Agilent, Santa Clara, California,

	data into the clinical workflow to assist with target selection in deep brain stimulation (DBS) surgical planning	United States/Siemens, Erlangen, Germany) <i>via</i> a 24-channel transmit-receive head coil array constructed in-house with a receiver bandwidth of 50 kHz. A T1w MPRAGE sequence was acquired (TR = 8.1 ms, TE = 2.8 ms, inversion time (TI) = 650 ms, FA = 11°, matrix: 256 × 512, 230 slices, resolution = 0.59 mm × 0.43 mm × 0.75 mm). Then, a T2w turbo spin-echo 3D (TR = 3D sagittal, matrix: 260 × 366, 266 slices, resolution = 0.6 mm ³ , 4 averages) was acquired. High-resolution <i>in vivo</i> templates were created by performing group-wise linear and nonlinear registration of 12 normal subjects scanned on a human 7T imager with both T1w and T2w contrasts (available for download at http://www.nitrc.org/projects/deepbrain7t/) resulting in an unbiased group nonlinear T1w average and T2w averages at submillimeter resolution
La <i>et al</i> [26]	To measure hippocampal subfields <i>in vivo</i> using ultra-high-field 7T MRI and determine if these measures predict episodic memory impairment in PD during life	Participants were scanned with a 7T GE Healthcare Discovery MR950 MRI whole-body scanner (GE Healthcare, Waukesha, WI) using a 32-channel radiofrequency (RF) receive head coil contained within a quadrature transmit coil (Nova Medical, Inc., Wilminutestgon, MA). Sixteen oblique coronal images oriented perpendicular to the longitudinal axis of the hippocampus were acquired with a T2w FSE sequence: TE = 47 ms; TR = 5-8 s (cardiac gated); acquired voxel size was 0.22 mm × 0.22 mm × 1.5 mm with a slice gap of 0.5 mm, interpolated by zero filling to 0.166 mm × 0.166 mm × 1.5 mm
Lau <i>et al</i> [27]	To integrate ultra-high-field template data into the clinical workflow to assist with target selection in DBS surgical planning	Patients were scanned on a 7T imager (Agilent, Santa Clara, California, United States/Siemens, Erlangen, Germany) <i>via</i> a 24-channel transmit-receive head coil array constructed in-house with a receiver bandwidth of 50 kHz. A T1w MPRAGE sequence was acquired (TR = 8.1 ms, TE = 2.8 ms, TI = 650 ms, FA = 11°, matrix = 256 × 512, 230 slices, resolution = 0.59 mm × 0.43 mm × 0.75 mm). Then, a T2w turbo spin-echo 3D (TR 3D sagittal, matrix: 260 × 366, 266 slices, resolution = 0.6 mm ³ , 4 averages) was acquired. High-resolution <i>in vivo</i> templates were created by performing group-wise linear and nonlinear registration of 12 normal subjects scanned on a human 7T imager with both T1w and T2w contrasts (available for download at http://www.nitrc.org/projects/deepbrain7t/) resulting in an unbiased group nonlinear T1w average and T2w averages at submillimeter resolution
La <i>et al</i> [26]	To measure hippocampal subfields <i>in vivo</i> using ultra-high field 7T MRI and determine if these measures predict episodic memory impairment in PD during life	Participants were scanned with a 7T GE Healthcare Discovery MR950 MRI whole-body scanner (GE Healthcare, Waukesha, WI) using a 32-channel RF receive head coil contained within a quadrature transmit coil (Nova Medical, Inc., Wilminutestgon, MA). Sixteen oblique coronal images oriented perpendicular to the longitudinal axis of the hippocampus were acquired with a T2w FSE sequence: TE = 47 ms; TR = 5-8 s (cardiac gated); acquired voxel size was 0.22 mm × 0.22 mm × 1.5 mm with a slice gap of 0.5 mm, interpolated by zero filling to 0.166 mm × 0.166 mm × 1.5 mm
Oh <i>et al</i> [25]	To investigate patterns in gray matter changes in patients with Parkinson's disease by using an automated segmentation method with 7T MRI	High-resolution T1-weighted 7T MRI volumes of 24 hemispheres were acquired from 12 Parkinson's disease patients. Magnetic resonance images from all subjects were acquired using a 7T MRI system (Philips Healthcare, Cleveland, OH, United States) with a 32-channel head coil (Nova Medical, Wilminutestgon, MA, United States). Three-dimensional anatomical brain scans were acquired using a magnetization-prepared rapid-acquisition gradient-echo sequence-induced T1-weighted imaging system with the following settings: TR = 4.4 ms, TE = 2.2 ms, slice thickness = 0.5 mm, in-plane resolution = 0.5 mm × 0.5 mm, matrix size = 432 × 432, number of axial slices = 432, and TA = 5 min 57 s
Mathiopoulou <i>et al</i> [29]	To explore whether combining 7T T2w and DWI sequences allows for selective segmenting of the motor part of the STN and, thus, for possible optimization of DBS	7T T2w and DWI sequences were obtained, and probabilistic segmentation of motor, associative, and limbic STN segments was performed. The MR-sequences were acquired before surgery on a 3T Philips Ingenia scanner (Philips Healthcare, Best, The Netherlands): (1) 3D sagittal T1-weighted, gadolinium-enhanced (TR = 8.81 ms, TE = 4.03 ms, echo train length (ETL) = 242, FOV = 256 mm, slice thickness = 0.9 mm, scan time = 8 min); (2) 3D axial T2w (TR = 2500 ms, TE = 230 ms, ETL = 133, FOV = 250 mm, slice thickness = 1.1 mm, scan time = 3 min); and (3) DWI (TR = 8234 ms, TE = 96 ms, <i>b</i> = 1200 s/mm ² , 32 gradient directions, phase encoding anterior-posterior, no reverse encoding, FOV = 256 mm, slice thickness = 2.0 mm, scan time = 14 min). The following MR sequences were acquired on a 7T Achieva system (Philips Healthcare) using a 32 channel receive coil (Nova Medical, Wilminutestgon, MA): (1) 3D sagittal T2w with Turbo spin echo imaging (TR = 3000 ms, TE = 324 ms, ETL = 182, FOV = 250 × 250 × 190, FA = 100°, voxel size = 0.7 mm isotropic, scan duration = 7 min); and (2) DWI (TR = 6084 ms, TE = 70 ms, ETL = 59, <i>b</i> = 1000 s/mm ² , 32 directions, FOV = 140 × 177 × 110, voxel size = 1.4 mm × 1.4 mm in-plane, slice thickness = 1.5 mm, scan duration = 13 min)
Isaacs <i>et al</i> [28]	The study aimed to test whether optimized 7T imaging protocols result in less variable targeting of the STN for DBS compared to clinically utilized 3T images	The 7T scan was acquired with a Siemens Magnetom scanner using a 32-channel head coil at the Scannexus Centre for Neuroimaging in Maastricht. Whole brain T1w 3D images were obtained with an adapted version of the multi echo MP2RAGE (magnetization-prepared rapid gradient echo multi-echo) sequence with 0.8 mm isotropic voxel sizes and the following parameters: 208 slices, TR = 6000 ms, TE 1/2 = (2.74 ms/8.71 ms), TI 1/2 = (750 ms/29000 ms), FA 1/2 = (4°/6°), BW 1/2 = (350 Hz/Px/150 Hz/Px), ES = 13.6 ms, interleaved and single shot multi slice mode and interleaved, sagittal orientation acquisition in the anterior-posterior direction, phase partial Fourier 6/8, parallel acquisition with GRAPPA and acceleration factor

		of 3 and TA of 10 min 56 s. Where possible, dielectric pads were placed between the side of the participants head and the receiver coil to reduce B1 inhomogeneity artefacts. The T2w 3D scan was acquired with a partial volume gradient echo ASPIRE (multi-channel phase data from multi-echo acquisitions) sequence covering the subcortex with 0.5 mm isotropic voxel sizes and the following parameters: 90 slices, 16.7% slice oversampling, TR = 33 ms, TE 1-4 =(2.49 ms, 6.75 ms, 13.50 ms, 20.75 ms), FA =12°, BW 1-4 = (300 Hz/px, 300 Hz/px, 200 Hz/px, 100 Hz/px), interleaved multi slice mode, sagittal orientation acquisition in the anterior-posterior direction, slice partial Fourier 7/8, parallel acquisition with GRAPPA and acceleration factor of 2 and TA 7 min 42 s
Cerebrovascular diseases	Van Tuijl <i>et al</i> [34]	To gain insight into hemodynamic imaging markers of the CoW for unruptured intracranial aneurysm (UIA) development by comparing these outcomes to the corresponding contralateral artery without an UIA using 4D flow MRI
	Wrede <i>et al</i> [32]	To prospectively evaluate non-contrast-enhanced 7T magnetic resonance angiography (MRA) for delineation of UIAs
	Uwano <i>et al</i> [36]	To investigate whether OEF maps generated by magnetic resonance quantitative susceptibility mapping (QSM) at 7 T enabled detection of OEF changes when compared with those obtained with PET
	Uwano <i>et al</i> [37]	To examine whether whole-brain MRA at 7 T could non-invasively detect impaired CVR in patients with chronic cerebral ischemia by demonstrating the leptomeningeal collaterals
	Noureddine <i>et al</i> [35]	To evaluate RF-induced tissue heating around aneurysm clips during a 7T head MR examination and determine the decoupling distance between multiple implanted clips
	Millesi <i>et al</i> [33]	To delineate the wall of intracranial aneurysms to identify weak areas prone to rupture
	Koemans <i>et al</i> [38]	To investigate whether a striped occipital cortex and intragyral hemorrhage, two markers recently detected on ultra-high-field 7T MRI in hereditary cerebral amyloid angiopathy (CAA), also occur in sporadic CAA (sCAA) or non-sCAA
		Participants underwent 7T MRI (Philips Healthcare, Best, The Netherlands) using a volume transmit and 32-channel receive coil (Nova Medical, Houston, United States). For this study, the Amsterdam Medical Center “PROspective Undersampling in multiple Dimensions” software patch was used, which enables a pseudospiral ky/kz-plane acquisition scheme designed for incoherent undersampling with a variable sampling density. Time-resolved 3D phase-contrast velocity maps (4D flow scan) over the cardiac cycle were acquired with the following parameters: Angulated coronal FOV 250 (feet-head) × 190 (right-left) × 20 (anterior-posterior) mm ³ , acquired resolution of 0.7 mm × 0.7 mm × 0.7 mm, repetition time/TE = 6.4/2.2, velocity encoding sensitivity 100 cm/s, FA = 15°, nominal acceleration factor 7, and 12 reconstructed cardiac phases (<i>i.e.</i> , reconstructed temporal resolution 83 ms for a heart rate of 60 bpm). Retrospective gating used a peripheral pulse unit for heartbeat detection. Acquisition duration was 10 min
		Both TOF MRA (time-of-flight magnetic resonance angiography) and non-contrast-enhanced MPRAGE were used at 7 T. 32-channel Tx/Rx RF head coil, maximum amplitude of 45 mT/m, slew rate of 200 mT/m/ms. Prior to acquisition of diagnostic sequences, B0-shimming was performed using a vendor provided gradient echo sequence and algorithm. For B1-field mapping and local FA optimization, a vendor-provided spin-echo type sequence was used; after a slice selective excitation, two refocusing pulses generate a spin-echo and a stimulated echo
		A 7T MRI scanner with quadrature transmission and 32-channel receive head coils was used. Source data of QSM were obtained using a 3-dimensional spoiled gradient recalled acquisition technique with the following scanning parameters: TR, 30 ms; TE, 15 ms; FA, 20°; FOV, 256 mm; acquisition matrix size, 512 × 256; slice thickness, 2 mm; number of slices, 160; reconstruction voxel size after zero-fill interpolation, 0.5 mm ³ ; and scan time, 3 min 25 s. The sections were set in the orthogonal axial plane from the level of the superior cerebellar peduncle to high convexity. Magnitude as well as real/imaginary phase images were regenerated from this acquisition. Structural images including T2WI and magnetic resonance angiography were also obtained
		MRI examinations were performed with a 7T MRI scanner with a quadrature transmission and 32-channel receive head coil system. Whole-brain single-slab 3D time-of-flight MRA was performed using the following scanning parameters: TR, 12 ms; TE, 2.8 ms; FA, 12°; FOV, 22 cm; matrix size, 512 × 384; slice thickness, 0.5 mm (zero-fill interpolation); partition, 332; tilted optimized non-saturated excitation; number of excitations, 1; and acquisition time, 10 min 32 s. Subsequently, axial and coronal maximum intensity projection images were generated after skull stripping with SPM8 software. SPECT studies were performed using two scanners and iodine 123 N-isopropyl-p-iodoamphetaminutese (¹²³ I-IMP) at a resting state with the ACZ challenge, as described previously. The voxel size was 2.0 mm × 2.0 mm × 5.0 mm in scanner 1 and 1.72 mm × 1.72 mm × 1.72 mm in scanner 2. The cerebral blood flow was quantified using the ¹²³ I-IMP autoradiography method. Angiography and SPECT studies were performed within 10 d before/after the MRI examination
		Unspecified
		Patients underwent ultra-high-field MRI that was performed in a whole-body 7T MRI unit (Siemens Healthcare) with a gradient strength of 40 mT/m using a 32-channel transmit/receive coil. The MRI sequence performed for this study was a nonenhanced MPRAGE sequence (TR/TE 3850/3.84 ms, isotropic voxel size 0.5 mm)
		T2-weighted images were obtained. MRI markers associated with small vessel disease were scored according to the Standards for Reporting Vascular changes on neuroimaging criteria

		intracerebral hemorrhage (ICH)	
	Dammann <i>et al</i> [40]	To compare cerebral cavernous malformations-associated cerebral venous angioarchitecture between sporadic and familial cases using 7T MRI	In all patients, SWI was performed at 7 T (Magnetom 7T; Siemens Healthcare). Susceptibility-weighted imaging sequences were established in previous work. The whole-body ultra-high-field MR system was equipped with a single-channel transmitter/32-channel receiver head coil (Nova Medical), and a gradient system capable of 45 mT/m maximum amplitude and a slew rate of 220 mT/m/ms. The SWI parameters were as follows: TE 15 ms, TR 27 ms, FA 14°, in-plane resolution (R) 250 mm × 250 mm, slice thickness 1.5 mm, and bandwidth 140 Hz/pixel. The SWI data were processed to phase, magnitude, susceptibility, and minimum intensity projection images. In addition, anatomical T1w (TR 2500 ms, TE 1.4 ms, FA 6°, 0.7 mm isotropic), T2w (TR 6000 ms, TE 99 ms, FA 29°, ST 3 mm, R 0.5 mm ²), and time-of-flight angiography (TR 20 ms, TE 4.3 ms, FA 20°, ST 0.4 mm, R 0.2 mm ²) sequences were acquired
	Harteveld <i>et al</i> [31]	To compare 3T and 7T MRI in visualizing both the intracranial arterial vessel wall and vessel wall lesions	For 7T MRI, a whole-body system (Philips Healthcare, Cleveland, OH, United States) was used with a 32-channel receive coil and volume transmit/receive coil for transmission (Nova Medical, Wilminuteston, MA, United States). The imaging protocol included a 3D whole-brain T1-weighted magnetisation-prepared inversion recovery turbo spin echo intracranial vessel wall sequence
	Jolink <i>et al</i> [39]	To assess presence and extent of contrast agent leakage distant from the hematoma as a marker of BBB disruption in patients with spontaneous ICH	7T MRI (Philips, Best, The Netherlands) scans were acquired with a standardized protocol; 3D T2w TR/equivalent TE = 3158/60 ms; voxel size acquired: 0.70 mm × 0.70 mm × 0.70 mm, reconstructed: 0.35 × mm × 0.35 mm × 0.35 mm), 3D T1-weighted (TR/TE 4.8/2.2 ms; voxel size acquired: 1.00 mm × 1.01 mm × 1.00 mm, reconstructed: 0.66 mm × 0.66 mm × 0.50 mm), dual echo 3D T2w (TR/first TE/ second TE 20/6.9/15.8 ms; voxel size acquired: 0.50 mm × 0.50 mm × 0.70 mm, reconstructed: 0.39 mm × 0.39 mm × 0.35 mm), and 3D FLAIR images were acquired (TR/TE/TI 8000/300/2325 ms; voxel size acquired: 0.80 mm × 0.82 mm × 0.80 mm, reconstructed: 0.49 mm × 0.49 mm × 0.40 mm). A gadolinium-containing contrast agent was administered in a single intravenous injection of 0.1 mL Gadovist/kg body weight with a maximum of 10 mL Gadovist or 0.2 mL Dotarem/kg body weight with a maximum of 30 mL Dotarem. Postgadolinium FLAIR images were acquired at least 10 min after contrast injection
TN	Moon <i>et al</i> [42]	To determine the central causal mechanisms of TN and the surrounding brain structure in healthy controls (HCs) and patients with TN using 7T MRI	Subjects underwent MRI scans using a 7T MR system (Philips Healthcare, Cleveland, OH, United States) with a 32-channel phased-array head coil (Nova Medical, Wilminuteston, MA, United States). 3D anatomical brain scans were acquired using magnetization prepared rapid acquisition gradient echo (MP-RAGE) sequence-induced T1w imaging with the following settings: TR = 4.6 ms, TE = 2.3 ms, FA = 110°, slice thickness = 0.5 mm, in-plane resolution = 0.5 mm × 0.5 mm, matrix size = 488 × 396, number of axial slices = 320, and TA = 5 min 53 s
	Moon <i>et al</i> [41]	To investigate DTI parameters and the feasibility of DTI criteria for diagnosing TN	Imaging scans were acquired with a whole-body 7T MR system (Philips Healthcare, Cleveland, OH, United States) with a 16-channel receive head coil (Nova Medical, Wilminuteston, MA, United States) and volume transmit. Standard scanning protocols included T1, 3D T2-VISTA, and DTI were used to assess microstructure and pathology changes. MRI sequences were: 7T T1 anatomical images (TR = 4.6 ms, TE = 2.3 ms, FA = 110°, thickness = 0.5 mm, voxel size 0.5 × 0.5, matrix size 488 × 396); three-dimensional T2-VISTA images to confirm offending vessels (TR = 2031 ms, TE = 303 ms, FA = 90°, voxel size 0.5 × 0.5, matrix size 360 × 360); and DTI (TR = 5606 ms, TE = 63 ms, FA = 90°, thickness = 1.5 mm, voxel size 1.5 × 1.8, matrix size 140 × 107, and $b = 700 \text{ s/mm}^2$)
Traumatic head injury	Hütter <i>et al</i> [43]	To evaluate the possible prognostic benefits of 7T SWI of traumatic cerebral microbleeds over 3T SWI to predict the acute clinical state and subjective impairments, including health-related quality of life, after closed head injury	The MRI examinations and their methods have been described in detail in an earlier publication. The 7T SWI acquisition time was about 13 min. UHF MR examinations were performed on a 7 T whole-body research system (Magnetom 7T, Siemens Healthcare, Germany) used in combination with 32-channel radiofrequency head coils
MS	Chou <i>et al</i> [44]	To evaluate the sensitivity of 7T magnetization-transfer-weighted (MTw) images in the detection of white matter lesions compared with 3T FLAIR	Participants underwent MRI in the Sir Peter Mansfield Imaging Centre using a 7T Philips Achieva scanner (Philips Medical Systems, Best, the Netherlands). The scanning protocols included 3D T1-weighted MP-RAGE imaging to assist with coregistering 3T 2D-FLAIR and 7T 3D-MTw images. Acquisition parameters at 7 T were TE = 3.2 ms; TR = 6.9 ms; TI = 800 ms; FA of the TFE readout pulse = 80°; TFE factor = 240; shot-to-shot interval = 8 s; spatial resolution = 1.25 mm × 1.25 mm × 1.25 mm; FOV = 200 mm × 200 mm × 72.5 mm; reconstruction matrix = 160 × 160 × 58 mm ³ ; and TA = 2 min
	Choksi <i>et al</i> [45]	The study aimed to identify white matter tracts associated with the severity of neurogenic lower urinary tract dysfunction in women with MS	7T DTI images were acquired (matrix 158 × 158, slice thickness 1.4 mm, FOV 220 cm × 220 cm ² , 64 directions, $b = 1000 \text{ s/mm}^2$, total scan time 12 min and 14 s) on a 7T Siemens MAGNETOM Terra MRI scanner with a 32-channel single transmit head coil (3T Siemens MAGNETOM Vida MRI scanner was used in two subjects with contraindications for 7T scanner)
	Beck <i>et al</i> [46]	The study aimed to characterize	The 7T brain scans included axial 3D MP2RAGE (0.5 mm isometric, acquired

		cortical lesions by 7T T2-/T1-weighted MRI, and to determine relationship with other MS pathology and contribution to disability	four times per scan session), sagittal 3D segmented T2w echo-planar imaging (EPI; 0.5 mm isometric, acquired in two partially overlapping volumes for full brain coverage), and axial 2D T2w multi-echo GRE (0.5 mm isometric, acquired in three partially overlapping volumes for near full supratentorial brain coverage). MP2RAGE data were processed into uniform denoised images (hereafter, T1w MP2RAGE) and T1 maps using manufacturer-provided software
Glioma	Prener <i>et al</i> [48]	To evaluate the potential clinical implication of the use of single-voxel magnetic resonance spectroscopy (MRS) at 7 T to assess metabolic information on lesions in a pilot cohort of patients with grades II and III gliomas	Seven patients and seven HCs were scanned using the semi-localization by adiabatic-selective refocusing sequence on a Philips Achieva 7T system equipped with a two-channel volume transmit head coil with a 32-channel receiver array. A 3D FLAIR sampled in the sagittal direction was acquired with the following parameters: TR = 7342 ms; TE = 348 ms; TI = 2200 ms; acquisition voxel size = 0.7 mm × 0.7 mm × 1.4 mm; FA = 75°; refocusing acquisition voxel size = 0.7 mm × 0.7 mm × 1.4 mm; refocusing angle = 30°; scan duration = 6 min 44 s. In this study, the scan was used for MRS voxel placement, although it was also acquired as part of an additional structural imaging research protocol
	Yuan <i>et al</i> [49]	The goal of the study was to explore the capability on preoperatively identifying IDH status of combining a convolutional neural network and a novel imaging modality, ultra-high-field 7T chemical exchange saturation transfer (CEST) imaging	All patients underwent MRI scans within a week prior to surgery. CEST MRI was performed on a 7T MRI scanner (MAGNETOM Terra; Siemens Healthineers, Erlangen, Germany) with a prototype-developed snapshot-CEST sequence based on a 3D gradient spoiled GRE readout with a single-channel transmit/32-channel receive head coil (Nova Medical, Wilminuteston, MA, United States). The snapshot-CEST sequence parameters were TR = 3.4 ms, TE = 1.59 ms, FA = 6°, resolution = 1.6 mm × 1.6 mm × 5 mm, and GRAPPA acceleration factor = 3 with amplitudes B1 = 0.6, 0.75, and 0.9 mT. Z-spectra were sampled unevenly by 56 frequency offsets between -300 ppm and +300 ppm. The Z-spectrum data were corrected for both B0 and B1 inhomogeneities using the WASABI method and were fit pixelwise by a five-pool Lorentzian model (water, amide, aminutese, NOE, and MT) using the Levenberg-Marquardt algorithm. For CEST data co-registration, high-resolution T1 MP2RAGE (TR = 3800 ms, TI1 = 800 ms, TI2 = 2700 ms, TE = 2.29 ms, FA = 7°, and resolution = 0.7 mm isotropic) and 3D T2-SPACE (TR = 4000 ms, TE = 118 ms, and resolution = 0.67 mm isotropic) were acquired at 7 T. Routine-clinical-sequence, contrast-enhanced T1-weighted images (TR = 6.49 ms, TE = 2.9ms, FA = 8°, spatial resolution = 0.833 mm × 0.833 mm × 1 mm), were acquired at 3 T on an Ingenia MRI scanner (Koninklijke Philips N.V., Netherlands)
	Prener <i>et al</i> [55]	The aim of this study was to explore the difference in gross tumor volume of DLGGs delineated from 7T and 3T MRI scans	The 7T MR system was an actively shielded Philips Achieva 7T MR system (Philips Healthcare, Best, The Netherlands). Scanning protocol settings for 7T were as follows: 3D TSE-T2 (0.7 mm × 0.7 mm × 0.7 mm) (TE = 60) and 3D FLAIR (0.7 mm × 0.7 mm × 0.7 mm) (TE = 347). Scan time for 7T was as follows: 3D TSE-T2 was 10 min 30 s and 3DFLAIR was 7 min 30 s
	Weng <i>et al</i> [56]	The underlying prospective study aimed to compare SLOW-EPSI to established techniques at 7 T and 3 T for IDH-mutation status determination	The applied sequences were MEGA-SVS, MEGA-CSI, SLOW-EPSI, MRSI, 3D-T1-MPRAGE, 3D-T2-SPACE, and TOF-angiography. Measurements were performed on a MAGNETOM-Terra 7T MR scanner in clinical mode using a Nova 1Tx32Rx head coil. At 7 T, MEGA-SVS: TE = 75 ms, TR = 2500 ms, VOI = 30 × 30 × 30 mm ³ , averages = 64, and TA = 5 min 42 s. MEGA-CSI: TE = 75 ms, TR = 2900 ms, VOI = 70 mm × 70 mm × 20 mm, FOV = 200 × 200 × 20 mm ³ (12 × 12 matrix), averages = 1, and TA = 8 min 10 s
	Yuan <i>et al</i> [50]	The study aimed to evaluate the diagnostic accuracy of combining CEST imaging and MRS for predicting glioma infiltration	CEST acquisitions were performed at 7 T on an MRI scanner (MAGNETOM Terra, Siemens Healthineers, Erlangen, Germany). A prototype snapshot-CEST (optimized single-shot GRE sequence with rectangular spiral reordering) was applied (TR = 3.4 ms, TE = 1.59 ms, FA = 6°, bandwidth = 660 Hz/pixel, grappa = 3, resolution = 1.6 mm × 1.6 mm × 5 mm)
	Voormolen <i>et al</i> [47]	To investigate intra- and extracranial distortions in 7T MRI scans of skull-base meningioma	The 7T scan parameters of the 3-dimensional sagittal magnetization-prepared turbo field echo sequence are as follows: FOV 256 mm × 256 mm × 200 mm (matrix 256 × 256 × 200), TI 1200 ms, ETL 256 mm ³ , readout 9 ms, TE 2.0 ms, bandwidth 506.3 Hz/pixel, and FA 8°. Total imaging time: 9 min and 36 s. Prior to the acquisition at 7 T, a B0 field map was acquired
Psychiatric disease	Van den Boom <i>et al</i> [51]	To investigate whether people can learn to dynamically control activity of the DLPFC, a region that has been shown to be important for working memory function and has been associated with various psychiatric disorders	fMRI performed using a 7T Philips Achieva system, with a 32-channel headcoil. Functional data recorded using an EPI sequence (TR/TE: 2.0 s/25 ms, FA: 70°, 39 axial slices, acquisition matrix 112 × 112, slice thickness 2.2 mm no gap, 2.19 mm in plane resolution). A T1-weighted image was acquired for anatomy (TR/TE: 7/2.76 ms; FA: 8°; resolution 0.98 mm × 0.98 mm × 1.0 mm)
	Morris <i>et al</i> [52]	To use ultra-high-field 7T MT MRI to localize the LC in humans with and without pathological anxiety, with 0.4 mm × 0.4 mm × 0.5 mm resolution in a feasible scan time. In addition, to apply a computational, data-driven LC localization and segmentation algorithm to delineate LC for all	Participants were scanned using a 7T MRI scanner (Magnetom, Siemens, Erlangen, Germany) with a 32-channel head coil at the Leon and Norma Hess Center for Science and Medicine, ISMMS. Most subjects tolerated the MRI environment well. On entering the scanner, several subjects reported dizziness lasting 1-2 min, which they found tolerable. Structural T1-weighted dual-inversion magnetization prepared gradient echo (MP2RAGE) anatomical images were acquired first (TR = 4500 ms, TE = 3.37 ms, TI1 = 1000s and 3200 ms, FA = 4° and 5°, iPAT acceleration factor = 3, bandwidth =

	participants. The relationships between LC volume and trans-diagnostic measures of pathological anxiety and attentional control were subsequently examined in a dimensional approach based on the RDoC initiative, reflecting evidence that pathological anxiety is a trans-diagnostic construct	130 Hz/pixel, 0.7 mm isotropic resolution, whole brain coverage). Second, MT-MRI data were acquired with a 3-D segmented GRE readout (turbo-FLASH; TFL) preceded by a train of 20 MT pulses of amplitude with 190 V transmit, and 7-min run time
Zoon <i>et al</i> [53]	The study aimed to explore the connection between the location of active DBS contact points within STN subdivisions and the development of apathy in Parkinson's disease patients undergoing DBS	22 PD patients that underwent STN DBS between January 2019 and February 2020 were divided in an apathy and non-apaty group using the change in the Starkstein Apathy Scale after 6 mo of DBS. For both groups the location of DBS electrodes was determined based on 7T MRI subthalamic network analysis, enabling visualization of the subdivisions and their projections relative to the active contact point. MDS-UPDRS III scores were included to evaluate DBS effect
Alper <i>et al</i> [54]	The objective of this study was to assess volumetric differences in hippocampal subfields between MDD patients globally and HCs as well as between a subset of treatment-resistant depression patients and HCs using automatic segmentation of hippocampal subfields software and ultra-high-field MRI	Thirty-five MDD patients and 28 HCs underwent imaging using 7T MRI. A 32-channel Nova Medical head coil was used to acquire brain images for segmentation. The 90-min imaging protocol included MP2RAGE (TR 6000 ms, TI1 1050 ms, TI2 3000 ms, TE 5.06 ms, voxel 0.70 mm × 0.70 mm × 0.70 mm) and T2 TSE (TR 9000 ms, TE 69 ms, voxel 0.45 mm × 0.45 mm × 2 mm) scans acquired at a coronal oblique oriented perpendicular to the long axis of the hippocampus
Essential tremor	Purrer <i>et al</i> [57] The aim of the study was to analyze the localization of individual lesions with respect to the VIM and the cerebello-thalamic tract	MRI images were acquired using a 7T scanner (Siemens Magnetom, Erlangen, Germany) with a 32-channel head coil. A fast MP-RAGE sequence was utilized to acquire the WMn contrast with a high isotropic resolution of 0.7 mm. The sequence parameters were TR/TI = 4000/670 ms, matrix = 364 mm × 310 mm × 240 mm, parallel imaging acceleration factor = 3, and acquisition time = 10 min 24 s. In addition, a T1-weighted MP-RAGE was acquired with the same coverage and resolution, but TR/TI = 2500/1100 ms, FA = 7°, PA = 2, TA = 5 min 33 s

TOF: Time-of-flight; CoW: Circle of Willis; CVR: Cerebrovascular reactivity; FLAIR: Fluid-attenuated inversion recovery; dMRI: Diffusion Magnetic Resonance Imaging; OEF: Oxygen extraction fraction; ACZ: Acetazolamide; DTI: Diffusion tensor imaging; TN: Trigeminal neuralgia; MS: Multiple sclerosis; GRE: Gradient-recalled echo; MRI: Magnetic resonance imaging.

3T MRI scans[12]. This improved detection rate may play a role in identifying suitable candidates for surgery and facilitating the complete resection of epileptogenic lesions, potentially leading to postoperative freedom from seizures [13]. Nevertheless, studies based on larger cohorts are needed to confirm its predictive value in preoperative evaluation. A quantitative assessment of surgical outcomes in patients scanned at 7 T, whose lesions were undetectable at conventional field strengths, further emphasizes the clinical impact of 7T imaging, elucidating the practical implications of employing 7T MRI in improving surgical outcomes for patients with initial elusive lesions[14]. Among 16 patients studied, 7 exhibited clear epileptogenic potential on 7T imaging, while 9 had findings of a less definite nature. Remarkably, 15 out of 16 patients achieved Engel I, II, or III outcomes, denoting substantial improvement. Notably, those with definite lesions on 7T imaging had a higher rate of achieving Engel I surgical outcomes (57.1%) compared to those with less definite lesion status (33.3%). This suggests that patients initially diagnosed as MRI-negative on lower field strength scans but with clear radiological findings on 7T, corresponding to the suspected seizure onset zone, may benefit significantly from surgical intervention[14]. A recent study suggested that employing high-resolution diffusion MRI-based tractography of hippocampal subfields enabled the quantification of connectivity within the subfields in MRI-negative patients and identified abnormal connectivity patterns. This information holds promise in refining the understanding of the seizure focus hypothesis, thereby aiding in the formulation of more informed surgical strategies [15]. These findings indicate that distinct connectivity patterns exist among hippocampal subfields in different types of epilepsy, holding potential significance for informing hypotheses regarding seizure focus and guiding surgical interventions, particularly in patients with MRI-negative findings[15]. Prospective studies involving larger cohorts of epilepsy patients, consistent scan and sequence protocols, and advancements in post-processing technology are crucial for further exploration. Beyond technical enhancements, establishing a better correlation between imaging features and clinical semiology, histopathology, and overall clinical outcomes is equally important for the continued refinement of ultra-high-field MRI in epilepsy diagnosis and treatment[16].

Pituitary adenoma

When compared to standard-of-care clinical imaging at 3 T or 1.5 T, no significant difference in the visualization of pituitary adenoma features has been observed at 7 T. However, cranial nerves III, IV, and VI, ophthalmic arteries, and posterior communicating arteries were more effectively detected with 7T MRI than with lower field strength scans, and this superiority extended to comparisons with both 1.5 T and 3 T[17]. Furthermore, employing a granular, voxel-based analysis has been shown to maximize the potential of 7T imaging resolution and along with high-resolution apparent diffusion coefficient maps in 7T diffusion-weighted imaging (DWI), it represents a sensitive measure of pituitary adenoma consistency contributing to a more accurate characterization of their internal composition, providing valuable information for preoperative planning and predicting surgical outcomes[18,19]. In addition, 7T DWI has been succe-

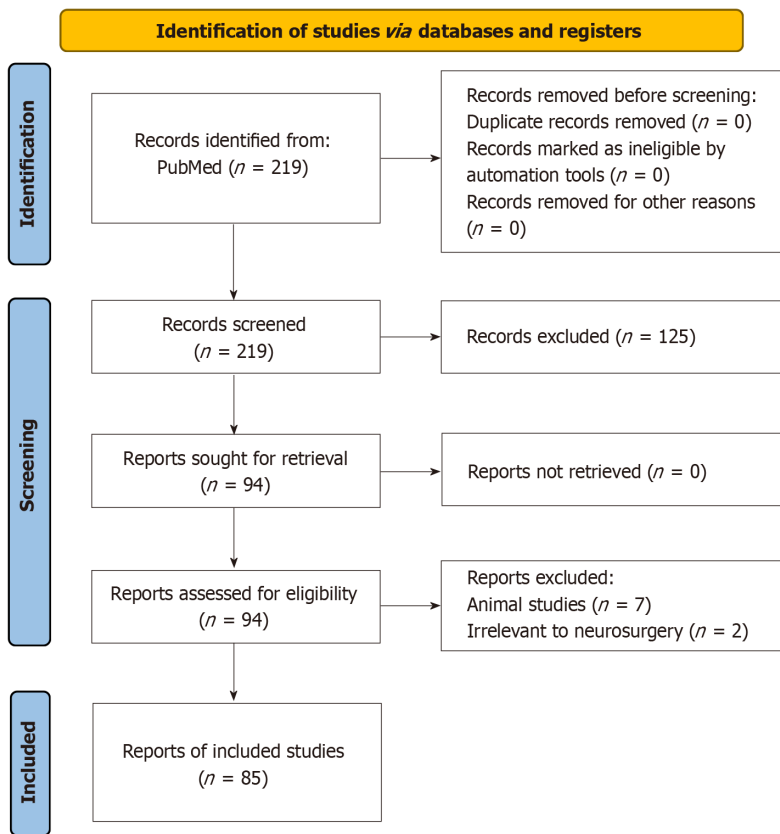


Figure 1 PRISMA flowchart depicting selection of studies for our systematic review.

successfully applied for probabilistic tractography of the optic tracts and radiations in patients with pituitary macroadenomas. The correlation between imaging findings and neuro-ophthalmological results offers an objective evaluation of damage to the anterior and posterior visual pathways, enhancing our ability to assess the impact of pituitary adenomas on visual function[20]. Quantifying secondary neuronal damage from adenomas through diffusion characteristics seen in 7T DWI enables preoperative characterization of visual pathway damage and facilitates prediction regarding recoverability of vision for patients experiencing chiasmatic compression[20,21]. The initial experience with ultra-high-field 7T MRI in patients with suspected Cushing’s disease and negative or equivocal imaging at conventional field strengths represents a critical aspect in detecting subtle abnormalities and may offer a valuable diagnostic tool in cases where conventional imaging falls short, contributing to improved diagnostic accuracy and patient management[22]. A recent study showed that 7T MRI facilitated the identification of previously unnoticed focal pituitary hypoenhancement in 90% (9/10) of patients. Remarkably, 7 out of these 9 cases corresponded histologically to corticotroph adenomas, indicating a significant adjunctive role for ultra-high-field MRI in the non-invasive clinical assessment of suspected Cushing's disease[22]. The use of 7T MRI proves valuable in identifying markers of endocrine function in patients with pituitary adenomas. The corrected T2 signal intensity (SI) of the tumor emerges as a sensitive predictor of hormonal secretion, offering utility in the diagnostic workup for pituitary adenoma. A study showed that hormone-secreting tumors exhibit higher T2-weighted SI and tumors associated with preoperative hypopituitarism display greater stalk curvature angles[23,24].

Parkinson's disease

Recently, Oh *et al*[25] employed high-resolution T1-weighted 7T MRI to investigate gray matter changes in Parkinson's disease (PD). The examination involved 12 patients and age- and sex-matched controls, with subgroup analysis based on the presence of axial motor symptoms. Utilizing an automated segmentation method, the study revealed distinctive patterns in cortical and subcortical volume alterations. PD patients exhibited global cortical atrophy, notably in the prefrontal area, including the rostral middle frontal, superior frontal, inferior parietal lobule, medial orbitofrontal, and rostral anterior cingulate regions while subcortical volume atrophy was observed in limbic/paralimbic areas such as the fusiform, hippocampus, and amygdala[25]. A recent study delved into the *in vivo* measurement of hippocampal subfields using ultra-high-field 7T MRI to understand whether these measures predict episodic memory impairment in PD. The findings provided insights into how structural changes within the hippocampus, such as the thickness of hippocampal CA1-SP subfield estimated by 7T MRI, could offer potential markers for early diagnosis and intervention of episodic memory impairment[26]. In the realm of advanced PD treatment, DBS targeting the subthalamic nucleus (STN) has proven highly effective. By assisting with target selection, 7T MRI has been shown to be capable of providing a more detailed and accurate representation of the brain anatomy, potentially improving the precision and efficacy of DBS procedures in PD patients[27]. Isaacs *et al*[28] conducted a study where three DBS-experienced neurosurgeons assessed optimal STN DBS target sites in three repetitions of 3T-T2, 7T-T2*, 7T-R2*, and 7T quantitative susceptibility mapping

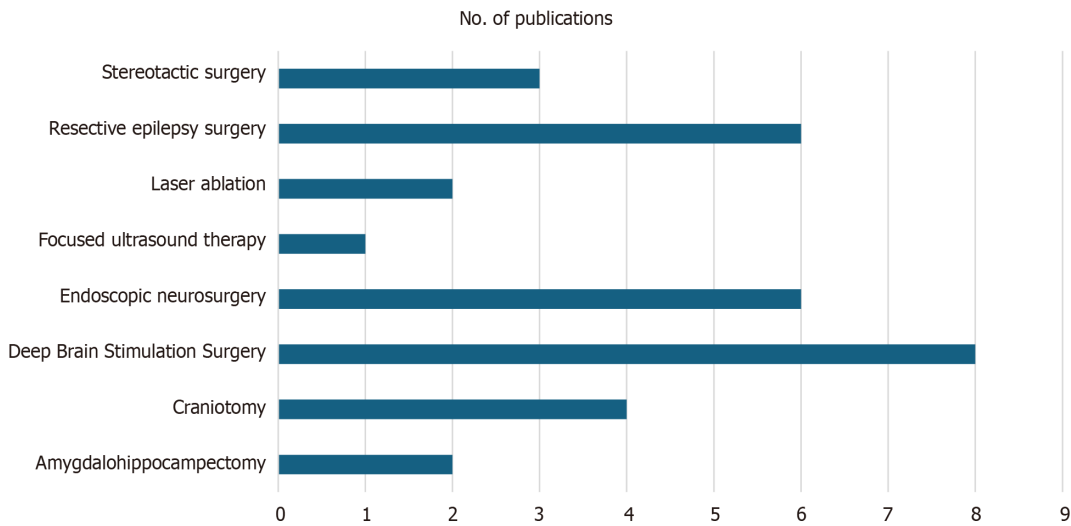


Figure 2 Chart showing number of 7T publications per neurosurgical procedure.

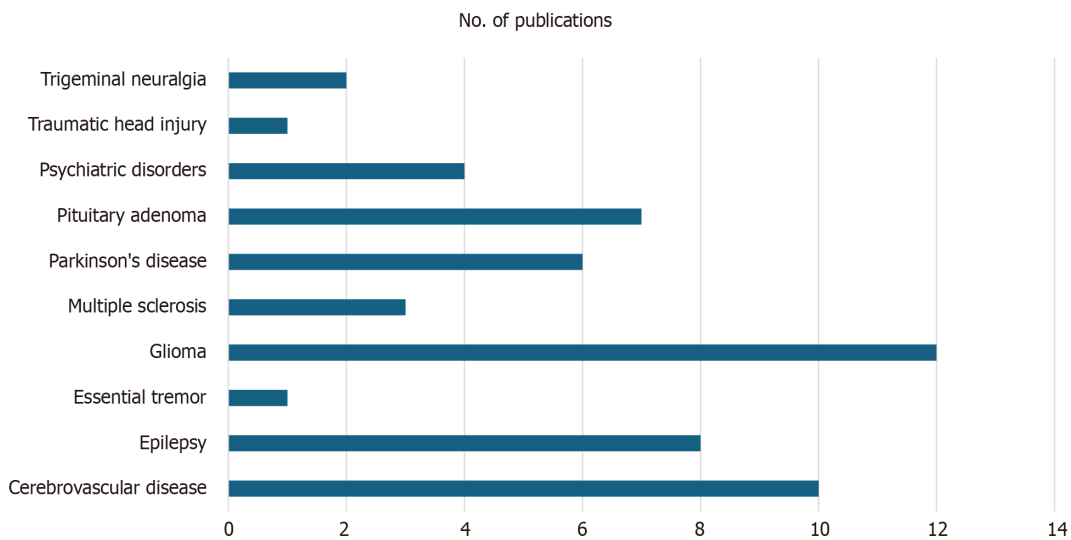


Figure 3 Chart showing number of 7T publications per neurosurgically treated pathology.

(QSM) images for five PD patients. The analysis showed that neurosurgeons were consistent in selecting the DBS target site across MRI field strengths, MRI contrast, and repetitions. However, when examining the coordinates in MNI space, it was observed that the chosen electrode location appeared to be more ventral with the 3T scan compared to the 7T scans. This suggests that while neurosurgeons maintain stability in their target selection, the higher anatomical information provided by 7T imaging might influence the actual location of the electrode during DBS placement[28]. A recent work outlined a workflow for integrating high-resolution *in vivo* ultra-high-field templates into the surgical navigation system to aid in DBS planning. Importantly, this method does not impose any additional cost or time on the patient. Future efforts will focus on prospectively evaluating various templates and assessing their impact on target selection[27]. A recent study based on 25 patients delved into the potential optimization of DBS through the combination of 7T T2-weighted and DWI sequences, enabling the selective segmentation of motor, associative, and limbic segments within the STN[17]. While the dorsolateral STN consistently housed the highest density of motor connections, the specific partitioning of segments varied among patients[29]. Notably, active electrode contacts within the predominantly motor-connected segment exhibited an average hemi-body unified PD rating scale motor improvement of 80%, contrasting with 52% outside this segment ($P < 0.01$). The study concluded that implementing 7T T2 and DWI segmentation offers insights into the location of the motor segment in DBS for PD[29]. Guided electrode placement based on segmentation is anticipated to enhance motor response, yet widespread implementation would benefit from the availability of commercial DBS software for postprocessing imaging[29]. In addition, a recent study aimed to validate the clinical application accuracy of the 7T-machine learning (ML) method by comparing it with the identification of the STN based on intraoperative microelectrode recordings and demonstrated that the 7T-ML method demonstrates high consistency with microelectrode-recordings data, offering a reliable and accurate patient-specific prediction for targeting the STN[30].

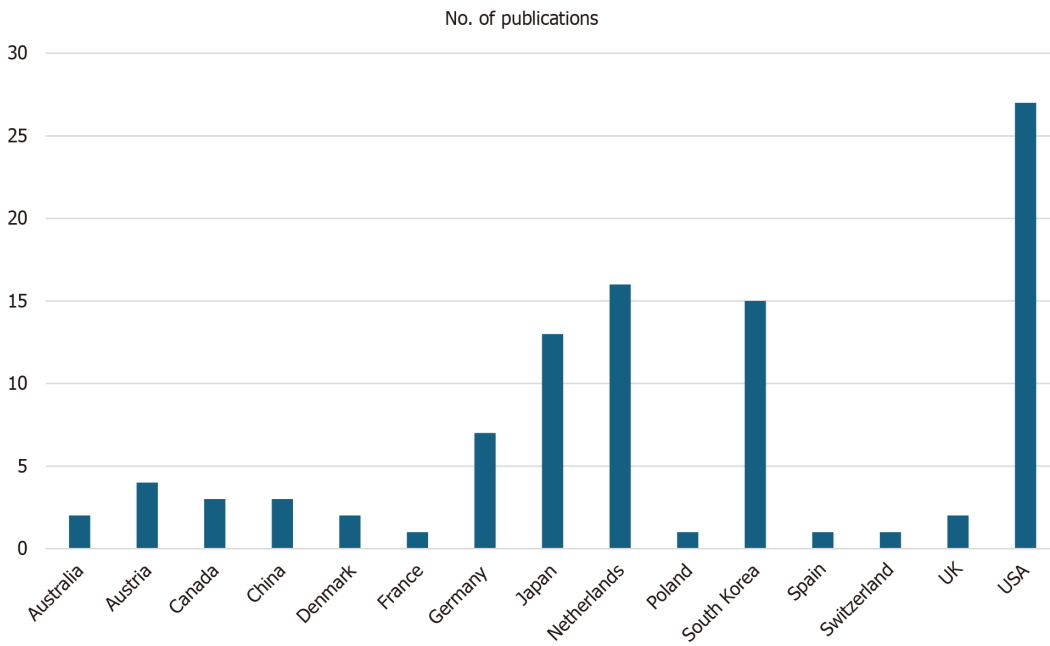


Figure 4 Histogram showing number of 7T publications per country.

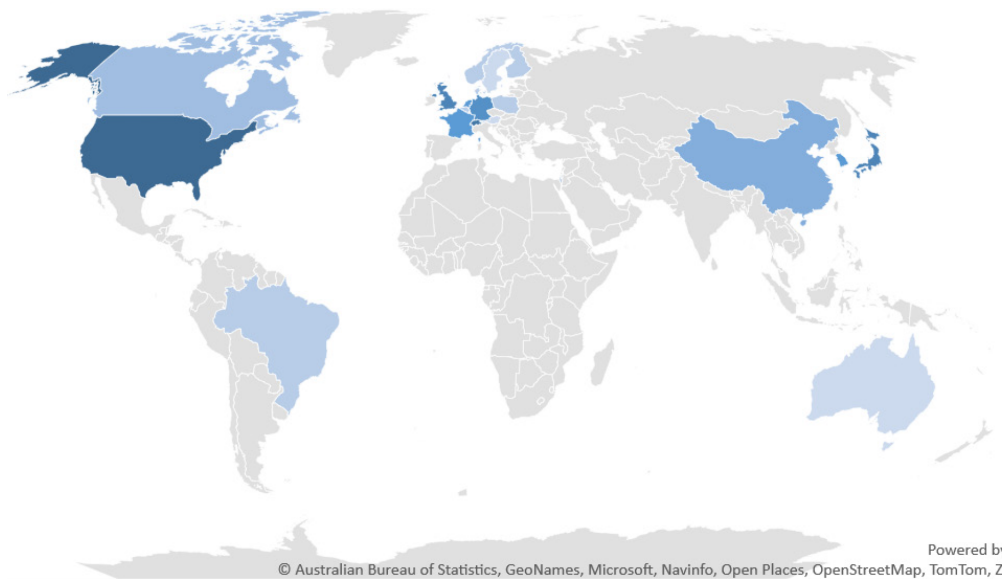


Figure 5 7-Tesla magnetic resonance imaging facilities per country. Australia (2), Austria (2), Belgium (1), Brazil (1), Canada (3), China (9), Denmark (1), Finland (1), France (4), Germany (18), Israel (1), Japan (6), Netherlands (4), Norway (1), Poland (1), South Korea (4), Sweden (2), Switzerland (5), United Kingdom (6), United States (35).

Cerebrovascular diseases

Comparison of 3T and 7T MRI in visualizing intracranial arterial vessel wall and vessel wall lesions has demonstrated the potential superiority of 7T MRI in providing enhanced resolution and detailed characterization of vessel wall abnormalities in cerebrovascular diseases[31]. Despite considerable variability in detected lesions at both field strengths, 7T MRI has the highest potential for identifying the overall burden of intracranial vessel wall lesions[31]. For example, a prospective evaluation of the utility of non-contrast-enhanced 7T magnetic resonance (MR) angiography (MRA) for delineating UIAs within a clinical setting showed comparability to the gold standard, digital subtraction angiography. The combined use of 7T non-enhanced magnetization-prepared rapid gradient echo and time-of-flight MRA for evaluating untreated UIAs emerges as a promising clinical application of ultra-high-field MRA[32]. Delineation of regions of wall weak in intracranial aneurysms has been performed using 7T MRI to identify areas prone to rupture, providing valuable insights into the structural characteristics of aneurysm walls and potentially contributing to risk stratification and personalized treatment strategies[33]. In most cases, there was an observed hyperintense rim effect along the vessel wall where there were demonstrated elevated values of mean wall shear stress (WSS) and vorticity, as analyzed by computational fluid dynamics[33]. In a retrospective, cross-sectional study utilizing 4D flow MRI at 7 T, the hemo-

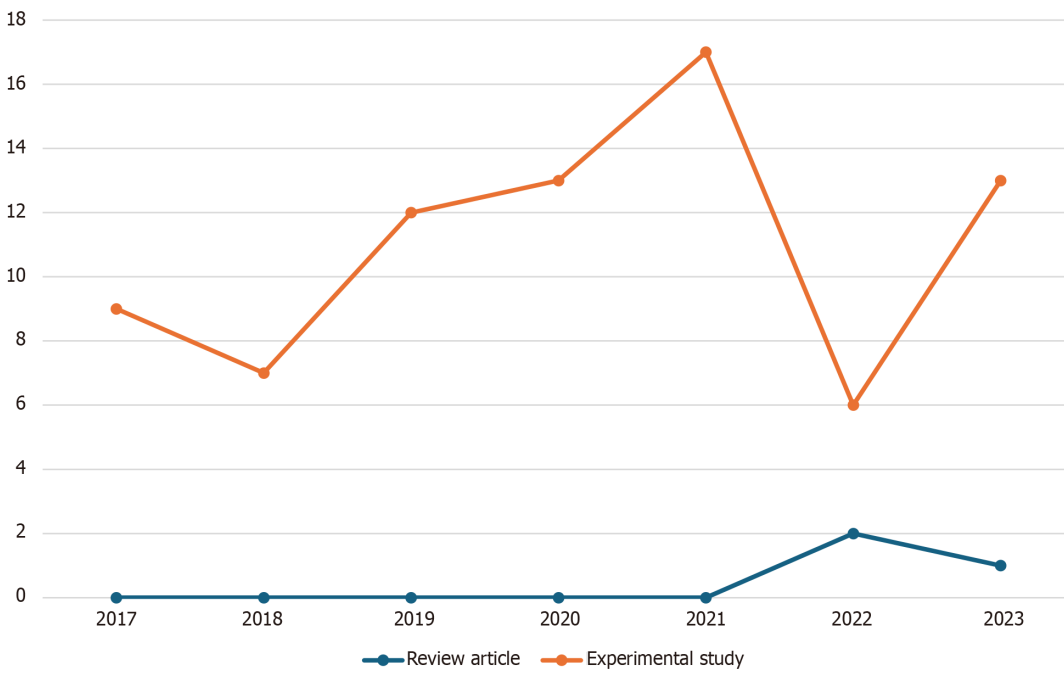


Figure 6 Illustration of number of 7T publications, both review papers and experimental studies, published in each year from 2017 to 2023.

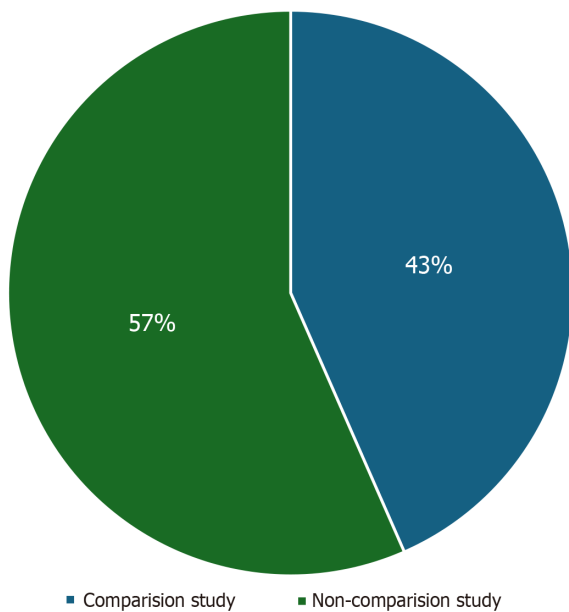


Figure 7 Pie chart showing share of comparison vs non-comparison studies.

dynamic characteristics along the circle of Willis have been investigated to gain insights into the development of UIAs [34]. Thirty-eight patients with UIAs, primarily women with a mean age of 62 years, were assessed for hemodynamic parameters in the parent artery of the UIA compared to the corresponding contralateral artery without a UIA. Results indicated significant differences in blood flow, mean velocity, WSS maxima and mean values, and velocity pulsatility index between the two arteries. Importantly, WSSmax increases linearly, while WSSmean decreases linearly with increasing UIA size. The findings suggested distinct hemodynamic variations between vessels with and without UIAs and highlighted the potential role of WSS in the pathology of aneurysm development[34]. The radiofrequency (RF)-induced tissue heating around aneurysm clips during a 7T head MR examination was also evaluated and aimed to determine the decoupling distance between multiple implanted clips to ensure the safety and feasibility of 7T MRI in these patients[35]. In a 7T ultra-high field MRI setting, safe scanning conditions regarding RF-induced heating can be implemented for single or decoupled aneurysm clips; however, more research is required for cases involving multiple aneurysm clips separated by less than 35 mm to ensure safety in this specific configuration[35]. The potential of oxygen

extraction fraction (OEF) maps generated by MR QSM at 7 T in detecting OEF changes was also investigated. The comparison with positron emission tomography (PET) results establishes the capability of 7T MRI to non-invasively monitor OEF alterations, offering a valuable alternative to traditional imaging modalities, ultimately helping avoid unnecessary radiation exposure[36]. In patients with unilateral steno-occlusive internal carotid artery/middle cerebral artery lesions, OEF ratios on 7T QSM images demonstrated a strong correlation with those on PET images, suggesting that OEF measurement by MRI has the potential to serve as a substitute for PET[36]. A study also explored the use of whole-brain MRA at 7 T for the non-invasive detection of impaired cerebrovascular reactivity in patients in an attempt to assess cerebrovascular function in patients with chronic cerebral ischemia[37]. The occurrence of a striped occipital cortex and intragyral hemorrhage, previously detected on ultra-high-field 7T MRI in hereditary cerebral amyloid angiopathy (CAA), was recently investigated. Researchers aimed to determine whether these markers are also present in sporadic CAA (sCAA) or non-sCAA ICH, contributing to the understanding of imaging markers in different forms of CAA[38]. While a striped occipital cortex was uncommon in superficial cortical siderosis (sCAA), approximately 12% of patients with sCAA exhibited intragyral hemorrhages which were also found to be associated with advanced disease, and their absence in patients with non-superficial cortical siderosis ICHs may suggest a level of specificity for CAA[38]. The presence and extent of contrast agent leakage distant from the hematoma were found as a marker of blood-brain barrier (BBB) disruption in patients with spontaneous ICH occurring in the previous days or weeks. The use of 7T MRI allows for a detailed examination of BBB integrity, providing valuable information on the extent of vascular damage in the surrounding brain tissue[39]. Next, a study compared cerebral cavernous malformations (CCMs)-associated cerebral venous angioarchitecture between sporadic and familial cases using 7T MRI. This investigation provided insights into the vascular alterations associated with CCMs, potentially aiding in the differentiation and characterization of familial and sporadic cases[40]. The susceptibility-weighted imaging (SWI) results of the venous angioarchitecture of multiple CCMs were consistent with the theory that venous anomalies are causative for the sporadic form of multiple CCMs[40].

Trigeminal neuralgia

7T MRI has been explored for investigating diffusion tensor imaging (DTI) parameters and assessing the feasibility of DTI criteria for diagnosing trigeminal neuralgia (TN). By examining the microstructural integrity of the trigeminal nerve, researchers aimed to identify specific DTI parameters that may serve as diagnostic indicators for TN[41]. 7T MRI was employed to investigate the central causal mechanisms of TN and the surrounding brain structure. By comparing healthy controls (HCs) with patients suffering from TN, researchers aimed to identify structural and functional alterations in the trigeminal nerve and associated brain regions. The high resolution and sensitivity of 7T MRI enable a detailed examination, shedding light on potential biomarkers and contributing to our understanding of the underlying mechanisms of TN[42]. Results suggest that the central anterior cingulate cortex and posterior cingulate cortex, but not the rostral anterior cingulate cortex, are associated with central pain mechanisms in TN[42].

Traumatic head injury

A study examined the potential prognostic advantages of utilizing 7T SWI for traumatic cerebral microbleeds (TMBs) in comparison to 3T SWI. The aim was to forecast the immediate clinical condition and subjective impairments, encompassing health-related quality of life, following a closed head injury (CHI). The number of TMBs showed a substantial association with indicators of the acute clinical state and chronic neurobehavioral parameters after a CHI, but there was no additional advantage of 7T MRI. These preliminary findings warrant a larger prospective study for the future[43].

Multiple sclerosis

Fluid-attenuated inversion recovery (FLAIR) imaging at 3 T is recognized as the most sensitive method for identifying white matter lesions in multiple sclerosis (MS). Although 7T FLAIR effectively detects cortical lesions, it has not been fully optimized for visualizing white matter lesions, thus limiting its use in delineating lesions in quantitative MRI studies of normal-appearing white matter in MS. As a result, a team assessed the sensitivity of 7T magnetization-transfer-weighted (MTw) images in detecting white matter lesions in comparison to 3T FLAIR. The findings indicate that 7T MTw sequences successfully identified the majority of white matter lesions detected by FLAIR at 3 T, thus implying that 7T MTw imaging can serve as a robust alternative alongside 3T FLAIR. Subsequent studies should explore and compare the roles of optimized 7T-FLAIR and 7T-MTw imaging[44]. A recent study aimed to pinpoint white matter tracts (WMTs) associated with the severity of neurogenic lower urinary tract dysfunction (NLUTD) in women with MS[45]. The primary cohort included 28 women with MS and NLUTD, and a validation cohort comprised 10 women with similar conditions. Both cohorts underwent clinical assessments and functional MRI protocols, with the validation cohort additionally undergoing a 7T fMRI scan[45]. The study identified a robust correlation between fractional anisotropy and mean diffusivity of specific WMTs and clinical parameters related to NLUTD symptoms in women with MS, notably the right inferior cerebellar peduncle, left posterior limb of the internal capsule, and left superior cerebellar peduncle[45]. Another study aimed to characterize cortical lesions in MS using 7T T2/T1-weighted MRI and assess their relationship with other MS pathology and impact on disability[46]. In 64 adults with MS (45 relapsing-remitting/19 progressive), cortical lesions were identified in 94%, with a higher burden in progressive MS compared to relapsing-remitting MS. The distribution of lesions across 50 cortical regions was nonuniform, with the highest lesion burden in the supplementary motor cortex and the highest prevalence in the superior frontal gyrus. Leukocortical lesions were strongly correlated with white matter lesions and paramagnetic rim lesions, while subpial lesions showed a moderate correlation; however, both were correlated with spinal cord lesions. Cortical lesion volumes, including subtypes, were correlated with disability measures, suggesting their significant role in the clinical course of MS[46].

Glioma

Ultra-high-field MRI of the brain is an appealing option for image guidance during neurosurgery due to its superior tissue contrast and detailed vessel visualization. However, the susceptibility of high-field MRI to distortion artifacts poses a potential challenge to image guidance accuracy. In a study, researchers specifically examined intra- and extracranial distortions in 7T MRI scans. Upon inspection of magnetization-prepared T1-weighted 7T MRI cranial images, no discernible intracranial distortions were observed. However, noteworthy extracranial shifts were identified, introducing a level of unreliability in 7T images when used for patient-to-image registration. To address this issue, researchers recommend conducting patient-to-image registration on a standard imaging modality, such as a routine computed tomography scan or a 3T MR image. Subsequently, the 7T MRI image can be fused with the routine image on the image guidance machine. This proposed approach is advised until a resolution is achieved for the observed extracranial shifts in 7T MRI scans[47]. An exploratory study aimed to assess the potential clinical implications of single-voxel 7T MR spectroscopy (MRS) in patients with grades II and III gliomas[48]. Seven patients and seven HCs were scanned, and metabolic ratios were calculated relative to water and total creatine. The results revealed significant increases in choline/creatinine and myoinositol/creatinine ratios, along with decreases in N-acetyl aspartate/creatinine and glutamate/creatinine ratios when comparing tumor data to control regions[48]. The N-acetyl aspartate/water and glutamate/water ratios also showed significant decreases. Lactate/water and lactate/creatinine ratios displayed increases, albeit not significant. GABA/water ratio was significantly decreased, and MRS spectra confirmed the presence of 2-hydroxyglutarate in three out of four patients studied. Overall, the study, conducted at 7 T, yielded results consistent with existing literature on both 3T and 7T MRS in glioma research[48]. In a retrospective study of 84 glioma patients, the potential for preoperative identification of isocitrate dehydrogenase (IDH) mutation status in glioma was explored using a combination of convolutional neural network (CNN) and ultra-high-field 7T chemical exchange saturation transfer (CEST) imaging[49]. The study demonstrated the potential of ultra-high-field CEST and CNN for improving sensitivity and specificity in predicting IDH mutation status, surpassing radionics-based predictions in various metrics. The authors emphasized the promising role of this approach in clinical decision-making while acknowledging the need for further improvement in accuracy through expanded datasets and addressing B1 inhomogeneities[49]. Using high fluoro-ethyl-L-tyrosine uptake as the standard, the combination of CEST and MRS was shown to outperform individual modalities in predicting tumor infiltration, presenting a promising alternative for delineating glioma extent without the use of radioactive tracers. The study's preliminary verification through multi-region biopsies supports the potential clinical relevance of the 7T CEST/MRS combination in guiding tumor resection and irradiation[50].

Psychiatric disorders

A team explored the potential for individuals to acquire the skill of dynamically controlling the activity of the dorsolateral prefrontal cortex (DLPFC). The DLPFC is recognized for its significance in working memory function and its association with various psychiatric disorders. This study also sought to delve into the learnability of such dynamic control, which may have implications for our understanding of cognitive processes and mental health conditions[51]. These findings offer an initial indication that individuals may have the capacity to learn to dynamically down-regulate physiological activity in the DLPFC. This has potential implications for psychiatric disorders in which the DLPFC plays a significant role[51]. Another study utilized a combination of high-resolution and quantitative MRI, employing both supervised and unsupervised computational techniques. This approach enabled the acquisition of robust sub-millimeter measurements of the locus coeruleus (LC) *in vivo*. Additionally, the study investigated the correlation of these measurements with prevalent psychopathological conditions. The implications of this work extend broadly, as it holds the potential to impact various neurological and psychiatric disorders known for their association with anticipated LC dysfunction[52]. This study combined high-resolution and quantitative MR with a mixture of supervised and unsupervised computational techniques to provide robust, sub-millimeter measurements of the LC *in vivo*, which were additionally related to common psychopathology. This work has wide-reaching applications for a range of neurological and psychiatric disorders characterized by expected LC dysfunction[52]. In a recent study, 22 PD patients who underwent STN DBS were categorized into apathy and non-apathy groups based on changes in the Starkstein Apathy Scale score 6 mo post-DBS[53]. Using 7T MRI subthalamic network analysis, the location of active DBS contacts relative to STN subdivisions (motor, associative, and limbic) was visualized. The analysis revealed that active contacts in apathy patients were more often positioned within or close to the area within the STN with a high density of surrounding projections to associative cortex areas compared to non-apathy patients (63% vs 42%, $P = 0.02$). Conversely, the density of surrounding motor projections was lower in the apathy group (18%) than in the non-apathy group (38%, $P = 0.01$). The study suggests an anatomical connectivity substrate for apathy in DBS, emphasizing the importance of considering the location of active contacts within the STN in relation to its subdivisions for understanding and potentially mitigating apathy in PD patients undergoing DBS[53]. A study aimed to explore volumetric differences in hippocampal subfields between patients with major depressive disorder (MDD), specifically treatment-resistant depression (TRD), and HCs using automatic segmentation of hippocampal subfields software with ultra-high-field 7T MRI[54]. The results revealed reduced right-hemisphere CA2/3 subfield volume in both MDD and TRD patients compared to HCs. Moreover, negative associations were found between subfield volumes and life-stressor checklist scores. The study highlights the potential of high-resolution MRI data and automated segmentation techniques to identify biomarkers for MDD and TRD, providing insights into the pathophysiology of depression and potential implications for treatment selection. However, the authors acknowledge the need for caution in interpreting these results due to the small sample size and low power, emphasizing the importance of further research in this area[54].

Limitations of our analysis

It is essential to highlight the limitations of our study. Initially, it is worth noting that our examination of records might have overlooked certain publications cataloged in alternative databases such as EMBASE, Scopus, Google Scholar, among others. Nevertheless, PubMed is renowned for its accurate and top-tier content sourced from peer-reviewed medical journals, underscoring its suitability for conducting systematic reviews in the medical field. Systematic reviews inherently involve a balance between comprehensiveness and practicality, and the inclusion of an excessive number of databases can lead to cumbersome processing times. In addition, we would like to highlight that a manual exploration of EMBASE using identical search criteria revealed minimal oversight of studies, indicating that the decision to abstain from its utilization incurred relatively minor drawbacks. Study selection bias could have occurred due to restriction to English language records, and search strategy constraints such as the non-inclusion of terms such as 7 T and 7-T potentially leading to skewed conclusions by systematically excluding certain studies. Excluding grey literature further compounds this issue, as valuable data from unpublished sources may be overlooked, resulting in an incomplete representation of evidence. Publication bias exacerbates these concerns, favoring the publication of studies with positive or significant results and potentially distorting the overall evidence base. Another limitation of our study was that if an author affiliated to the Neurosurgery Department was involved in the manuscript, the study was included even though a neurosurgical procedure was not discussed in the article. Lastly, although we retrieved a total of 85 studies into our database, only 49 out of those have been referenced in this review in [Table 1](#) since their findings were relevant to a specific pathology while the remaining have only been denoted in the figures (were used only for analysis and generation of the data)[55-57].

CONCLUSION

The findings open avenues for further exploration and integration of 7T imaging into routine clinical practice, promising improved patient outcomes and refined surgical interventions. However, this will be possible only if the distribution of 7T MR systems is accelerated worldwide and radiologists receive enough training regarding safety measures, feasibility, and other challenges. The adoption of 7T MRI faces significant barriers, primarily revolving around its substantial cost and potential side effects. With the machine alone costing approximately 6.5 million dollars, considerations extend to the energy consumption and space requirements. Moreover, concerns regarding side effects such as vertigo further impede its acceptance. Safety issues arise due to the stronger magnetic field, posing risks to patients with metallic implants or devices, alongside challenges in achieving consistent image quality and contrast uniformity. Regulatory hurdles for clinical application also loom large. To surmount these obstacles, concerted efforts are essential. Ongoing research is crucial to address safety concerns and establish clear guidelines for safe usage. Advancements in imaging techniques and software are necessary to enhance image quality. Collaborative endeavors among researchers, clinicians, and regulators are pivotal for setting standards and protocols, defining gold standards for clinical use. Additionally, increasing awareness and providing education on the manifold benefits of 7T MRI are imperative to foster its wider adoption in clinical practice. A continuously updated list of 7T MRI facilities and their relevant locations globally can be accessed at <https://www.google.com/maps/d/u/0/viewer?ll=1.941826124046989%2C0&z=2&mid=1dXG84OZIAOxjsq-h3x2tGzWL1bNU>.

FOOTNOTES

Author contributions: Perera Molligoda Arachchige AS conceived of the presented idea and performed the analysis; Catapano F and Politi LS verified the analytical methods. All authors discussed the results and contributed to writing the final manuscript.

Conflict-of-interest statement: The authors have no conflicts of interest to declare.

PRISMA 2009 Checklist statement: The authors have read the PRISMA 2009 Checklist, and the manuscript was prepared and revised according to the PRISMA 2009 Checklist.

Open-Access: This article is an open-access article that was selected by an in-house editor and fully peer-reviewed by external reviewers. It is distributed in accordance with the Creative Commons Attribution NonCommercial (CC BY-NC 4.0) license, which permits others to distribute, remix, adapt, build upon this work non-commercially, and license their derivative works on different terms, provided the original work is properly cited and the use is non-commercial. See: <https://creativecommons.org/licenses/by-nc/4.0/>

Country of origin: Italy

ORCID number: Arosh S Perera Molligoda Arachchige 0000-0002-3875-0267; Letterio S Politi 0000-0002-6190-6688.

S-Editor: Qu XL

L-Editor: Wang TQ

P-Editor: Che XX

REFERENCES

- 1 Arachchige ASPM. Transitioning from PET/MR to trimodal neuroimaging: why not cover the temporal dimension with EEG? *AIMS Neurosci* 2023; **10**: 1-4 [PMID: 37077957 DOI: 10.3934/Neuroscience.2023001]
- 2 Perera Molligoda Arachchige AS. Neuroimaging with PET/MR: moving beyond 3 T in preclinical systems, when for clinical practice? *Clin Transl Imaging* 2023; **11**: 315-319 [DOI: 10.1007/s40336-023-00572-6]
- 3 Arachchige ASPM. 7-Tesla PET/MRI: A promising tool for multimodal brain imaging? *AIMS Neurosci* 2022; **9**: 516-518 [PMID: 36660074 DOI: 10.3934/Neuroscience.2022029]
- 4 Verma Y, Ramesh S, Perera Molligoda Arachchige AS. 7 T Versus 3 T in the Diagnosis of Small Unruptured Intracranial Aneurysms: Reply to Radojewski et al. *Clin Neuroradiol* 2024; **34**: 51-52 [PMID: 37318559 DOI: 10.1007/s00062-023-01321-y]
- 5 Cosottini M, Roccatagliata L. Neuroimaging at 7 T: are we ready for clinical transition? *Eur Radiol Exp* 2021; **5**: 37 [PMID: 34435257 DOI: 10.1186/s41747-021-00234-0]
- 6 Okada T, Fujimoto K, Fushimi Y, Akasaka T, Thuy DHD, Shima A, Sawamoto N, Oishi N, Zhang Z, Funaki T, Nakamoto Y, Murai T, Miyamoto S, Takahashi R, Isa T. Neuroimaging at 7 Tesla: a pictorial narrative review. *Quant Imaging Med Surg* 2022; **12**: 3406-3435 [PMID: 35655840 DOI: 10.21037/qims-21-969]
- 7 Whiting PF, Rutjes AW, Westwood ME, Mallett S, Deeks JJ, Reitsma JB, Leeflang MM, Sterne JA, Bossuyt PM; QUADAS-2 Group. QUADAS-2: a revised tool for the quality assessment of diagnostic accuracy studies. *Ann Intern Med* 2011; **155**: 529-536 [PMID: 22007046 DOI: 10.7326/0003-4819-155-8-201110180-00009]
- 8 Sterne JAC, Savović J, Page MJ, Elbers RG, Blencowe NS, Boutron I, Cates CJ, Cheng HY, Corbett MS, Eldridge SM, Emberson JR, Hernán MA, Hopewell S, Hróbjartsson A, Junqueira DR, Jüni P, Kirkham JJ, Lasserson T, Li T, McAleenan A, Reeves BC, Shepperd S, Shrier I, Stewart LA, Tilling K, White IR, Whiting PF, Higgins JPT. RoB 2: a revised tool for assessing risk of bias in randomised trials. *BMJ* 2019; **366**: 14898 [PMID: 31462531 DOI: 10.1136/bmj.l4898]
- 9 Page MJ, McKenzie JE, Bossuyt PM, Boutron I, Hoffmann TC, Mulrow CD, Shamseer L, Tetzlaff JM, Akl EA, Brennan SE, Chou R, Ghanaville J, Grimshaw JM, Hróbjartsson A, Lalu MM, Li T, Loder EW, Mayo-Wilson E, McDonald S, McGuinness LA, Stewart LA, Thomas J, Tricco AC, Welch VA, Whiting P, Moher D. The PRISMA 2020 statement: an updated guideline for reporting systematic reviews. *BMJ* 2021; **372**: n71 [PMID: 33782057 DOI: 10.1136/bmj.n71]
- 10 Stefanits H, Springer E, Pataria E, Baumgartner C, Hainfellner JA, Prayer D, Weisstanner C, Czech T, Trattinig S. Seven-Tesla MRI of Hippocampal Sclerosis: An In Vivo Feasibility Study With Histological Correlations. *Invest Radiol* 2017; **52**: 666-671 [PMID: 28538339 DOI: 10.1097/RLI.0000000000000388]
- 11 Zhang Y, Lv Y, You H, Dou W, Hou B, Shi L, Zuo Z, Mao W, Feng F. Study of the hippocampal internal architecture in temporal lobe epilepsy using 7 T and 3 T MRI. *Seizure* 2019; **71**: 116-123 [PMID: 31325818 DOI: 10.1016/j.seizure.2019.06.023]
- 12 Wang I, Oh S, Blümcke J, Coras R, Krishnan B, Kim S, McBride A, Grinenko O, Lin Y, Overmyer M, Aung TT, Lowe M, Larvie M, Alexopoulos AV, Bingaman W, Gonzalez-Martinez JA, Najm I, Jones SE. Value of 7T MRI and post-processing in patients with nonlesional 3T MRI undergoing epilepsy presurgical evaluation. *Epilepsia* 2020; **61**: 2509-2520 [PMID: 32949471 DOI: 10.1111/epi.16682]
- 13 Veersema TJ, Ferrier CH, van Eijsden P, Gosselaar PH, Aronica E, Visser F, Zwanenburg JM, de Kort GAP, Hendrikse J, Luijten PR, Braun KPJ. Seven tesla MRI improves detection of focal cortical dysplasia in patients with refractory focal epilepsy. *Epilepsia Open* 2017; **2**: 162-171 [PMID: 29588945 DOI: 10.1002/epi4.12041]
- 14 Sharma HK, Feldman R, Delman B, Rutland J, Marcuse LV, Fields MC, Ghatan S, Panov F, Singh A, Balchandani P. Utility of 7 tesla MRI brain in 16 "MRI Negative" epilepsy patients and their surgical outcomes. *Epilepsy Behav Rep* 2021; **15**: 100424 [PMID: 33521618 DOI: 10.1016/j.ebr.2020.100424]
- 15 Rutland JW, Feldman RE, Delman BN, Panov F, Fields MC, Marcuse LV, Hof PR, Lin HM, Balchandani P. Subfield-specific tractography of the hippocampus in epilepsy patients at 7 Tesla. *Seizure* 2018; **62**: 3-10 [PMID: 30245458 DOI: 10.1016/j.seizure.2018.09.005]
- 16 van Lanen RHGJ, Colon AJ, Wiggins CJ, Hoebregers MC, Hoogland G, Roebroek A, Ivanov D, Poser BA, Rouhl RPW, Hofman PAM, Jansen JFA, Backes W, Rijkers K, Schijns OEMG. Ultra-high field magnetic resonance imaging in human epilepsy: A systematic review. *Neuroimage Clin* 2021; **30**: 102602 [PMID: 33652376 DOI: 10.1016/j.nicl.2021.102602]
- 17 Rutland JW, Delman BN, Feldman RE, Tsankova N, Lin HM, Padormo F, Shrivastava RK, Balchandani P. Utility of 7 Tesla MRI for Preoperative Planning of Endoscopic Endonasal Surgery for Pituitary Adenomas. *J Neurol Surg B Skull Base* 2021; **82**: 303-312 [PMID: 34026406 DOI: 10.1055/s-0039-3400222]
- 18 Yao A, Rutland JW, Verma G, Banihashemi A, Padormo F, Tsankova NM, Delman BN, Shrivastava RK, Balchandani P. Pituitary adenoma consistency: Direct correlation of ultrahigh field 7T MRI with histopathological analysis. *Eur J Radiol* 2020; **126**: 108931 [PMID: 32146344 DOI: 10.1016/j.ejrad.2020.108931]
- 19 Perera Molligoda Arachchige AS, Politi LS. Potential applications of 7 Tesla magnetic resonance imaging in paediatric neuroimaging: Feasibility and challenges. *World J Clin Pediatr* 2024; **13**: 90641 [DOI: 10.5409/wjcp.v13.i2.90641]
- 20 Rutland JW, Padormo F, Yim CK, Yao A, Arrighi-Allisan A, Huang KH, Lin HM, Chelnis J, Delman BN, Shrivastava RK, Balchandani P. Quantitative assessment of secondary white matter injury in the visual pathway by pituitary adenomas: a multimodal study at 7-Tesla MRI. *J Neurosurg* 2019; **132**: 333-342 [PMID: 30660127 DOI: 10.3171/2018.9.JNS182022]
- 21 Rutland JW, Delman BN, Huang KH, Verma G, Benson NC, Villavisanis DF, Lin HM, Bederson JB, Chelnis J, Shrivastava RK, Balchandani P. Primary visual cortical thickness in correlation with visual field defects in patients with pituitary macroadenomas: a structural 7-Tesla retinotopic analysis. *J Neurosurg* 2019; **133**: 1371-1381 [PMID: 31628280 DOI: 10.3171/2019.7.JNS191712]
- 22 Patel V, Liu CJ, Shiroishi MS, Hurth K, Carmichael JD, Zada G, Toga AW. Ultra-high field magnetic resonance imaging for localization of corticotropin-secreting pituitary adenomas. *Neuroradiology* 2020; **62**: 1051-1054 [PMID: 32306052 DOI: 10.1007/s00234-020-02431-x]
- 23 Rutland JW, Loewenstern J, Ranti D, Tsankova NM, Bellaire CP, Bederson JB, Delman BN, Shrivastava RK, Balchandani P. Analysis of 7-tesla diffusion-weighted imaging in the prediction of pituitary macroadenoma consistency. *J Neurosurg* 2020; **134**: 771-779 [PMID: 32109870 DOI: 10.3171/2019.12.JNS192940]
- 24 Rutland JW, Pawha P, Belani P, Delman BN, Gill CM, Brown T, Cheesman K, Shrivastava RK, Balchandani P. Tumor T2 signal intensity and stalk angulation correlates with endocrine status in pituitary adenoma patients: a quantitative 7 tesla MRI study. *Neuroradiology* 2020; **62**: 473-482 [PMID: 31925468 DOI: 10.1007/s00234-019-02352-4]
- 25 Oh BH, Moon HC, Kim A, Kim HJ, Cheong CJ, Park YS. Prefrontal and hippocampal atrophy using 7-tesla magnetic resonance imaging in

- patients with Parkinson's disease. *Acta Radiol Open* 2021; **10**: 2058460120988097 [PMID: 33786201 DOI: 10.1177/2058460120988097]
- 26 **La C**, Linortner P, Bernstein JD, Ua Cruadhlaioich MAI, Fenesy M, Deutsch GK, Rutt BK, Tian L, Wagner AD, Zeineh M, Kerchner GA, Poston KL. Hippocampal CA1 subfield predicts episodic memory impairment in Parkinson's disease. *Neuroimage Clin* 2019; **23**: 101824 [PMID: 31054380 DOI: 10.1016/j.nicl.2019.101824]
- 27 **Lau JC**, MacDougall KW, Arango MF, Peters TM, Parrent AG, Khan AR. Ultra-High Field Template-Assisted Target Selection for Deep Brain Stimulation Surgery. *World Neurosurg* 2017; **103**: 531-537 [PMID: 28427973 DOI: 10.1016/j.wneu.2017.04.043]
- 28 **Isaacs BR**, Heijmans M, Kuijf ML, Kubben PL, Ackermans L, Temel Y, Keuken MC, Forstmann BU. Variability in subthalamic nucleus targeting for deep brain stimulation with 3 and 7 Tesla magnetic resonance imaging. *Neuroimage Clin* 2021; **32**: 102829 [PMID: 34560531 DOI: 10.1016/j.nicl.2021.102829]
- 29 **Mathiopoulou V**, Rijks N, Caan MWA, Liebrand LC, Ferreira F, de Bie RMA, van den Munckhof P, Schuurman PR, Bot M. Utilizing 7-Tesla Subthalamic Nucleus Connectivity in Deep Brain Stimulation for Parkinson Disease. *Neuromodulation* 2023; **26**: 333-339 [PMID: 35216874 DOI: 10.1016/j.neurom.2022.01.003]
- 30 **Shamir RR**, Duchin Y, Kim J, Patriat R, Marmor O, Bergman H, Vitek JL, Sapiro G, Bick A, Eliahou R, Eitan R, Israel Z, Harel N. Microelectrode Recordings Validate the Clinical Visualization of Subthalamic-Nucleus Based on 7T Magnetic Resonance Imaging and Machine Learning for Deep Brain Stimulation Surgery. *Neurosurgery* 2019; **84**: 749-757 [PMID: 29800386 DOI: 10.1093/neuros/nyy212]
- 31 **Harteveld AA**, van der Kolk AG, van der Worp HB, Dieleman N, Siero JCW, Kuijf HJ, Frijns CJM, Luijten PR, Zwanenburg JJM, Hendrikse J. High-resolution intracranial vessel wall MRI in an elderly asymptomatic population: comparison of 3T and 7T. *Eur Radiol* 2017; **27**: 1585-1595 [PMID: 27387876 DOI: 10.1007/s00330-016-4483-3]
- 32 **Wrede KH**, Matsushige T, Goericke SL, Chen B, Umütlu L, Quick HH, Ladd ME, Johst S, Forsting M, Sure U, Schlamann M. Non-enhanced magnetic resonance imaging of unruptured intracranial aneurysms at 7 Tesla: Comparison with digital subtraction angiography. *Eur Radiol* 2017; **27**: 354-364 [PMID: 26993650 DOI: 10.1007/s00330-016-4323-5]
- 33 **Millesi M**, Knosp E, Mach G, Hainfellner JA, Ricken G, Trattinig S, Gruber A. Focal irregularities in 7-Tesla MRI of unruptured intracranial aneurysms as an indicator for areas of altered blood-flow parameters. *Neurosurg Focus* 2019; **47**: E7 [PMID: 31786557 DOI: 10.3171/2019.9.FOCUS19489]
- 34 **van Tuijl RJ**, Timmins KM, Velthuis BK, van Ooij P, Zwanenburg JJM, Ruigrok YM, van der Schaaf IC. Hemodynamic Parameters in the Parent Arteries of Unruptured Intracranial Aneurysms Depend on Aneurysm Size and Are Different Compared to Contralateral Arteries: A 7 Tesla 4D Flow MRI Study. *J Magn Reson Imaging* 2024; **59**: 223-230 [PMID: 37144669 DOI: 10.1002/jmri.28756]
- 35 **Noureddine Y**, Kraff O, Ladd ME, Wrede K, Chen B, Quick HH, Schaefer G, Bitz AK. Radiofrequency induced heating around aneurysm clips using a generic birdcage head coil at 7 Tesla under consideration of the minimum distance to decouple multiple aneurysm clips. *Magn Reson Med* 2019; **82**: 1859-1875 [PMID: 31199013 DOI: 10.1002/mrm.27835]
- 36 **Uwano I**, Kudo K, Sato R, Ogasawara K, Kameda H, Nomura JI, Mori F, Yamashita F, Ito K, Yoshioka K, Sasaki M. Noninvasive Assessment of Oxygen Extraction Fraction in Chronic Ischemia Using Quantitative Susceptibility Mapping at 7 Tesla. *Stroke* 2017; **48**: 2136-2141 [PMID: 28663515 DOI: 10.1161/STROKEAHA.117.017166]
- 37 **Uwano I**, Kameda H, Harada T, Kobayashi M, Yanagihara W, Setta K, Ogasawara K, Yoshioka K, Yamashita F, Mori F, Matsuda T, Sasaki M. Detection of impaired cerebrovascular reactivity in patients with chronic cerebral ischemia using whole-brain 7T MRA. *J Stroke Cerebrovasc Dis* 2020; **29**: 105081 [PMID: 32807478 DOI: 10.1016/j.jstrokecerebrovasdis.2020.105081]
- 38 **Koemans EA**, Voigt S, Rasing I, Jolink W, van Harten TW, van der Grond J, van Rooden S, Schreuder F, Freeze WM, van Buchem MA, van Zwet EW, van Veluw SJ, Terwindt GM, van Osch M, Klijn C, van Walderveen M, Wermer M. Striped occipital cortex and intragray hemorrhage: Novel magnetic resonance imaging markers for cerebral amyloid angiopathy. *Int J Stroke* 2021; **16**: 1031-1038 [PMID: 33535905 DOI: 10.1177/1747493021991961]
- 39 **Jolink WM**, Lindenholtz A, van Etten ES, van Nieuwenhuizen KM, Schreuder FH, Kuijf HJ, van Osch MJ, Hendrikse J, Rinkel GJ, Wermer MJ, Klijn CJ. Contrast leakage distant from the hematoma in patients with spontaneous ICH: A 7 T MRI study. *J Cereb Blood Flow Metab* 2020; **40**: 1002-1011 [PMID: 31142225 DOI: 10.1177/0271678X19852876]
- 40 **Dammann P**, Wrede K, Zhu Y, Matsushige T, Maderwald S, Umütlu L, Quick HH, Hehr U, Rath M, Ladd ME, Felbor U, Sure U. Correlation of the venous angioarchitecture of multiple cerebral cavernous malformations with familial or sporadic disease: a susceptibility-weighted imaging study with 7-Tesla MRI. *J Neurosurg* 2017; **126**: 570-577 [PMID: 27153162 DOI: 10.3171/2016.2.JNS152322]
- 41 **Moon HC**, You ST, Baek HM, Jeon YJ, Park CA, Cheong JJ, Lee YJ, Park YS. 7.0 Tesla MRI tractography in patients with trigeminal neuralgia. *Magn Reson Imaging* 2018; **54**: 265-270 [PMID: 29305127 DOI: 10.1016/j.mri.2017.12.033]
- 42 **Moon HC**, Park CA, Jeon YJ, You ST, Baek HM, Lee YJ, Cho CB, Cheong CJ, Park YS. 7 Tesla magnetic resonance imaging of caudal anterior cingulate and posterior cingulate cortex atrophy in patients with trigeminal neuralgia. *Magn Reson Imaging* 2018; **51**: 144-150 [PMID: 29777819 DOI: 10.1016/j.mri.2018.05.005]
- 43 **Hütter BO**, Altmepfen J, Kraff O, Maderwald S, Theysohn JM, Ringelstein A, Wrede KH, Dammann P, Quick HH, Schlamann M, Moeninghoff C. Higher sensitivity for traumatic cerebral microbleeds at 7 T ultra-high field MRI: is it clinically significant for the acute state of the patients and later quality of life? *Ther Adv Neurol Disord* 2020; **13**: 1756286420911295 [PMID: 32313555 DOI: 10.1177/1756286420911295]
- 44 **Chou IJ**, Lim SY, Tanasescu R, Al-Radaideh A, Mouglin OE, Tench CR, Whitehouse WP, Gowland PA, Constantinescu CS. Seven-Tesla Magnetization Transfer Imaging to Detect Multiple Sclerosis White Matter Lesions. *J Neuroimaging* 2018; **28**: 183-190 [PMID: 28944575 DOI: 10.1111/jon.12474]
- 45 **Choksi D**, Schott B, Tran K, Jang R, Hasan KM, Lincoln JA, Jalali A, Karmonik C, Salazar B, Khavari R. Disruption of specific white matter tracts is associated with neurogenic lower urinary tract dysfunction in women with multiple sclerosis. *Neurol Urodyn* 2023; **42**: 239-248 [PMID: 36321777 DOI: 10.1002/nau.25075]
- 46 **Beck ES**, Maranzano J, Luciano NJ, Parvathaneni P, Filippini S, Morrison M, Suto DJ, Wu T, van Gelderen P, de Zwart JA, Antel S, Fetco D, Ohayon J, Andrada F, Mina Y, Thomas C, Jacobson S, Duyn J, Cortese I, Narayanan S, Nair G, Sati P, Reich DS. Cortical lesion hotspots and association of subpial lesions with disability in multiple sclerosis. *Mult Scler* 2022; **28**: 1351-1363 [PMID: 35142571 DOI: 10.1177/13524585211069167]
- 47 **Voormolen EH**, Diederens SJH, Woerdeman P, van der Sprenkel JWB, Noordmans HJ, Visser F, Viergever MA, Luijten P, Hoogduin H, Robe PA. Implications of Extracranial Distortion in Ultra-High-Field Magnetic Resonance Imaging for Image-Guided Cranial Neurosurgery. *World Neurosurg* 2019; **126**: e250-e258 [PMID: 30797931 DOI: 10.1016/j.wneu.2019.02.028]
- 48 **Prener M**, Opheim G, Shams Z, Søndergaard CB, Lindberg U, Larsson HBW, Ziebell M, Larsen VA, Vestergaard MB, Paulson OB. Single-

- Voxel MR Spectroscopy of Gliomas with s-LASER at 7T. *Diagnostics (Basel)* 2023; **13** [PMID: 37238288 DOI: 10.3390/diagnostics13101805]
- 49 **Yuan Y**, Yu Y, Chang J, Chu YH, Yu W, Hsu YC, Patrick LA, Liu M, Yue Q. Convolutional neural network to predict IDH mutation status in glioma from chemical exchange saturation transfer imaging at 7 Tesla. *Front Oncol* 2023; **13**: 1134626 [PMID: 37223677 DOI: 10.3389/fonc.2023.1134626]
- 50 **Yuan Y**, Yu Y, Guo Y, Chu Y, Chang J, Hsu Y, Liebig PA, Xiong J, Yu W, Feng D, Yang B, Chen L, Wang H, Yue Q, Mao Y. Noninvasive Delineation of Glioma Infiltration with Combined 7T Chemical Exchange Saturation Transfer Imaging and MR Spectroscopy: A Diagnostic Accuracy Study. *Metabolites* 2022; **12** [PMID: 36295803 DOI: 10.3390/metabo12100901]
- 51 **Van den Boom MA**, Jansma JM, Ramsey NF. Rapid acquisition of dynamic control over DLPFC using real-time fMRI feedback. *Eur Neuropsychopharmacol* 2018; **28**: 1194-1205 [PMID: 30217551 DOI: 10.1016/j.euroneuro.2018.08.508]
- 52 **Morris LS**, Tan A, Smith DA, Grehl M, Han-Huang K, Naidich TP, Charney DS, Balchandani P, Kundu P, Murrough JW. Sub-millimeter variation in human locus coeruleus is associated with dimensional measures of psychopathology: An in vivo ultra-high field 7-Tesla MRI study. *Neuroimage Clin* 2020; **25**: 102148 [PMID: 32097890 DOI: 10.1016/j.nicl.2019.102148]
- 53 **Zoon TJC**, Mathiopoulou V, van Rooijen G, van den Munckhof P, Denys DAJP, Schuurman PR, de Bie RMA, Bot M. Apathy following deep brain stimulation in Parkinson's disease visualized by 7-Tesla MRI subthalamic network analysis. *Brain Stimul* 2023; **16**: 1289-1291 [PMID: 37619890 DOI: 10.1016/j.brs.2023.08.013]
- 54 **Alper J**, Feng R, Verma G, Rutter S, Huang KH, Xie L, Yushkevich P, Jacob Y, Brown S, Kautz M, Schneider M, Lin HM, Fleysler L, Delman BN, Hof PR, Murrough JW, Balchandani P. Stress-related reduction of hippocampal subfield volumes in major depressive disorder: A 7-Tesla study. *Front Psychiatry* 2023; **14**: 1060770 [PMID: 36816419 DOI: 10.3389/fpsy.2023.1060770]
- 55 **Prener M**, Opheim G, Simonsen HJ, Engelmann CM, Ziebell M, Carlsen J, Paulson OB. Delineation of Grade II and III Gliomas Investigated by 7T MRI: An Inter-Observer Pilot Study. *Diagnostics (Basel)* 2023; **13** [PMID: 37189466 DOI: 10.3390/diagnostics13081365]
- 56 **Weng G**, Ermiş E, Maragkou T, Krcek R, Reinhardt P, Zubak I, Schucht P, Wiest R, Slotboom J, Radojewski P. Accurate prediction of isocitrate dehydrogenase -mutation status of gliomas using SLOW-editing magnetic resonance spectroscopic imaging at 7 T MR. *Neurooncol Adv* 2023; **5**: vdad001 [PMID: 36875625 DOI: 10.1093/oaajnl/vdad001]
- 57 **Purrer V**, Upadhyay N, Borger V, Pieper CC, Kindler C, Grötz S, Keil VC, Stöcker T, Boecker H, Wüllner U. Lesions of the cerebello-thalamic tract rather than the ventral intermediate nucleus determine the outcome of focused ultrasound therapy in essential tremor: A 3T and 7T MRI-study. *Parkinsonism Relat Disord* 2021; **91**: 105-108 [PMID: 34562715 DOI: 10.1016/j.parkreldis.2021.09.013]



Published by **Baishideng Publishing Group Inc**
7041 Koll Center Parkway, Suite 160, Pleasanton, CA 94566, USA
Telephone: +1-925-3991568
E-mail: office@baishideng.com
Help Desk: <https://www.f6publishing.com/helpdesk>
<https://www.wjgnet.com>

